

Abstract

LIU, LEI. Wireless Sensor and Embedded Active Diagnosis for Structural Health Monitoring. (Under the direction of Dr. Fuh-Gwo Yuan.)

Wireless smart sensor technologies, which integrate sensors and microprocessors with wireless communication, have become increasingly vital in structural health monitoring (SHM). Despite the fact that researches on wireless sensor for a variety of applications have made significant strides in these years, unique demands for structural health monitoring, in particular for active diagnosis, are not fulfilled. Followed by the discussion on the issues and challenges, e.g., contradiction between limited bandwidth and limited energy, this research investigates power aware solutions in wireless sensor platform and embedded damage localization algorithms.

For wireless sensors, improving sampling bandwidth with minimum power consumption is on focus in the first priority. Based on preliminary researches, a dual-processor based architecture is proposed and implemented to remedy inefficiencies caused by the traditional centralized architecture and serial operations. With parallel controlling, the architecture gains mega-hertz range sampling capability without unnecessary power consumption during data acquisition as the traditional architecture has. The implementation of hardware and software is also discussed in detail. The completion of the wireless sensor platform enables feasibility for active diagnosis where high frequency waves (small wavelengths) should be excited to detect damages in the size of millimeter range.

For embedded SHM algorithms, the imposition of distributed (decentralized) collaborative algorithms is required to cope with the large flux of sensory data, the limited processing capability and energy for wireless sensors. The later part of this work focuses on establishing a power aware damage localization algorithm for isotropic plates.

Higher-order theory is used to formulate the dispersion relation of elastic wave propagation in isotropic plates. Upon investigations on dispersion phenomena, a linear mapping algorithm is developed to remove dispersion, thereby enhancing signal resolution. The dispersion removal further facilitates traditional damage localization methods, such as cross-correlation, to be used in dispersive medium.

An energy decay model based on asymptotic expansion of the wave field is derived for damage localization. With the preclusion of noises, the proposed model provides a simple, yet effective method to obtain propagation distance by measuring the intensity of the diagnostic signal. To successfully embed damage localization into resources-constraint wireless sensors, computational complexity is lessened to expedite calculations and reduce energy consumption by providing exact solutions of the cross-correlation method and the energy decay method for damage localization in isotropic plates.

By embedding the proposed damage localization algorithm into the wireless sensor, experiments are conducted to validate the power efficiency of the proposed wireless sensor and algorithm. To compare the performance, three damage localization scenarios are tested, which are full transmission, embedded cross-correlation and embedded energy decay method. It is shown that the wireless sensor and the embedded energy decay method can construct a laboratory based SHM system with significant less power consumption to localize damage in isotropic plates and the combination holds promise for practical SHM systems.

WIRELESS SENSOR AND EMBEDDED ACTIVE DIAGNOSIS FOR STRUCTURAL HEALTH MONITORING

by

LEI LIU

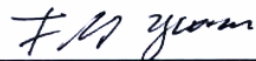
A dissertation submitted to the Graduate Faculty of
North Carolina State University
in partial fulfillment of the
requirements for the Degree of
Doctor of Philosophy

MECHANICAL ENGINEERING

Raleigh, NC

2006

APPROVED BY:



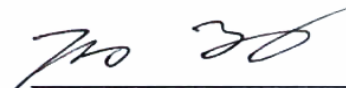
Dr. FuhGwo Yuan
Chair of Advisory Committee



Dr. Juei F. Tu



Dr. Kara Peters



Dr. TaoFang Zeng

Biography

Lei Liu was born in Wuhan, China. He attended HuaZhong University of Science and Technology in Wuhan during 1995-1998 in the department of Mechanical Engineering and received a Bachelor of Engineering degree in 1999. One year before the graduation, he was recommended to admission for M.S. program in the department of Mechanics at the same university and carried out graduate research work in 1998. During 2000-2001, he suspended his study and spent one year in Japan as a software engineer in StoneGate Co.. Then, he went back to the university and earned a Master of Science degree in the summer of 2002. After half a year of career life in Founder International Inc., he enrolled at North Carolina State University as a doctoral student of Mechanical Engineering in the spring of 2003, working toward his Ph.D. degree in the area of structural health monitoring with wireless sensors.

Acknowledgements

I would like first to express my great thanks to my advisor, Dr. Fuh-Gwo Yuan, who provided priceless support in my research, guided me by sharing his knowledge, and encouraged me to explore various areas. He has been an excellent supervisor, meticulous in reading my drafts, generous with his time and advice. Particularly, I am deeply indebted for his invaluable support on both academic and non-academic matters.

I am also grateful to all the members of my committee, Dr. Kara Peters, Dr. Jay Tu, Dr. TaoFang Zeng and Dr. M.N. Noori for serving on my committee and reading this dissertation. Special thanks go to Dr. Shaorui Yang, who has been a wonderful source of help and always ready to answer my most questions in mathematics. I also extend my gratitude to Mr. Taylor Frank for revising the writing.

I have benefited greatly through being able to meet and work with a number of colleagues during my doctoral work. Thanks go to Lei Wang for generously sharing his experience on plate experiments and initial Matlab code. Also, I thank Feng Zhang, who provided lots of effort during the development of the wireless sensor. Thanks are also due to all members in our group for nice academic and non-academic discussions. They are Dr. Yun Jin, Ms. Aihua Liang, Dr. Saeed Nojovan, Mr. H. Hussein, and Mr. Nate Pringle.

Above all, I want to express my gratitude to my parents and my love, Ying Hu, for their ability to adjust themselves to my situation and for the unreserved support and endless patience. Ying has endured more from me being in Raleigh than anyone should ever have to, particularly under the staggeringly difficult personal circumstances of the last four years. I can't guarantee this will turn out to be worth it but I promise that I'll try to make it up to you in our future together.

Table of Contents

List of Tables	vii
List of Figures.....	viii
1 Introduction	1
1.1 SHM and Wireless Smart Sensors.....	1
1.2 Reviews on Wireless Sensor for SHM	2
1.3 Challenges of Using Wireless Sensors for Active Diagnosis in SHM.....	6
1.4 Overview of This Research	10
2 Power Aware Wireless Sensor Architecture for Active Diagnosis	13
2.1 Traditional Centralized Architecture for Wireless Sensor	13
2.2 Improvements on Speed Using DMA	16
2.3 Improvements on Power Efficiency Using Dynamic Frequency Scaling	20
2.3.1 <i>Energy utilization of batteries</i>	21
2.3.2 <i>Dynamic power management</i>	23
2.3.3 <i>Dynamic frequency scaling within FPGA</i>	24
2.4 A New Architecture of Wireless Sensor for Active Diagnosis	29
3 Wireless Sensor Design with the New Architecture.....	32
3.1 Modularized Framework for Wireless Sensor Design	32
3.2 Processing Module	37
3.3 Supporting Module	39
3.4 Transduction Module.....	42
3.5 Interfacing Module	46

3.6	Verification and Summary.....	47
4	Elastic Wave Propagation in Isotropic Plates.....	53
4.1	Dispersion Relations based on Higher-Order Plate Theory	53
4.1.1	<i>Formulation of the higher-order plate theory</i>	<i>54</i>
4.1.2	<i>Dispersion relation for extensional wave</i>	<i>60</i>
4.1.3	<i>Dispersion relation for flexural wave.....</i>	<i>63</i>
4.2	Transient Wave Propagation in Dispersive Mediums	64
4.3	Dispersion Removal	70
4.3.1	<i>Linear mapping algorithm.....</i>	<i>71</i>
4.3.2	<i>Simulation and experimental verification.....</i>	<i>78</i>
4.4	Energy Decay Model.....	81
4.4.1	<i>The higher-order plate theory.....</i>	<i>81</i>
4.4.2	<i>The 3-D elasticity theory.....</i>	<i>86</i>
4.4.3	<i>Energy decay model.....</i>	<i>91</i>
4.5	Summary.....	95
5	Active Damage Localization for Isotropic Plates	97
5.1	Overview of Active Damage Localization	97
5.2	Active Damage Localization Using Correlation	98
5.3	Active Damage Localization Using the Energy Decay Model and Optimization Methods	102
5.4	Improvement on the Localization Methods: Matrix solutions	106
5.4.1	<i>Matrix solution for the correlation method</i>	<i>107</i>
5.4.2	<i>Matrix solution for the energy decay model</i>	<i>107</i>

5.4.3	<i>Singular value decomposition (SVD)</i>	110
5.5	Results from Simulated Data.....	111
5.6	Summary.....	121
6	Experimental Validation of Distributed Active Damage Localization within Wireless Sensor Network	123
6.1	A Three-Tier Network for Active Damage Localization	123
6.2	Experimental Setup.....	128
6.3	Experiments on Active Damage Localization	130
6.3.1	<i>Damage localization in base station with the Levenberg-Marquardt method</i> .	134
6.3.2	<i>Embedded damage localization using cross-correlation and SVD</i>	136
6.3.3	<i>Embedded damage localization using the energy decay model and SVD</i>	139
6.3.4	<i>Comparison and summary</i>	140
7	Conclusions and Future Studies	144
7.1	Conclusions	144
7.2	Future Studies	147
8	References	150
	APPENDIX	157
	Appendix A: Schematics of the Wireless Sensor	158
	Appendix B: VHDL Code for the FPGA core	167
	Appendix C: Analytical Expressions of The Five-peaked Waves	171

List of Tables

Table 2.1 A comparison of characteristic between MCU and FPGA.....	25
Table 3.1 A summary on the hardware specification of the wireless sensor.....	52
Table 4.1 Material properties and geometry of an Al 6061 plate.....	69
Table 5.1 Comparison of the solution of damage localization using cross-correlation.....	117
Table 6.1 Results of damage localization using the L-M method.....	134
Table 6.2 Results of damage localization using the cross-correlation method in slave nodes	138
Table 6.3 Results of damage localization using the energy decay model in wireless sensors	140

List of Figures

Figure 1.1 The organization of this dissertation	10
Figure 2.1 Traditional centralized architecture for wireless sensors	14
Figure 2.2 Picture of the extension board based on ripple counters	16
Figure 2.3 Block diagram of the extension module based on ripple counters	17
Figure 2.4 Block diagram for the extension module based on CPLD	19
Figure 2.5 Logic blocks programmed inside the CPLD	19
Figure 2.6 Pictures of the extension board based on CPLD	19
Figure 2.7 Discharge characteristic of the N battery used in this research [12]	22
Figure 2.8 IP core design in FPGA.....	26
Figure 2.9 Current consumption for a fully routed FPGA (AT94K10).....	28
Figure 2.10 DFS implemented inside FPGA	29
Figure 2.11 A new architecture of wireless sensor for active diagnosis.....	31
Figure 3.1 Module classification for COTS based wireless sensors.....	34
Figure 3.2 Board to board layout of the wireless sensor.....	36
Figure 3.3 Pictures of the processing module.....	39
Figure 3.4 Pictures of the supporting module.....	42
Figure 3.5 Pictures of the transduction modules: (a) Piezoelectric (b) Strain Gage and Acc. 45	
Figure 3.6 Picture of the interfacing module	47
Figure 3.7 Pictures of fully assembled wireless sensor	48
Figure 3.8 Data collected by the wireless sensor with 4 MHz sampling rate.....	49
Figure 3.9 Comparison between data collected by the wireless sensor and an oscilloscope..	50
Figure 3.10 Real-time acceleration measurement and comparison	51

Figure 4.1 Sign convention for the displacements, stress and moment resultants in a plate ..	54
Figure 4.2 Dimensionless phase velocity for extensional wave ($\nu = 0.33$)	62
Figure 4.3 Dimensionless dispersion relation for extensional wave ($\nu = 0.33$).....	62
Figure 4.4 Dimensionless dispersion relation for flexural wave ($\nu = 0.33$)	64
Figure 4.5 Dimensionless phase velocity for flexural wave ($\nu = 0.33$).....	64
Figure 4.6 Dimensionless group velocity for extensional wave from higher-order plate theory ($\nu = 0.33$).....	67
Figure 4.7 Dimensionless group velocity for flexural wave from higher-order plate theory ($\nu = 0.33$).....	67
Figure 4.8 Dimensionless group velocity calculated from 3-D elastic theory ($\nu = 0.33$).....	67
Figure 4.9 Dispersion of transient wave propagating in aluminum plate	69
Figure 4.10 The dispersion relation and its Taylor expansions for 1/8 in. plate.....	73
Figure 4.11 Illustration of the linear mapping for dispersion removal	73
Figure 4.12 Comparison of amplitude spectrum before and after linear mapping	75
Figure 4.13 Comparison of phase spectrum before and after linear mapping	75
Figure 4.14 Comparison of unwrapped phase spectrum before and after linear mapping	76
Figure 4.15 Block diagram of the dispersion removal procedure.....	77
Figure 4.16 Dispersion removal applied to the simulated data.....	79
Figure 4.17 Original signal and compressed signal from 1/8 inch plate	80
Figure 4.18 Original signal and compressed signal from 1/16 inch plate	81
Figure 4.19 Measured time-series signals with different distances	91
Figure 4.20 Normalized amplitude and signal energy decay ratios.....	92
Figure 5.1 Procedure of correct correlation with dispersion removal	101

Figure 5.2 The circle and its center for potential damage locations with given $\kappa = 7$ and 3	109
Figure 5.3 Simulated scattered wave by finite difference method with AWGN added	112
Figure 5.4 Comparison between contaminated signal and compressed signal.....	113
Figure 5.5 Comparison between un-contaminated signal and compressed signal.....	113
Figure 5.6 The cross-correlated sequences of contaminated signals and compressed signals	115
Figure 5.7 Damage localization using cross-correlation and NLS	116
Figure 5.8 Comparison of localization error by using L-M and gradient descent.....	117
Figure 5.9 Searching paths with different initial guess positions for L-M method	118
Figure 5.10 Damage localization through SVD.....	119
Figure 6.1 Illustration of the three-tier sensor network for active diagnosis	124
Figure 6.2 Experimental setup for active damage localization.....	128
Figure 6.3 Schematic for the experimental setup.....	128
Figure 6.4 Pre-damage wave, post-damage wave, and their difference (reflection wave)...	131
Figure 6.5 The reflection waves recovered in wireless sensors with the 1/16 inch plate	132
Figure 6.6 The reflection waves recovered in wireless sensors with a 1/8 inch plate	133
Figure 6.7 Time and energy consumption measured using the L-M method	135
Figure 6.8 Energy consumption measured using the cross-correlation method in slave nodes	137
Figure 6.9 Energy consumption measured using the energy decay model in slave nodes ...	139
Figure 6.10 Comparison of total energy consumption for one diagnosis cycle in a group ..	141

1 Introduction

1.1 SHM and Wireless Smart Sensors

Life cycle *in-situ* monitoring of critical structures such as aircrafts and civil infrastructure is vital for the safety of aging structures and long-term operational cost. Extreme loading and hazardous events on structures during operation can result in deterioration and flaws due to material fatigue, degradation, de-laminations, thus affecting integrity of structures. If these flaws are undetected at an early stage, the outcome could eventually be catastrophic. In order to respond to any structural abnormalities, associated damages should be detected, identified, quantified, and, if possible, continuously monitored. Consequently, acquiring knowledge of the nature and distribution of damage in a structure in service is compulsory to develop subsequent timely strategies to retard deterioration and enhance safety.

The objective of structural health monitoring (SHM) technology is to develop autonomous built-in systems for the continuous (or on-demand) monitoring, inspection, and damage detection of structures with minimum labor involvement [1]. The immediacy and sensitivity of SHM systems (SHMS) can lead to many potential benefits, such as short-term verification of innovative designs, early detection of problems, avoidance of catastrophic failures, effective allocation of resources and reduced service disruptions and maintenance costs. Typically, SHMS, in addition to the structures under monitoring, would include three subsets: sensors (or transducers), data acquisition system and damage detection/modeling system. Traditionally, computers are primarily used to serve as both of the latter two subsets and are wired to various sensors deployed on structures. Such implementation is essentially an extension of laboratory based data acquisition system. Located at a few critical points in

structures, the sensors convert ambient variables into electrical signals which are transferred to the computer over co-axial cables. The signals then are changed into digital format data by an analog-to-digital converter (ADC) and logged in the computer for further processing and interpretation by certain health monitoring algorithms.

The convergence of information technologies and wireless communications with vast reduction in cost, size and power consumption of complementary metal oxide semiconductor (CMOS) circuitry has brought new vistas for researches in SHM. The past several years have seen an increasing interest in the development of wireless smart sensors, networks and applications for SHM. Unlike the sensors (transducers) in current SHM systems which are only capable of transduction, wireless smart sensor, or abbreviated as wireless sensor, integrates functionalities of transduction, signal conditioning, signal processing, and wireless transmission. Since wireless sensor can process the data collected from ambient and condense the data into useful information locally, numerous advantages, such as robustness, flexibility, and fault-tolerance can be envisaged for SHMS. As in-service monitoring of structures has generated a high level of interest, inexpensive and durable wireless sensor networks to be applied in SHM applications have attracted much attention recently.

1.2 Reviews on Wireless Sensor for SHM

The term, “wireless sensor”, is not the traditional concept of “sensor”, but rather an autonomous data acquisition node attached to where traditional sensors can be attached. The essential difference between traditional sensors and wireless sensors is the intelligence capabilities, i.e. an on-board microcontroller unit (MCU). A definition for the wireless sensor can be found in [2], which states wireless sensor must have four important features: (i) on-board MCU (ii) wireless communication, (iii) small size, and (iv) low-cost. Though this

definition is pretty modernized, early works on wireless sensors can be attributed to those designs without concerns on the last two features. Particularly, it is likely better to extend the definition with another factor: low power. The extension is important because wireless sensor faced severe challenges on power consumption [3].

For SHM, initial efforts made on wireless sensors can be traced back to the 1990's. Straser and Kiremidjian (1998) presented a design of a low-cost wireless modular monitoring system (WiMMS), which uses commercial off-the-shelf (COTS) components and consists of a microprocessor, a radio modem, data storage chips, and batteries, for civil structures monitoring [4]. An 8 channel, 16-bits ADC with fixed 240 Hz sampling rate was used to monitor strain and implement near real-time damage diagnostics. The presented unit contains almost all features in the previous definition and may represent the first major step by the structural engineering community towards decentralized data processing and wireless SHM, though power consumption is not emphasized.

Meanwhile, Mitchell *et al.* (1999) developed a prototype of wireless sensor for SHM and smart structures that allows data from multiple sensors to be communicated over a single communication channel [5]. This improvement virtually brought the concept of network into wireless SHM. Lately in 2002, Mitchell even extended this work to allow users to access the wireless sensor network via internet. Although the latter work has little contribution solely to wireless sensor, it actually demonstrated the flexibility of a SHMS based on wireless sensors.

Recognizing the importance of decentralized data processing, Lynch *et al.* (2001) demonstrated a proof-of-concept platform which includes a 4MHz CPU to accommodate a wide range of analog sensors and a Direct Sequence Spread Spectrum (DSSS) radio to enable communication among the sensors [6, 7]. A maximum 1 kHz sampling rate with 14 bits

resolution can be reached in some units using the ADXL210 accelerometer. Lynch kept improving their work since then and has reported a continuous flow of improvements on speed and efficiency based on the original design [8-10].

Meanwhile, wireless sensors built for general purpose applications, which can partially meet the need for SHM applications, have been continuously developed and improved by researchers in electrical engineering field. Remarkably, an open platform for smart sensing applications, MICA Motes series, has been presented by U.C. Berkeley since 2002 [11]. The main idea behind this research is to develop smart dust, or Motes, in which the ultimate goal is to create a low-cost, fully autonomous system within a cubic millimeter volume, allowing for the realization of dense sensor arrays. The original hardware system includes a 4 MHz MCU with an internal 10-bit ADC, a software stack radio (CC1000) and a 4M bit EEPROM. Through a 51-pins connector, it brought modularity to support different types of sensors. A comprehensive embedded system, named as TinyOS, was developed to allow rapid and easy development for users. This achievement in effect set a milestone for wireless sensors that enables researchers from different backgrounds to easily apply wireless sensors to their fields. Innumerable publications about using Motes in SHM can be found between 2003 and 2005, and applying wireless sensors for SHM has become a hot topic since then. However, due to the limitation of the sampling speed, the majority of these publications still focused on strain sensing and dynamic response of structures.

As an astonishing success, MICA Motes has been constantly upgraded by several different contributors. MICA2 and MICAz were developed and commercialized by Berkeley's group and Crossbow (www.xbow.com). Also extended from the Berkeley Motes, Intel has announced the development of the Intel-Motes platform to focus on additional

hardware and software improvements and increased levels of integration [12].

A new wireless communication standard, IEEE 802.15.4 [13], was established and released in 2003 for low data rate sensor network. The majority of the effort is not only to provide power efficient protocol for energy-constrained wireless sensors, but to attempt to unify the communication interface across wireless sensor design/platforms for compatibility. Since then, many designs (2003-2006) providing different features have been proposed and presented based on the new communication standard [14-17].

It must be pointed out that, although the achievements made on wireless sensors have made significant strides, the wireless sensors or prototypes were mostly designed or suitable for low frequency applications primarily used for monitoring civil structures. The limitations in performance impede the continuously expanding demands of other SHM applications. For instance, the interests on high frequency signals may not be satisfied. Kiremidjian *et al.* [18] commented that pushing data acquisition and computation forward is fundamental to the smart sensing and monitoring system, which represents a radical departure from the conventional instrumentation design and computational strategies for monitoring civil structures. For non-destructive evaluation (NDE)/SHM applications that employ acoustic and ultrasonic waves, particularly guided wave, for damage interrogation [19-21], sampling capability of wireless sensors must be significantly improved to at least fulfill the minimum requirement established by the Nyquist-Shannon sampling theorem. Lynch and Loh [22] also indicated the increasing need for higher sampling rates in excess of 500 kHz. As a result, wireless sensors that are capable of high speed data acquisition/excitation are expected to empower fine-grain sensor measurements and associated algorithms.

1.3 Challenges of Using Wireless Sensors for Active Diagnosis in SHM

Diagnosis strategies employed in SHMS can also be broadly classified into two categories: global methods and local methods. The global methods infer or assess the state of a structure from its overall modal response, while majority of them are vibration-based methods to detect damage existence and to attempt to localize damages [23]. However, there are several essential disadvantages associated with such methods, such as low sensitivity and poor reliability due to limited number of modes. The only primary attraction is that they require few numbers of sensors than that for local methods, which may be a great benefit in traditional SHMS. In contrast, local methods, such as ultrasonic non-destructive evaluation (NDE), use direct examination of structural members to determine the condition of those members. They can precisely give indications of the location and possible severity of the damage in the area where they are applied.

The topic on diagnosis strategies can not be completed without covering the diagnostic technologies. For SHM, the diagnostic technologies can be generally classified as (1) passive diagnosis and (2) active diagnosis. The fundamental difference between them is that active diagnosis has known inputs (both sensors and actuators) whereas passive diagnosis does not. A passive system uses various types of sensors, such as fiber optics, strain gages, and accelerometers to listen and evaluate characteristic signals from structures due to external impact events, damage evolution, etc.. On the other hand, an active diagnosis system, or active damage localization system, is also equipped with actuators to generate selected diagnostic signals (excitations) to interrogate the health status of structures. Commonly, passive diagnosis systems are used to monitor the overall condition of structures; while active diagnosis systems can provide fine-grain information to identify the location and

the nature of the damage in individual components of structures. It should be noted that various types of excitation signals with different waveforms may provide different degrees of sensitivities to a specific type of damage in a structure. This is because a sensor's responses from a specified excitation signal generally depend on the interaction between the sensor/actuator and the host structure, the material properties of the structure and the damage mechanisms.

To monitor critical structures, local methods and active diagnosis is generally important. However, active diagnosis requires that devices have relatively higher speed than that of passive diagnosis. For instance, the frequency of diagnosis signal may range from tens of kHz to hundreds of kHz. The demand of the sampling capability is far beyond that those cited wireless sensors can offer. Increasing the sampling capability may seem to be trivial task at first glance. However, with the conventional architecture used in current wireless sensors, it is almost impossible since MCU may be required to be run at hundreds of megahertz (MHz) frequency. Although MCU is increasing in speed, and reducing in power consumption as technology improves, practical wireless sensors with the conventional architecture for high speed sensing need a technology improvement for many years to come.

Energy constraint is a critical issue for wireless sensor and networks [24, 25]. As self-contained devices, wireless sensors may be expected to be embedded into structures or installed in hostile or inaccessible areas with little or no maintenance. Although numerous investigations [26-28] have been made on self-powered (i.e. power scavenging) devices to harvest energy from external environments, such as sunlight, vibration and motion, either they are not powerful enough to provide stable energy or their usages are limited to specific ambient. Energy constrained batteries are the only primary power sources currently used by

almost all wireless sensor prototypes. Therefore, minimization of power consumption at all levels of a wireless sensor is critical to promise a reasonable life. The critical issue promptly necessitates that wireless sensor must attain power efficiency, or be power aware, on both its design and its applications.

To minimize the power consumption, power consumptions associated with different tasks must be analyzed and identified. The following list points out individual power consumption and gives a briefly explanation as below:

- *Acquisition consumption:* The power consumption for sensing is strongly tied to the speed requirement of applications and the selection and design of hardware. As a rule of thumb, the faster speed a circuit operates, the more power is required. In current wireless sensors, however, deficiency is presented as that wireless sensor must run at a speed which is a multiple of desired sampling speed.
- *Communication consumption:* The power consumed in communication is directly proportional to the amount of data exchanged and other factors, such as encoding strategies. Reducing the communication flow, or specifically the amount of data transmission, is the essential way to improve power efficiency.
- *Computation consumption:* The power consumption for computations depends on the arithmetic algorithms used for data processing and interpretation, which may be desired to reduce the communication consumption. Utilizing efficient algorithms is fundamental to make balance between performance and power consumption. On the other hand, complex algorithms which may obtain higher degree condensation of information may impose many iterations and complicated calculations and require long CPU time. Thus, tradeoff must be made between the computation consumption and the communication

consumption. Notably, most wireless sensors do not have floating-point unit (FPU) for supporting floating-point operations. Excessive time for the computation of a complex algorithm may be incurred as the floating-point calculation is operated by software routines. For instance, a simple multiplication of two floating-point numbers may require hundreds of MCU cycles in wireless sensors.

From the above statements, it may be seen that the *acquisition consumption* is relatively independent, while the *communication consumption* and the *computation consumption* are interrelated with each other and strongly coupled with specific diagnosis methods or algorithms. On the other hand, from a systematical viewpoint, the acquisition consumption has more concern on hardware of wireless sensors, and the last two are relevant to software inside wireless sensors.

To use wireless sensors with active diagnosis for SHM, challenges lie on the minimization of all the identified power consumption. First of all, hardware design of the wireless sensor must be improved to enable high speed sensing capability and retain power efficiency. The improvement must keep the acquisition consumption as low as possible, while the interest on sensing high frequency signal must also be satisfied. Secondly, the optimization and tradeoff between the communication consumption and the computation consumption must be made to limit total power consumption in a minimum. Especially in active diagnosis, the increased sampling rate may result tremendous amount of data to be processed or transmitted. Emphasizing on power awareness of wireless sensors and SHMS, the research needs focus on the investigation of both hardware and software to apply wireless sensors with active diagnosis for SHM.

1.4 Overview of This Research

This research seeks to address the power awareness of wireless sensors and SHMS with a final goal of providing an improved architecture for power efficient data acquisition/excitation, designing a novel wireless sensor with high speed data acquisition/excitation capability, and proposing a power efficient damage localization algorithm and strategy for active diagnosis of isotropic plate. According the discussion in Section 1.3, the dissertation is organized into two parts as shown in Figure 1.1.

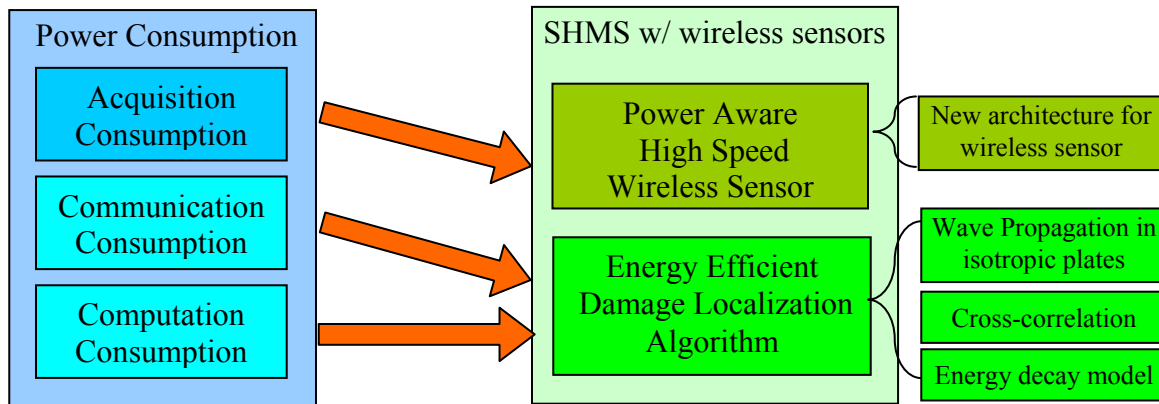


Figure 1.1 The organization of this dissertation

In the first part, the minimization of the acquisition consumption is explored to obtain power efficient wireless sensor hardware. Upon reviewing the conventional architecture of wireless sensors and addressing the deficiency, improvements on both speed and power efficiency are presented and discussed. Unlike other wireless sensor, the development of a new architecture and the introduction of logic-based processor increase the maximum sampling frequency to be identical to the operating frequency. Dynamic frequency scaling is proposed to be used along with other methods used in conventional wireless sensors to achieve a power aware design. The implementation of the proposed architecture is given in detail and verified.

Chapter 2 points out the deficiency of the conventional architecture of wireless sensors and proposed a new architecture for wireless sensor which satisfy the requirement of active diagnosis. Improvements required for both speed and power efficiency are addressed and discussed. After detailed discussion of parallel controlling and dynamic frequency scaling, a power efficient solution for wireless sensors with high speed sensing/actuation capability is provided. Chapter 3 describes the implementation of a wireless sensor based on the proposed architecture. FPGA integrated wireless sensor based on the proposed architecture. A brief outline of the capabilities and specifications of the wireless sensor is listed. Also, strains and accelerations collected by the wireless sensor are compared with those collected by an oscilloscope to verification the accuracy.

In the second part, the minimization of the communication consumption and the computation consumption are investigated. Since both power consumptions are strongly related to the algorithm or software running in a wireless sensor and are application specific, this research investigates damage localization for isotropic plates with wireless sensors and active diagnosis in which propagating elastic waves are used to detect and locate potential damages. The power efficiency of wireless sensor with different damage localization methods are compared and discussed.

To correctly characterize wave propagation in isotropic plates, higher-order plate theory is used to derive dispersion relations. Based on leading-order asymptotic solution under impulsive point load, an energy decay model is established to obtain the time of arrival of diagnostic waves propagated in isotropic plates. For the purpose of comparison, a traditional method, i.e. cross-correlation, is also introduced. Noticing the inexactness of the cross-correlation method due to wave dispersion, a linear mapping algorithm is developed to

compensate dispersed waves and enable the cross-correlation method to correctly obtain the time of arrival of dispersed waves. To reduce computational complexity, nonlinear least-squares problems for damage localization with both methods are simplified to linear least-square problems to obtain matrix solution using singular value decomposition.

In Chapter 4, dispersive elastic wave propagation in plate will be investigated. The higher-order theory will be used to derive dispersion relation for both extensional wave and flexural wave in isotropic plate. To correctly handle and interpret dispersed wave after long distance propagation, a linear mapping algorithm will be proposed, developed and verified. Additionally, an energy decay model based on asymptotic solution will be developed to be used in active damage localization.

Chapter 5 addresses the investigation made to reduce computational complexity of two damage localization methods: cross-correlation and energy decay model. Particularly, both methods have attractive characteristics that enable dramatic reduction of the communication consumption and possibility of distributed computation. Comparison and discussion basing on simulation data will be given.

In Chapter 6, the power efficiency of active damage localization is explored. A three-tier wireless sensor network is proposed and the two damage localization methods are embedded into wireless sensors to evaluate computation consumption and communication consumption under different conditions.

Chapter 7 summarizes the research detailed in this dissertation and presents possible directions for future research on SHM employing wireless sensors.

2 Power Aware Wireless Sensor Architecture for Active Diagnosis

Wireless sensors have become increasingly vital in structural health monitoring applications. However, conventional designs of wireless sensor have low I/O throughput and are not capable of high speed sensing/excitation, which are usually essential for active diagnosis and ultrasonic non-destructive evaluation (NDE). A key step to enable wireless sensors to be suitable for active diagnosis is to understand the system requirement to satisfy two requirements: high speed and affordable power consumption. The focus of this chapter is to address issues and deficiencies of conventional wireless sensors which are originally targeted to low speed applications, and to develop a new architecture for high speed applications. The proposed new architecture is not tied to any particular processor/controller platform but rather details how a co-processor with parallel processing functionally can minimize the power consumption.

2.1 Traditional Centralized Architecture for Wireless Sensor

All wireless sensor prototypes, reviewed in Section 1.2, have their own unique features with various selections of hardware components. However, the core of their designs is a low power MCU with compact package. The benefit of using the MCU is obvious as all prototypes are built with commercial off-the-self components: it is widely available, easy to interface with other chips, integrated with many useful modules, and most importantly it only has very low power consumption to enable the possibility of long term operations. Besides that, data flashes with serial interface working as data storage are usually in favor, primarily to free the MCU's I/O pins for future extension. For instance, the representative wireless sensor, Mica Motes [11], was designed to have a 4 MHz MCU with an integrated ADC

(Analog-to-Digital Converter) and a 4Mb external data flash. The single MCU running programmed instructions controls all peripherals and itself. Peripherals chips are operated sequentially and can be turned off (or put into power down mode) to save power if they are not in use. Thereby, a centralized architecture is founded.

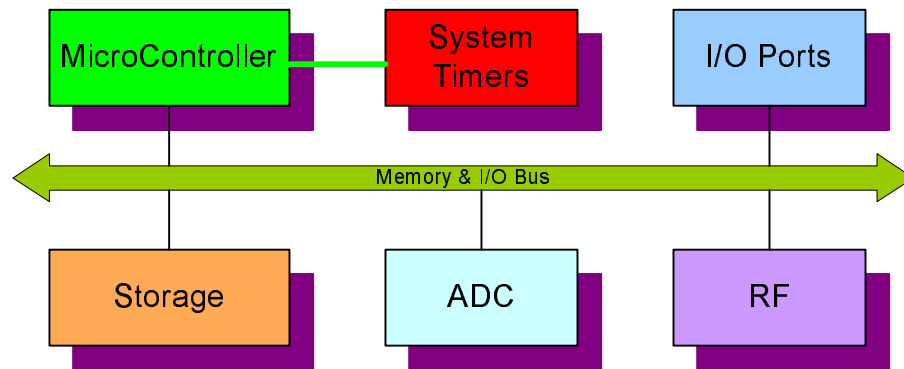


Figure 2.1 Traditional centralized architecture for wireless sensors

Figure 2.1 depicts a typical architecture used to design wireless sensors. The core of the architecture is a central MCU that is clocked by system timers. Although there may be multiple I/O ports existed in the MCU, only one I/O port can be accessed by the programmed instructions at a time. Virtually, only one I/O bus exists as shown in the figure. The MCU is timeshared by all peripheral chips, including storage device, ADC, RF chip and other potential devices connected from the I/O ports. Communications between the MCU and the peripheral chips are made through the I/O bus sequentially. For example, accessing to the ADC has to be queued before that the MCU completely writes previous data into the storage. Ideal concurrence is not possible in this centralized architecture with MCU. Software approach, i.e. context switching, is generally designed in operating systems with the supports of multithread library to enable multi-tasks applications.

The centralized architecture can lead to a very concise design of wireless sensors. Nevertheless, the performance of wireless sensors is inevitably hindered by the centralized

architecture because of the serial operation of MCU. To perform an operation that involves multiple peripheral chips, the MCU has to control and access those chips one by one and a simple operation may require multiple clock cycles to be completed. For instance, a sampling operation which takes one sample may be decomposed into the following steps: (1) operations on the ADC; (2) Data reading (from the ADC into internal memory in the MCU); (3) operations on the storage (specifying correct address); and (4) Data writing (from the internal memory to the storage). Since each step usually requires multiple instructions, it is not unusual that a sampling operation takes tens of MCU clocks to complete. Additionally, the desire of large volume storages to accommodate more data and the availability of MCU I/O pins usually lead researchers to choose flash memories with serial interface as storage. The compromise remarkably degrades I/O speed between the MCU and the storage since data has to be exchanged sequentially bit by bit with additional overhead for address controls (i.e., page and offset). In the Motes, although the ADC is capable of 15 ksps (kilo sampling per second) at maximum resolution (10-bits), the serial flash can only be operated at a low throughput rate (around 40 kbps with 8-bits width), resulting a maximum sampling rate limited to around 4 ksps, which is far below the requirement for ultrasonic NDE.

The deficiency of the centralized architecture can be evaluated from both speed and power consumption. Due to the sequential operation, unnecessary waiting of inactive chips results in delay in time and waste in power. In low speed applications, the deficiency may be not significant: for speed, the MCU may run at an operating frequency which is much higher than the required sampling rate; for power consumption, the sensing operation may need only a fraction of time. In high speed application, however, the deficiency may be too severe to make the centralized architecture impractical: The MCU may be required to run at tens of

MHz to satisfy the sampling rate only; while power consumption are increased to an unacceptable level due to the high operating frequency and the waste.

2.2 Improvements on Speed Using DMA

For active diagnosis in SHM, diagnosis signal with tens of thousands, or even hundreds of thousands Hertz is not unusual. The sampling capability of wireless sensors with the centralized architecture is far below requirements. As mentioned in the previous section, MICA Motes can only be capable of sampling at 4 ksps, which is only able to recover signals with frequencies below 2 kHz per the Nyquist–Shannon sampling theorem. The demand of SHM promptly needs wireless sensors with high speed sampling capability.

In modern computers, Direct Memory Access (DMA) technology is widely used to allow certain hardware subsystems within a computer to access system memory independently of the Central Processing Unit (CPU). Data are transferred or communicated between devices without subjecting the CPU to a heavy overhead. Computers that have DMA channels can transfer data much more quickly than computers without a DMA channel. To enable wireless sensor to be applied to high speed applications, attempt to extend the centralized architecture with DMA was made in the initial stage of this research.

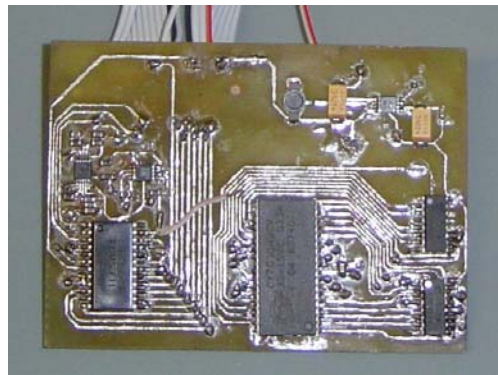


Figure 2.2 Picture of the extension board based on ripple counters

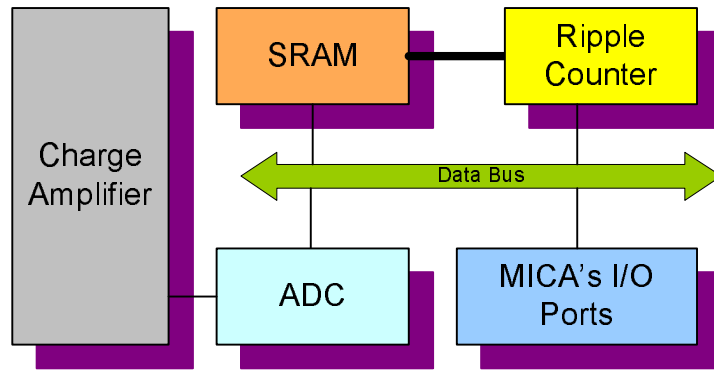


Figure 2.3 Block diagram of the extension module based on ripple counters

An extension module was designed to be attached to the MICA Motes (Figure 2.2). An external SRAM with high volume (4MB) and an external ADC (8-bits) were used. Unlike the flash with serial interface, the SRAM has parallel interfaces for both data and address. Since the MICA Motes does not have enough amount of I/O pins, a ripple counter is specially designed to works as an address controller for the SRAM. The ripple counter allows that individual cell in SRAM can be sequentially access within two MCU clock. Additionally, to support piezoelectric sensor, a charge amplifier were designed to covert the charge generated from piezoelectric into voltage, and simultaneously function as a high-pass filter to remove low frequency noises.

The difference and the benefit of the DMA may be best explained by checking the block diagram of the extension module which is illustrated in Figure 2.3. Two buses are defined in the design. One of them is specified for data communication and simply an extension from a MICA's I/O port on which all add-on components are connected. The other is defined for address control of SRAM indicated with the bold line in the figure, which only locally exists in the extension board. The MCU in the MICA is only responsible for providing control signals to the ADC and the SRAM, and clocks the ripple counter. In contrast to what does in the centralized architecture, the data converted by the ADC in each

sampling cycle is directly written into the SRAM through the data bus. The MCU has no awareness of the value of data, but rather information about the number of data. After the writing, the MCU provides a clock to the ripple counter to increase its output by one. Since the SRAM is addressed by the ripple counter, data in the following sampling cycle will be written into the next cell of the SRAM. Consequently, the compromise mentioned in the previous section is not necessarily to be made and deficiency in I/O speed is partially minimized. Since the MICA Motes operate at 4 MHz, maximally 2 MHz clock can be generated by software. Sampling rate up to 300 kbps was achieved with the serial execution of all steps and at least 13 MCU clocks are required to complete a sampling cycle. Detail about the controlling steps in a sampling cycle can be found in [29].

It must be noted that data stored in the SRAM has to be sequentially accessed by the MCU due to the ripple counter. This may result in deficiency in data processing in which the MCU may need to access data in random addresses. Also, the sampling rate achieved is still not high enough to meet the requirement of sensing ultrasonic signals. To further push the sampling rate up, another improvement is made through using a Complex Programmable Logic Device (CPLD) as a specific DMA controller. CPLD is a programmable logic device offering high speed and predictable timing and is ideal for implementing a complex finite state machine. Since CPLD can concurrently control multiple chips, the operations on an ADC and a SRAM can be made simultaneously. Multiple steps in a sampling cycle may be combined to reduce latency.

The block diagram of the second extension module is presented in Figure 2.4. Similar DMA approach was adopted for sampling and data access. However, A CPLD, XC9572XL from Xilinx, takes the role for controlling and addressing since it has abundant resources

with programmability. I/O pins of the CPLD are categorized into two groups: control pins and data pins. Data pins are directly connected to the data bus, while control pins are connected to the ADC, the SRAM, and the MICA's connector. The CPLD is internally divided into several logic blocks, which is given in Figure 2.5. The command dispatcher interprets the instructions from MICA, while the DMA controller coordinates the SRAM controller and the ADC controller to cooperate together during the sampling. The address latch is used to temporarily store the target address since the data bus is 8 bits whereas 17 bits are required to control the address of the SRAM.

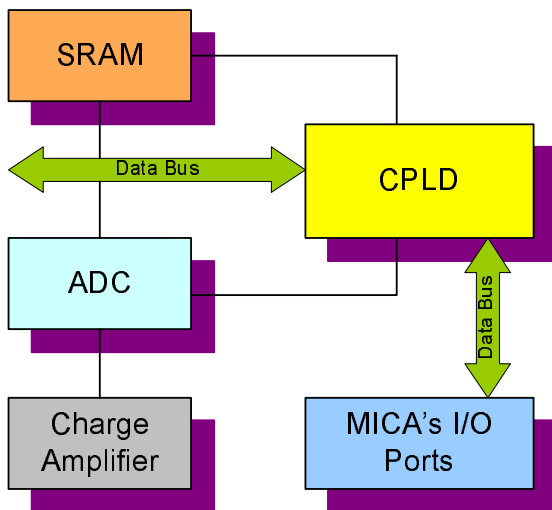


Figure 2.4 Block diagram for the extension module based on CPLD

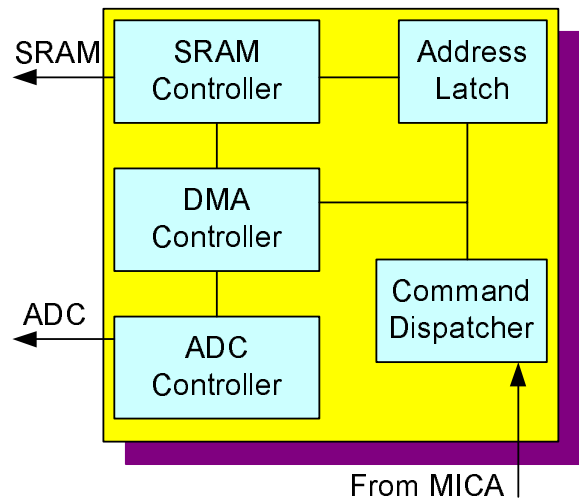


Figure 2.5 Logic blocks programmed inside the CPLD



Figure 2.6 Pictures of the extension board based on CPLD

A typical operation may be initiated by filling the address latch with the target address of the SRAM, that is, three bytes are sent from the MCU and stored into the address latch. Then, the DMA controller will notify the SRAM controller to initialize the SRAM with the target address. Following that, the MCU in MICA only needs to send certain commands (in the form of data) to the CPLD to let it know the sampling speed, the sampling duration, the desired data length and etc.. For data sampling, a typical sampling cycle will be started by the DMA controller to notify the ADC controller to do sampling and conversion. Once a data is available, the SRAM controller will be notified to physically latch the data into the SRAM. Then, the address of the SRAM will be incremented by the SRAM controller and the DMA controller will go into a new cycle again.

It may be noted that the MCU has no direct access to the SRAM and the ADC since the CPLD functions as a co-controller for SRAM and ADC. All essential controlling logic functions are encapsulated in the CPLD, which is clocked by a 4MHz oscillator. This gives the design a very promising feature that all functionality and detailed information for data acquisition and storage is hidden inside the extension module. A sampling rate around 800 ksp/s was achieved in this improvement [30]. Since the CPLD can simultaneously control both the SRAM and the ADC, totally 5 CPLD clocks are required for obtaining one sample. Compared to the first extension, the issue of random data access is partially resolved due to the contribution of the address latch.

2.3 Improvements on Power Efficiency Using Dynamic Frequency Scaling

The improvements made previously by using DMA technology have significantly increased the I/O speed and the sampling rate. However, a practical design of wireless sensor must also satisfy the other requirement: the power consumption must be affordable for

batteries, or the power efficiency must be maximized.

There are many aspects to be considered to achieve a power aware design from a viewpoint of system. First of all, the energy utilization of batteries must be explored. Although the utilization seems to be not related to the power efficiency at first glance, the regulation circuits used to exert energy from batteries have different characteristics which may affect the power efficiency and design. Secondly, proper power management needs to be investigated as a straightforward way to improve the power efficiency is to turn off inactive components. Particularly for high speed wireless sensors, the instantaneous power consumption for data acquisition needs to be minimized. In this section, these first two topics will be covered in general as they have been intensively investigated in researches for conventional wireless sensors. Dynamical frequency scaling technology is proposed to be embedded into a Field Programmable Gate Array (FPGA) to reduce the instantaneous power consumption for data acquisition. The software proposed to be programmed in the FPGA core is covered to show the advantage.

2.3.1 Energy utilization of batteries

As that pointed out in the introduction, batteries are the only practical power supplies of wireless sensors nowadays. Even if there is a break through in power scavenging devices, charge buffering devices, or specifically batteries, are still essential to exist between power scavenging devices and wireless sensors. In other words, batteries are always of importance viewing from the side of wireless sensors. Consequently, the optimal utilization of the energy source ends up to investigations related to batteries.

Nominally, the capacity of a battery is rated and given in milliamp-hours (mAh). However, predicting life of batteries used in wireless sensors is not a trivial task since it will

differ under different circumstances, e.g. current draw and cutoff voltages. Also, the output voltage and the current sourcing capability varies over the life of a battery, and depends on many factors, such as battery dimensions, type of electrode material and some anomalies that can appear during drain. Discharge curves with constant current for the N size battery used for the wireless sensor in this research are

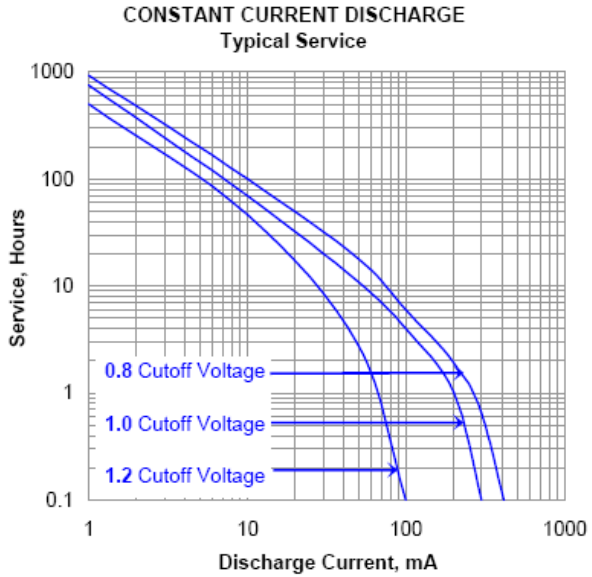


Figure 2.7 Discharge characteristic of the N battery used in this research [12]

shown in Figure 2.7 [12]. Although the figure is for the particular alkaline battery from Energizer, it can represent typical discharge characteristics for alkaline batteries without losing generality. When the constant current draw is 80 mA, a battery can last 9 hours with 0.8V cutoff voltage, but only 0.2 hours with 1.2V cutoff voltage. It can be clearly seen that most of battery capacity lies below 1.2V and the service life of a battery can be significantly extended with low cutoff voltage.

To optimize the utilization and fully exert the energy, a boost regulator must be included in a wireless sensor. Theoretically, the lower startup voltage the boost regulator supports, the longer life can be expected for batteries. However, some limitations, such as internal resistance and electric circuits, usually imply a bottom line of 0.8V. To roughly estimate the life of a battery, 80% of the rated capacity may be used [31].

Two important issues must be addressed with the boost regulator. The first is the side effect arising from imperfect efficiency. Efficiency of the boost regulator can be defined as

the ratio of the output power and the input power, which may not perfectly be 100% due to the power loss for switching and regulating. The efficiency decreases when the output power is relatively small since the power loss almost keeps constant. When a wireless sensor enters standby mode, the power loss will constitute a significant fraction of the total energy consumption. Hence, the boost regulator must be operated at a low switching frequency or adaptive switching frequency to obtain high efficiency for low current load. However, such compromise may raise the second issue: the current source capability. The boosting and regulating is made through DC-AC-DC by using switching technology which will be briefly introduced in Section 3.3. Due to the volume limitation of inductors and capacitors, the charge converted in a unit time has a maximum value. For circuits which require large current in a transient duration, such as those for prospective embedded excitation or actuator driving, they may suffer from the limited current sourcing capability. As a solution, two power buses may be required in a wireless sensor: one provides regulated power for normal operations, while the other provides direct connection to batteries for high power operations.

2.3.2 Dynamic power management

Dynamic power management (DPM) has been widely used in applications and investigated in researches. The basic idea of DPM is to reduce overall power consumption by turning inactive components off or putting them into sleep mode [32]. Depending on the policy adopted, a wireless sensor can enter different mode of operation in which different circuitry parts are active. Each such mode is characterized by a certain power consumption and time necessary to the components to become active again. Typically, the less the power consumption, the longer the time overhead to resume chips from sleeping. Since the power management policy is beyond the scope of this research, only the modes of operation

potentially existed in a high speed wireless sensor are of concern.

From the improvements on speed, it has been shown that a secondary processor/controller may dramatically increase the performance of a wireless sensor. The following modes may be identified for dual-processor architecture:

- Sensing/Actuation mode: all components are in active status. The instantaneous power consumption at this mode may be the highest. However, since wireless sensor only operates at this mode in transient. The overall power consumption may be still affordable for batteries depending on the duty cycle.
- Computation mode with hardware acceleration: The secondary processor, running at a higher frequency, may be used to perform high speed computation for certain algorithms which require hardware acceleration.
- Computation mode: Certain algorithms in the form of software running in the primary processor to interrogate the collected data.
- Communication mode: A wireless sensor communicates with other devices, *i.e.* other wireless sensors and base station.
- Standby mode: All chips, including the processors, are put into power save mode. The primary processor wakes up periodically and turns on RF chip to check incoming messages to keep a wireless sensor vigilant over the network.

2.3.3 Dynamic frequency scaling within FPGA

In principle, processors can be divided into two classes: instruction based processor and programmable logic based processor. The first type, often referred as microcontroller unit (MCU), executes preset instructions by sequentially fetching, interpreting, outputting in one or multiple clock cycles. With slightly higher cost and power consumption, the second

type possesses a higher degree of flexibility. This type of device, such as CPLD and FPGA, can be configured to create arbitrary combinatorial logic functions, even soft-MCUs. Parallel processing and controlling can be implemented at hardware level. FPGA is an array of gates with programmable interconnections and logic functions. Comparisons are made between typical FPGA and MCU in Table 2.1.

Table 2.1 A comparison of characteristic between MCU and FPGA

	Instructi on set	Pre-built functions	I/O number	Power	Ease of programming	Parallelism	Cost
MCU	Support	Yes	Few	Low	Easy	No	Low
FPGA	N/A	No	Abundant	Moderate	Fair	Yes	Moderate

It has been discussed and concluded that the instruction based processor is not able to design a high speed system with power efficiency. The improvement with CPLD shows the advantage of using the programmable logic based processor, in which the total number of clocks required to complete a sensing cycle is reduced from 13 to 5. Obviously, if a sensing cycle can be made within one clock, maximum power efficiency can be obtained since no power will be wasted on the waiting. However, the data-width of the ADC's output (10-bits) differs from the data-width of the SRAM's input (8-bits or 16-bits which depends on the configuration). If using the SRAM in 8-bits mode, the SRAM's address has to be increased twice in a single sensing cycle in order to completely save the data from the ADC. This may double the clock cycles required to complete a sampling cycle and should be avoided. In contrast, if using the SRAM in 16-bits mode and directly connecting the ADC to the SRAM, 37.5% volume of the SRAM may be left unused. In the design with CPLD, the resource of the CPLD is so constrained that it is nearly impossible to program it more complex operations.

To solve the issue, FPGA is proposed to substitute CPLD to work as the secondary

controller for sensing. A FIFO (first in first out) style shifter may be designed in a FPGA to relay the data from the ADC to the SRAM. The shifter is 24-bits long, and virtually works like a dual ports register. The logical circuitry for ADC controlling (ADC controller) directly pushes the data from the ADC into the shifter in each sensing cycle, and another logical circuitry for SRAM controlling (SRAM controller) save the data in the shifter into the SRAM whenever the accumulated bit length exceeds 16. These two controllers work independently without awareness of each other. Only five times of data saving will occur within every eight sensing cycles. This can be easily understood as that the common multiple of 10 and 16 is 80.

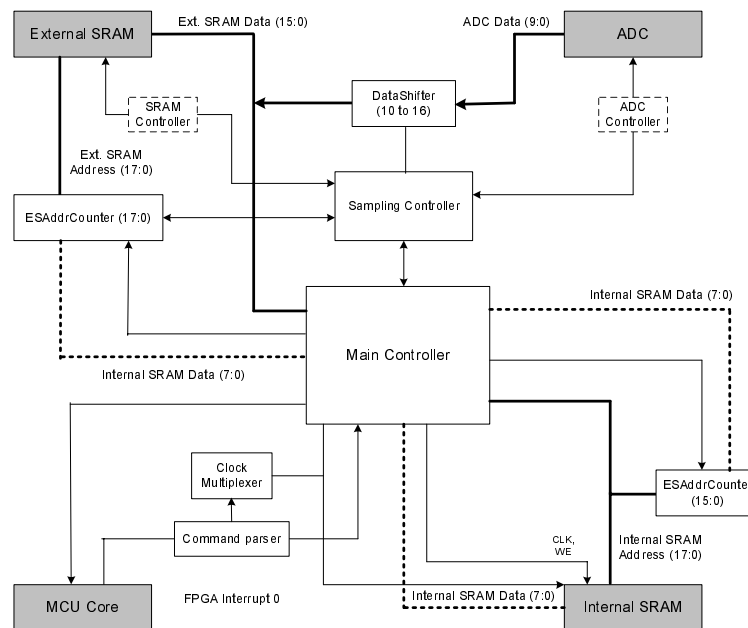


Figure 2.8 IP core design in FPGA

Figure 2.8 graphically expresses the conformation of the core design proposed in a FPGA with four shaded boxes representing components outside the FPGA. A command parser receives command from the MCU and changes the status of the main controller. Two address buses exist for to correctly locate both an internal SRAM between the MCU and the FPGA and an external SRAM. Two counters with different bit-length are connected to the two buses respectively. When the address of a SRAM needs to be set, the counter will be

initialized by the main controller within three clock cycles. After that, the counters will automatically incremented by one in every FPGA clock to make the next cell of SRAM accessible. A virtual sampling controller, which is cascaded from the main controller, controls the sensing procedure. The sampling will continues until the address counter reaches a preloaded upper limit. By the cooperation of these controllers, one sensing cycle can only require one clock with full utilization of SRAM. The same method can also be easily migrated to be used for the case of actuation, in which the ADC is replaced by a digital-to-analog converter (DAC). Programmed with VHDL, the core physically includes 152 flip-flops, 293 output drivers and 940 repeaters after placing and routing by software. Appendix B gives the VHDL code.

Upon successfully making the sampling frequency identical to the operating frequency of the FPGA, the instantaneous power consumption for the sensing/actuation mode can be reduced by using Dynamic Frequency Scaling (DFS). In contrast to DPM which saves power by controlling on/off status, DFS dynamically adjust the operating frequency of the processor to manage power consumption [32]. For any processors, its power consumption may be expressed as [33],

$$P_d = kV^2C_Lf \quad (2.1)$$

where k is the switching activity constant., C_L is the load capacitance, f is the clock frequency and V is the supply voltage. It can be seen from this equation that the power consumption is proportional to the clock frequency. While low-power techniques applied during IC design and manufacture enables lowering the supply voltage and the load capacitance, it is desirable to operate the processor in the lowest frequency to reduce the instantaneous power consumption. It also reveals the reason why continuous improvements

are needed to make the sampling frequency identical to the operating frequency.

Figure 2.9 gives an example to show the relationship between the power consumption (represented by the current) and the clock frequency. The data is generated by Figaro after completely placing and routing of some test codes with different complexities. Four lines with different utilizations are presented in slopes of 0.51, 1.07, 1.91, and 2.89 mA/MHz. It may be seen from the figure that the power consumption is also proportionally related to the resource utilization. Subtle differences in the clock frequency and utilization mode may reduce or increase power consumption considerably.

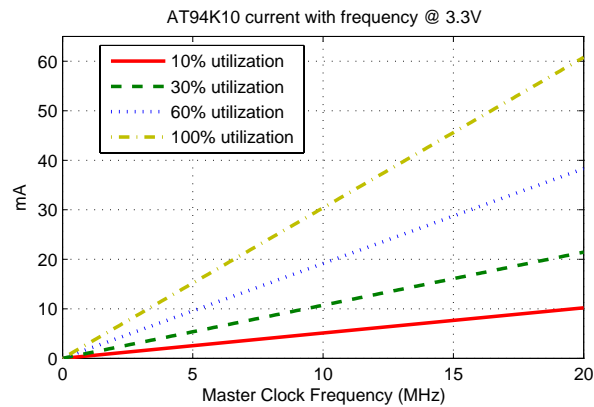


Figure 2.9 Current consumption for a fully routed FPGA (AT94K10)

DFS are usually implemented by using adjustable oscillators. There are two types of adjustable oscillator. The first type is statically programmable oscillator which outputs clock pulses in pre-programmed frequency, which is not suitable for DFS since it requires external programmers to change the frequency. The second type is MCU programmable oscillator based on PLL (Phase Lock Loop) technology. However, the accuracy of the second type oscillator is low. A representative chip is DS1077L, which can be online programmed to dynamically change the output frequency from 4.87 kHz to 66.666 MHz, can only guarantee accuracy of 1.25%, in comparison to 150 ppm for normal crystal based oscillator. Thus, both types of adjustable oscillators may not be used in wireless sensors since timing accuracy is

also critical for sensing.

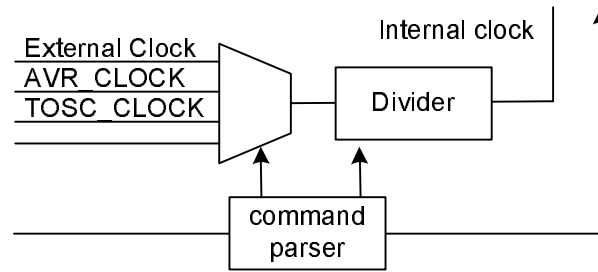


Figure 2.10 DFS implemented inside FPGA

Noticing the power consumption of FPGA is related to the utilization and the main frequency, a software approach may be adopted alternatively in FPGA to realize DFS. The basic idea is to construct a clock generator in FPGA to provide clock to the FPGA itself. Although the clock generator is constantly run in high frequency, it consumes insignificant power since it only needs a very small fractional utilization of a FPGA. Figure 2.4 presents such an implementation including a command parser, a multiplexer and a divider. The command parser receives instructions, controls the multiplexer to select desired clock signal, and sets the factor used by the divider. The output signal from the clock generator is then used to supply the internal clock signal to the rest part of the FPGA. Normally, the internal clock can be deactivated by setting the factor of the divider to be zero, and only the command parser is constantly clocked by the slowest clock, TOSC_CLOCK which is 32.768 kHz in the figure, to monitor commands.

2.4 A New Architecture of Wireless Sensor for Active Diagnosis

The discussion in this chapter has given the demonstration that how parallel controlling can improve power efficiency for data acquisition, and also has given us inspiration and strong motivation to design a new architecture for wireless sensors which are capable of high speed data acquisition. The architecture should adopt the advantages of the

conventional wireless sensor that may be beneficial for low speed applications, whereas it should enable power efficient operations for high speed applications.

Compared with CPLD, FPGA offers more flexibilities and resources due to the smaller size of logic block. In the past, FPGA was used for fast ASIC (Application Specific Integrated Circuit) prototyping. ASIC designs were tested by being prototyped in a FPGA until it is close to meeting the requirements. By designing systems to fully use the capability of FPGA, it is possible to create systems providing high flexibility in the field. Because of the limited current source capability of MICA motes, the previous improvement did not use FPGA. For a totally new design, it may be feasible to use FPGA within affordable power budget with dedicated power management.

A wireless sensor may have extremely complex operations. It is nearly impossible to build a finite state machine to cover all complex logical functions for wireless sensors within a single FPGA due to the limitation of resources and technical issues. An instruction based processor is still preferred to handle normal operations. It must be noted that an instruction based processor may be designed and implemented in a FPGA (or so called soft-core MCU). Thus, a single FPGA can serve as both types of processors. However, such approach may be impractical for wireless sensors from the viewpoint of efficiency: to implement a full functional MCU, a large amount of gates is required which increases the requirement of density of FPGA and correspondingly costs and power consumption. Consequently, combining COTS FPGA and MCU and adopting their advantages is still the best approach for wireless sensor design with discrete components.

Figure 2.11 illustrates the proposed architecture for high speed wireless sensors and graphically presents the idea discussed in this chapter. The core of the architecture is that

dual processors co-exist together: one for normal operations and the other for high speed data acquisition/actuation. Corresponding to the processors, two types of storage devices may be needed: a volatile type memory for high speed and a non-volatile type memory for permanent storage. Notably, three bold lines indicate two different data buses and an interface between two processing units. The interface may have a great variety of forms, such as shared memory, interrupts and etc. Since the two data buses are irrelevant, sensing/actuation can be precisely made while other operations, such as wireless communication and data processing, can be running concurrently.

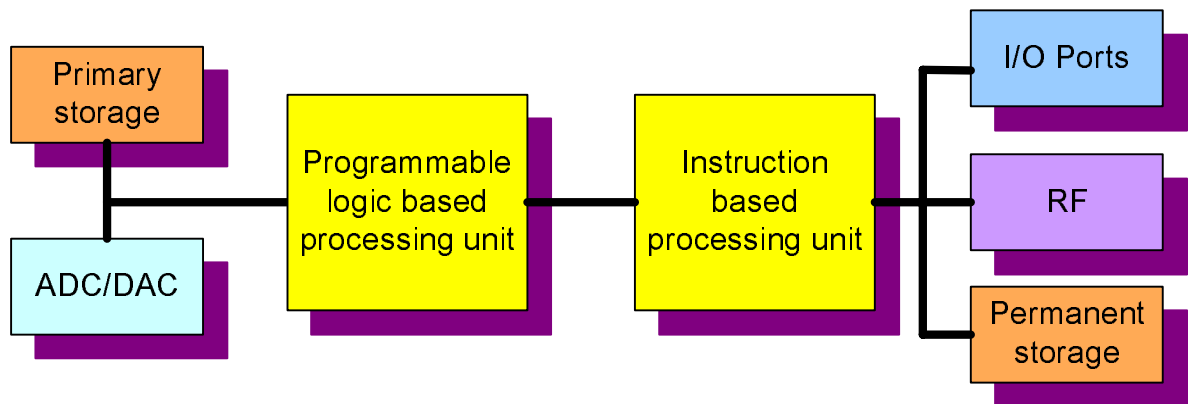


Figure 2.11 A new architecture of wireless sensor for active diagnosis

3 Wireless Sensor Design with the New Architecture

To keep good extensibility and flexibility for potential applications, wireless sensor must be designed with a scalable modularized framework, although our initial goal aims to develop an experimental prototype platform for active diagnosis with piezoelectric sensors/actuators. A modularized framework consists of a unique-defined interface and multiple modules which are individually responsible for one or several particular operations. As embedded system technologies continue to evolve, each individual module can be easily upgraded and customized for balancing the performance, power budget, and cost. This chapter will first establish the modularized framework for wireless sensor, and then address the design and the particular implementation for all modules in detail.

3.1 Modularized Framework for Wireless Sensor Design

In general, a wireless sensor node is a combination of an embedded data acquisition system and a processing system. Several sub-modules can be classified by tracing data flow:

- *Signal Conditioning*: Sensors convert ambient variables (strain, pressure, acceleration, etc.) into electrical signals with varying density and various forms, such as voltage, current or charge. The raw signals from sensors may be weak and noisy. Signal conditioning circuits for filtering, compensating, and amplification could be used to improve signal quality by de-noising and/or removing unwanted frequency bands and adjusting output signal in proper form (amplitude and offset).
- *Analog to Digital*: The conditioned analog signal needs to be accurately encoded into digital data for further processing. As digitally discrete encoded data do not usually represent the true nature of information in the continuous analog data, the

- requirements of resolution and speed must be carefully assessed.
- *Digital to Analog*: For applications such as active diagnosis which require initiating signal generation, the sensor node must be capable of converting digital data into analog signals to drive transducers.
 - *Data storage*: A massive repository device is required for persistent data storage. Although MCU may employ certain types of memory (program flash, EEPROM, SRAM), the internal memories are usually dedicated for particular purposes and limited in size. Especially for application that requires high sampling rate, the storage device with high I/O throughput capability is critical to handle the input data stream.
 - *RF communication*: A sensor node must be capable of transmitting/exchanging information with the outside physical world. There are numerous radio standards and protocol, as well as COTS radio devices. Frequency band, modulation format, protocol and data rate have to be taken into consideration.
 - *Processor*: A core device(s) for controlling and computing is essential to provide intelligence to the sensor nodes. Many types of processors exist with subtle differences, such as MCU, DSP (Digital Signal Processor) and FPGA. Wireless sensor applications usually favor low power MCU. However, when fast I/O throughput is of concern, the choice of processor needs to be re-evaluated.
 - *Power regulating/scavenging*: Energy supply is a critical factor for wireless sensors. As most prototypes are powered by batteries at present, many researchers are working on power scavenging device to accumulate/convert ambient energy into electricity. Besides that, power regulation must be included to provide a stable power supply for ICs and to optimize operations of the energy sources. Additionally, power regulation

may need to handle requirements for multiple voltage levels. For example, in active diagnosis, higher voltage is required to drive transducers.

- *Others*: Besides the above essential parts, miscellaneous circuits fall into this catalog. For instance, various interfaces to allow human intervention may be needed.

To setup the framework, these sub-modules must be further grouped into several modules by examining their relationships and evaluating the inter-connectivity. For good extensibility, the inter-connection interface should be designed to be as flexible as possible. These sub-modules, which interact tightly and have numerous electrical connections, need to be put into one module to avoid occupying too much of the inter-connection interface. Moreover, noise sensitive sub-modules, such as analog circuits, need to be located away from high speed digital circuit to minimize interference and retain signal fidelity.

Under these considerations, a three-module basic configuration, which may also include actuation in the future, may be designated for COTS based wireless sensors. As shown in Figure 3.1, the core module is the *processing module* which includes all necessary operations for a basic data acquisition system. The processing module can be readily tailored and replaced to fit varying demands of speed, power budget, and cost.

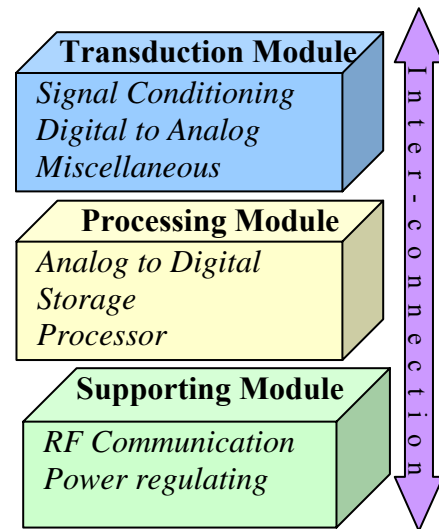


Figure 3.1 Module classification for COTS based wireless sensors

Another advantage for this arrangement, especially of high speed applications, is that a vast number of connections between the external storage and the processor can be hidden inside the module. Thus, inter-connections among modules which are limited by physical

restrictions can be reserved. Below the processor module, the *supporting module* is constructed by combining RF communication and power regulating sub-modules. Using separate sub-module for RF enables easy migration to accommodate versatile communication protocols. The *transduction module* mainly contains an analog circuit for signal conditioning. Signal from transducers is pre-conditioned in this module to reduce the disturbance from high frequency digital signals. For active diagnosis applications, this module can be designed with an add-on digital-to-analog sub-module for driving transducers. Depending on the application, the modular configuration is versatile while complying with the same interconnection definition. Four or more modules can be connected through for more functionality. Modules of the same type, but with different implementation, may have multiple instances and can co-exist in a single system. For example, power scavenging and human intervention interface can be implemented as independent modules, and two or more transduction modules can be stacked together to support more types of sensing simultaneously.

To achieve compactness, 3D stack style design was chosen for physical layout as an improvement of a previous version [29] and as inspired by the Motes. However, since the Motes has only one 51-pin connector, the connection is not structurally strong, especially when pressure or vibration is present. To improve reliability, the previous design used a pair of through-hole 1.27 mm headers and sockets on opposite edges. Nevertheless, such miniature headers suffer from deformation after several times of mating. In this design, a specific module corresponds to a physical printed circuit board (PCB), and the interconnections are made through four surface mounted fine pitch connectors. Connectors are placed along with the board edges. Two connectors on each side are perpendicular to each

other to ensure reliable connections and to obtain maximum useable area for IC placement. As many PCBs can be stacked as desired, modules do not necessarily have to be adjacent to have a direct communication channel.

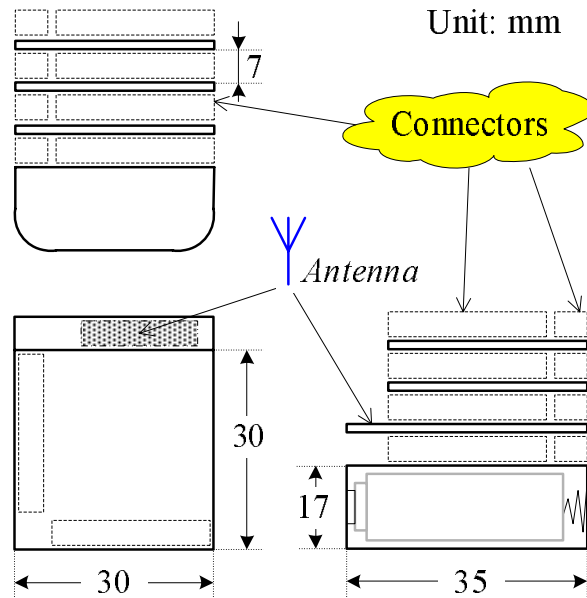


Figure 3.2 Board to board layout of the wireless sensor

The physical dimension was decided by scrutinizing potential components with the largest footprint and power supply. Although extreme miniaturization is not practical without an application-specific integrated chip, a design with discrete components is still expected to be as compact as possible. Since two N-size batteries were chosen as the primary energy source, the PCB was designed in square shape with 30mm along each side with an exception for the supporting module which is immediately adjacent to the battery holder and has an extra 5mm in length. Printed antenna or surface mounted antenna for RF communication can be placed in this area and protruded underneath other modules to avoid attenuation of radio strength. Experiences learned from previous work also reveal that such placement can effectively reduce the noise from radio radiation and enlarge radio coverage. All other modules follow the 30mm square and then can be stacked on top of the bottom board. A

sketch of layout from different views is shown in Figure 3.2. There is a total of 50 inter-connections available for connectivity through the connectors which are represented by rectangles with dash line in the figure. Each connector is a 1 mm pitch miniaturized socket or receptacle with 25 pins with polarization, thus eliminating the possibility of incorrect connection. Although more inter-connections can be added by choosing connectors with smaller footprints, difficulties with routing will result in more PCB layers, and smaller or buried vias will be required with increased cost.

3.2 Processing Module

Based on the discussion made in Section 2.4, implementation of the processing module is made by using a FPGA with a dedicated 8-bit hardware MCU core, AT94K10AL from Atmel®, because of its high integration, compact package and low power feature. The chip has distributed 10ns programmable synchronous/asynchronous dual port SRAM, 8 global clocks, cache logic ability, and 10k usable gates in FPGA part, in addition to the enhanced RISC architecture based MCU core [34]. A 40k gates version, AT94K40AL is also available with the same footprint to provide more usable resources. For the preliminary prototype and initial experiments, the 10k gates version is used for the controlling cores of high speed data acquisition/actuation. When other IP cores for arithmetic algorithms are required, the chip can be readily replaced by the 40k version.

Three clock sources, running at 32.768 kHz, 4 MHz and 10 MHz respectively, are included to enable subtle power management and fulfill speed requirements. Both the 32.768 kHz and the 4 MHz clocks are made through external crystals and internal circuits of the MCU core. For normal operations, the one with high frequency will run the MCU at 4 MHz (which is the same speed implemented in MICA Motes); whereas for power-down operation,

the one with low frequency provides an accurate asynchronous timer to enable the MCU to be vigilant to events, such as remote wakeup messages. The fastest clock source, which is also controlled by the MCU, is used to operate the FPGA at 10 MHz for high speed requirements. In the case where no high speed operations is required, the clock can be disabled to completely halt the FPGA, consequently reducing power consumption to a comparable level with other wireless sensor prototypes which use centralized architecture. Additionally, with a built-in software clock multiplexer inside the FPGA, the operating frequency of the FPGA can be dynamically switched among the three global clock sources. This function provides high feasibility in managing the power.

A monolithic, 10-bit, 20msps ADC, AD9200 from Analog Devices [35], and a 4 Mb (256k × 16-bit) SRAM with 55 ns access time consists of the part for data acquisition. The FPGA provides a software generated clock to the ADC. The maximum sampling rate is up to 10 msps as the FPGA operates at 10 MHz. With that sampling rate, the SRAM can hold up to 40 ms data.

The FPGA core is internally divided into several function modules as given in Section 2.3.3. Ultimately, only one clock cycle is needed for a sensing cycle by dedicated program in VHDL, thus the power consumption for sensing is reduced to a minimum level. This program and the program running in the MCU are both stored in a 512 kB serial FPGA configuration EEPROM and loaded at system power-up with in-system programmability.

All components are mounted in a four layer PCB. The board is partitioned into two areas. The northeastern area with larger size is allocated for digital circuits, while the southwestern area with smaller size is designated for analog circuits. A picture that shows both top and bottom sides of the assembled processing module are presented in Figure 3.3.

All unused ports from the FPGA core are routed to connectors, along with I/O ports from the MCU for future extension. The west side connector in the top side is dedicated for digital I/Os, mainly connected to the MCU. Modules which only require low speed serial access can use I/O ports from this connector. The south side connector is assigned to be a combination of power lines, analog I/O, and digital I/Os from the FPGA. One power line is to supply regulated 3.3 Volts. All the components are powered by this power line, while analog supply decoupling is implemented locally in the processing module. The other power line is reserved for direct connection to batteries. To minimize potential crosstalk noise, a dedicated analog ground connection is placed in-between.

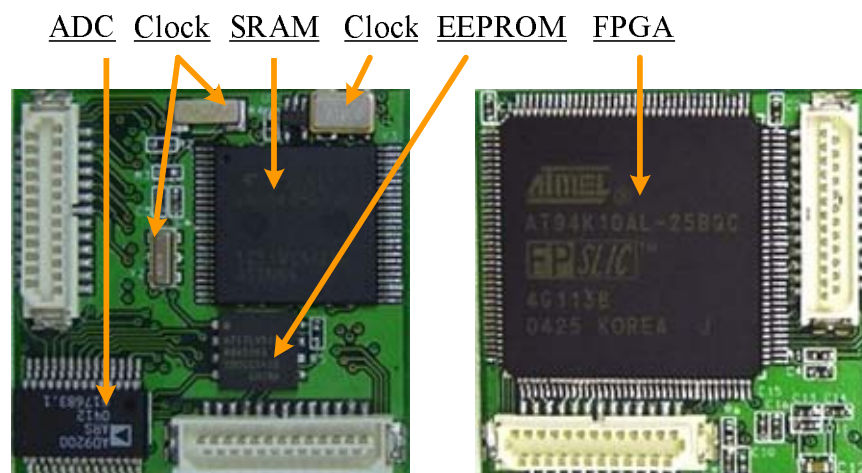


Figure 3.3 Pictures of the processing module

3.3 Supporting Module

The supporting module is another essential part of the wireless sensor design. According to the definition given in the Figure 3.1, the supporting module must provide communication support through wireless channels and stable energy supplies with its two sub-modules, which will be analyzed and addressed separately.

Because batteries are used as the primary energy source, power regulation is critical for the robustness and the life of the sensor. If no power regulation is applied, wireless

sensors may malfunction once the batteries' voltage falls below the cutoff voltages of one or several components. Analog circuits even have stricter requirements on the purity of voltage supply to keep accuracy. For example, both the radio transmission power and reception sensitivity may be proportional to the voltage provided to the radio. Several switching technologies, capacitor-based and inductor-based, are usually used to elevate and regulate voltage [36]. In capacitor-based converters, semiconductor switches are controlled to charge and discharge capacitors through different paths to produce an output voltage on an output capacitor proportional to the input voltage; In inductor-based converters, DC input voltage is chopped into short current pulse in an inductor to charge an output capacitor, and then obtain changed voltage. Regulation in both converters is done through adjusting switching duty cycle by monitoring the in-circuit current or voltage. Compared to the inductor-based converter, the capacitor-based converter has extra power loss during charging since the voltage over the output capacitor is not continuous. However, the inductor based converter may have larger physical volume due to the size of the inductor.

For COTS components based wireless sensor, it is believed that the inductor based converter is better since power efficiency has higher priority than volume. More concretely, since COTS inductors have standard package, optimal balance between the capacitance and the volume of the output capacitor must be found empirically. A high efficiency DC-DC converter IC, TPS61016 from Texas Instruments Inc., is chosen to regulate the input power coming either from a directly connected battery packet or through an external power connector. The chip is based on a fixed frequency, current mode, pulse-width-modulation (PWM) controller. At light load, the chip can automatically goes into power save mode. Because a built-in synchronous rectifier is integrated, system efficiency is kept extremely

high. The power sub-module can provide 3.3V constant voltage to the entire wireless sensor node even when the batteries drop down to 0.9V.

As the IEEE 802.15.4 protocol is being widely accepted for energy constrained wireless sensor networks due to its extreme power efficiency, it was desirable to adopt this protocol to achieve compatibility among upgraded and other wireless sensor platforms. In the early stage of this research [37], a transceiver IC from Atmel was used as a wireless modem while the protocol stack is implemented in the software. Since all tasks, such as package encoding and decoding, is done in MCU, large amount of program space have to be occupied by protocol codes. To save the precious program space and accommodate full compatibility of IEEE 802.15.4, a specific transceiver, CC2420, is selected to replace the one in the previous design. The CC2420 is a low power and cost efficient, IEEE 802.15.4 compliant transceiver aimed at control and monitoring applications. The transceiver module provides 16-channel direct sequence spread spectrum modem with 2M chips/s and 250 kbps effective raw data rate in the 2.4 GHz unlicensed ISM band [38]. It is highly configurable with many integrated functions, such as programmable output power, data buffering, burst transmissions, hardware medium access control (MAC) encryption and authentication, clear channel assessment, signal strength indicator and battery monitor. Nominal effective transmission coverage is 10 to 75 meters. Extensive hardware support for packet handling, such as all physical (PHY) and some MAC functions, are implemented inside the chip, thus the size of program code can be vastly reduced. The configuration interface and transmit/receive FIFOs of CC2420 are accessed via an SPI interface.

Figure 3.4 shows the assembled supporting module. Two versions with different types of antenna are designed as shown in the thumbnails at right to validate transmission

range. The first type utilizes a multilayer ceramic surface mounted antenna. The antenna is originally designed for 2.4 GHz Bluetooth from Phycomp Ltd. It has omni-directional radiation pattern with 0db gain based on micro-strip theory. For comparison, another version with printed PCB antenna is also designed. As the chip antenna requires a particular ground plane, many circumstances, such as antenna mounting, the distances to adjacent components and the sizes of ground planes, may adversely affect antenna performance and radiation pattern. Since the available size for ground plane in the wireless sensor is much smaller than specified, we compared the performances of two types of board after initial assembling. Because a battery holder is placed right underneath the supporting module and may act as another ground plane to detune antenna, it was found that the printed PCB antenna is more reliable than the chip antenna. A socket for external antenna is also provided. If needed, high gain external antenna, or power amplifier can be cascaded to enhance communication range.

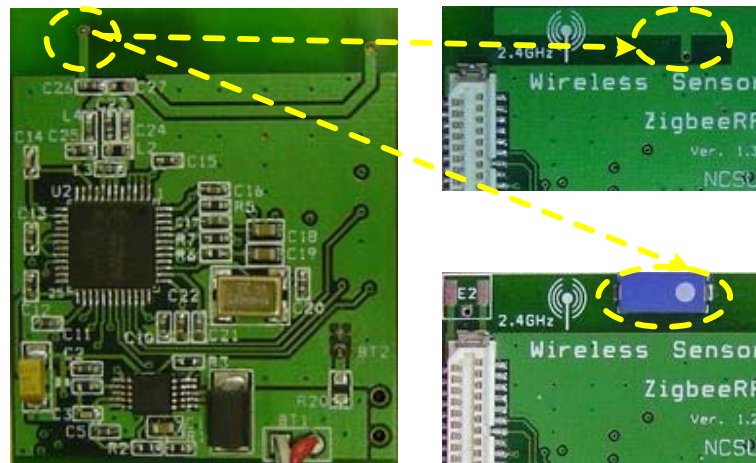


Figure 3.4 Pictures of the supporting module

3.4 Transduction Module

For SHM, crucial physical parameters including displacement, strain, acceleration, and temperature may need to be monitored to provide information about the behavior of a structure or environmental conditions. Two transduction modules have been developed for

fully supporting these measurements with multiple types of transducers.

The first transduction module specifically provides supports for piezoelectric sensors. Physically, a piezoelectric sensor has two electrodes with dielectric crystal in-between. In contrast to traditional strain gage, a piezoelectric sensor has many advantages, such as high sensitivity of electromechanical coupling, low power requirements, broad bandwidth, and low noise threshold. Thus, it is well suited in dynamic strain sensing, especially for detecting diagnosis waves. Electricity or charge will be generated when mechanical stress is applied on a piezoelectric sensor with the amount and the direction of electricity determined by the strength and direction of the stress. Typical output voltage is in the range of tens of μV while measuring diagnostic waves in structures, thus interfacing circuits with enough gain must be provided in the transduction module.

Two types of amplifiers, voltage mode and charge mode, can be used to provide gain for the signal generated from piezoelectric sensor, since a piezoelectric sensor can be modeled in two ways: a voltage source with a series capacitor and resistor, or a charge source with a shunt capacitor and resistor. For voltage mode amplifier, the induced voltage is presented in the high impedance positive input and amplified by the operational amplifier. However, the gain is related to the amount of capacitance seen from the input side of the operational amplifier. As the piezoelectric sensor has to be directly mounted on or embedded in structures, parasitic capacitance of the cable will affect the actual gain. As a result, the interfacing circuit must be calibrated whenever the cable is moved or replaced. In charge amplifier, the amplification is done through balancing the charges in the piezoelectric and the feedback capacitor. Thus, the stray capacitance associated with the interface cable will not affect the gain. Additionally, the configuration of the charge amplifier is inherently like a

first-order high pass filter and low frequency noise will be effectively reduced. Hence, the charge amplifier is better to amplify signals from piezoelectric sensors for active diagnosis.

A transduction module for piezoelectric sensor is designed with a charge amplifier. A piezoelectric sensor mounted on a structure with polarization perpendicular to the surface is wired to the board with a 2.54 mm header. When waves propagate through the sensor, bi-polar charge flow will be induced. To correctly handle the bipolar charge by a single supply circuit, a high input impedance differential charge amplifier circuit is designed. The first stage uses two charge pre-amplifiers. One amplifier is responsible for giving pre-amplification for positive charge while the other one for negative charge. The gains of both pre-amplifiers are exactly identical by matching the feedback resistors and capacitors. Another operation amplifier is configured as a difference amplifier with unity gain for the second stage. These two stages are connected as a classic instrumentation amplifier like architecture. Bi-polar charges can be converted and amplified by this configuration and shifted to the reference voltage. A third stage is also included to utilize a voltage mode amplifier for further amplification. Two chips with dual operational amplifiers are used as shown in Figure 3.5(a). To accommodate correct ADC interfacing, 2.0 V rail voltage from the ADC in the processing module is obtained from the connector and divided in half by a voltage follower to provide reference voltage. All these chips can be individually turned off for dynamic power management. Besides the sensing interface, this board also includes a simple interface for human interaction. Two tact switches can be used as external triggers and three LEDs in a single package can serve as indicators for interior status of MCU.

Another transduction module for strain gauge and acceleration is also designed and shown in Figure 3.5(b). Due to the low bandwidth nature of strain gages and accelerometers,

only low frequency signal can be measured by these devices. Although the ADC on the processing module can still be used, it is not very efficient because its power dissipation is slightly higher than that of a low speed version. A dedicated ADC for low speed application would help to conserve power and may obtain better resolution. Such an implementation also demonstrates the flexibility of the modularized design.

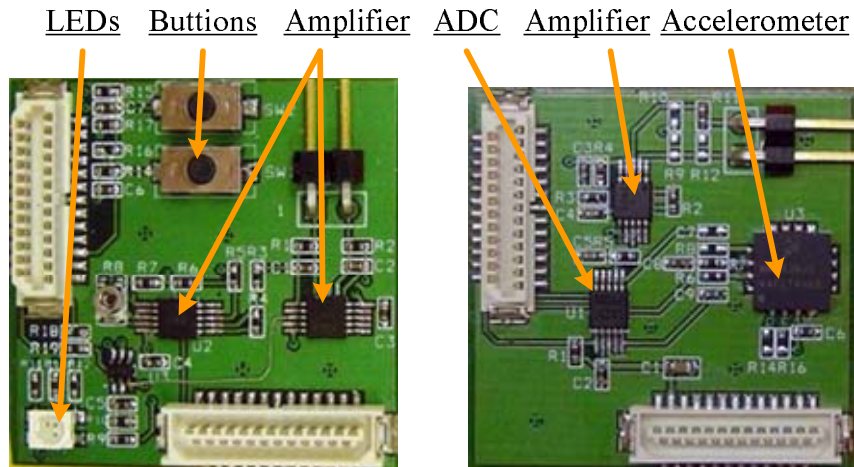


Figure 3.5 Pictures of the transduction modules: (a) Piezoelectric (b) Strain Gage and Acc.

A 4 channel, 12-bit, 1 msp/s ADC with serial interface, ADC124S021, is used as the secondary ADC on this transduction module. The ADC is individually controlled by a software program in the MCU via a three-wire bus. One channel is allotted to the strain gage and the other three channels are reserved to the three axes of an accelerometer. The strain gage can be wired to the header which is connected to an arm of a classic Wheatstone bridge. A wide-temperature, precision instrumentation amplifier is used to measure the differential voltage. The three-axis accelerometer, MMA7260, consists of two surface micro-machined capacitive sensing cells and a signal conditioning ASIC with shutdown mode. Its sensitivity can be dynamically adjusted with different sensitivities ranging from 1.5g to 6g. Transduction modules which can accommodate other types of transducers, e.g. gyro sensors, can be readily designed for different applications.

3.5 Interfacing Module

An independent interfacing module is designed to allow the processing module to be connected to computer via USB port. In-system programming, debugging and communication can be done through this module. By stacking the interfacing module to a processing module and a supporting module, a base station can be constructed to allow data exchange between wireless sensor network and computer.

A USB interface chip, FT232R, is used to convert USB packages to signal that is compatible with UART (Universal Asynchronous Receiver and Transmitter) interface with data rate up to 250 kbps. With the help of the USB chip, the MCU in the processing module can exchange data with the computer via the built-in UART interface. To enable programming, an extraordinary MCU dedicated as programmer is designed in the interfacing module. In normal mode, the MCU is attached to the UART bus and constantly monitors data on UART. When programming is required, a special command is sent by programming software in computer to activate the extraordinary MCU into programming mode. In the programming mode, the extraordinary MCU halts the FPGA/MCU on the processing module and puts the EEPROM into the programming mode by pulling the reset line low. The extraordinary MCU, then, reads the bit stream of the new program from the computer and writes the content to the EEPROM according to the EEPROM's programming specification. An inexpensive MCU, Atmega48, is chosen and programmed for the preceding task. In addition, an on-board low dropout voltage regulator enables convenient use of power on the USB bus. When other modules are connected to the interfacing module, no batteries are required. A picture for assembled interfacing module is shown in Figure 3.6.



Figure 3.6 Picture of the interfacing module

3.6 Verification and Summary

The wireless sensor design presented in this chapter is an improved version of a preliminary design [37] for the proposed architecture described in Chapter 2. Built entirely from COTS components, it provides a proof-of-concept platform for enabling active diagnosis with wireless sensor for SHM.

Figure 3.7 shows different views of how individual modules are stacked to form a compact wireless sensor. An assembly of a wireless sensor with a transduction module, a supporting module and a processing module is shown in the picture (a), while views from different sides are shown in pictures (b) (c) (d). The supporting module is the bottom board which is attached directly to the battery holder and wired to the batteries. The processing module is in the middle with up-side/down-side connectors to make interconnections to the supporting module and the transduction module which is the topmost board in the picture. More modules can be stacked on the topmost module as long as it has the same interface, and the sequence of these modules can be arbitrarily arranged.

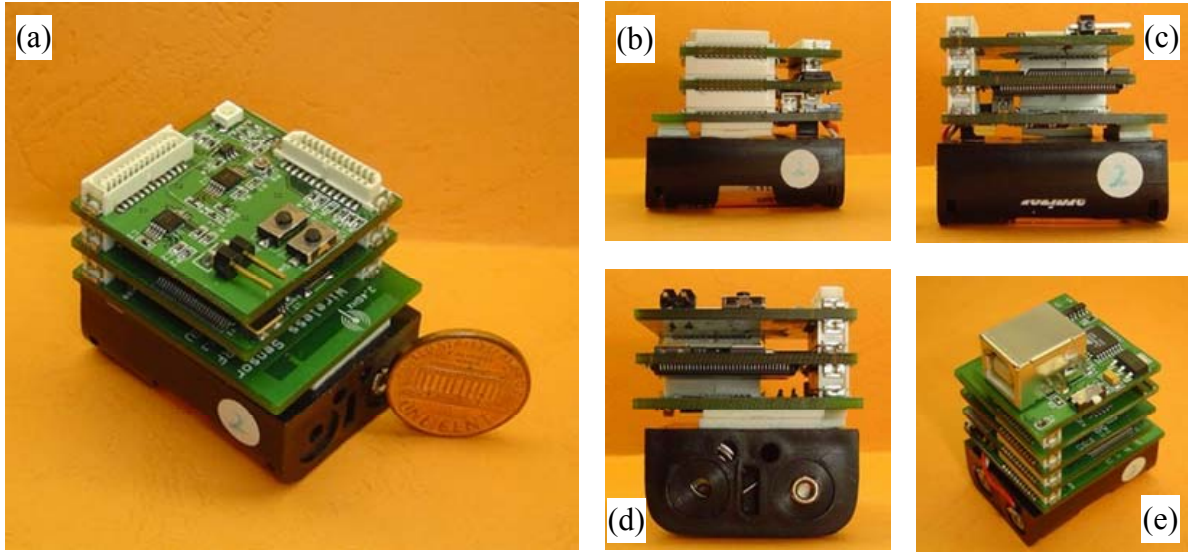


Figure 3.7 Pictures of fully assembled wireless sensor

Various applications can be constituted in such a manner. For example, a wireless sensor can have two transduction modules to enable both piezoelectric and accelerometer. A wireless sensor solely used for networking (i.e. routing and repeating) can just have a supporting module and a processing module. Also, wired calibration system can be constructed by just using a processing module, a transducer module and an interfacing module. Shown in the picture (e), a demonstration of the configuration for interfacing and programming includes an attached interfacing module and two transduction modules.

To validate the performance of the wireless sensor, experiments were conducted with different setups. In the first setup, a wireless sensor including a transduction module with the support of piezoelectric sensor is used to record wave propagation in an aluminum plate to verify the speed and the accuracy. The distance between the sensor and the excitation source is 16.26 cm (6.4 inch). Figure 3.8 shows the time-series signal collected at the wireless sensor with 4 MHz sampling rate. In this experiment, the central frequency of the excitation signal was set to 40 kHz with amplitude of ± 40 V, and the group velocity of the

corresponding flexure wave is 2107 m/s. The unit of the vertical axis is $2V/1024$ which is obtained from the ADC specification. From the figure, it can be clearly seen that the first wave packets can be identified as the propagating wave travel through the plate from the actuators to the sensor along the shortest path since the shape and the arrival time are consistent with theoretical interpretation. After the first wave packet, reflections from plate boundaries will be observed. This is manifested from the signal which includes the synthesized wave packets around and after $400 \mu\text{s}$. In practice, only the first wave packet is of interest, and the reminder can be neglected or even not be collected in SHM.

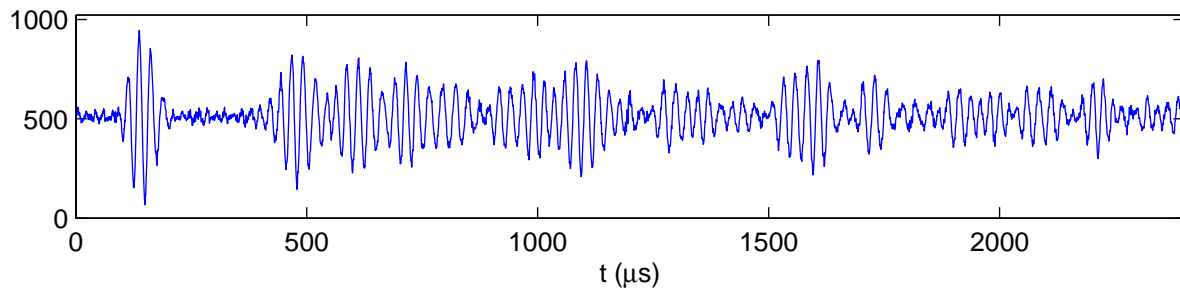


Figure 3.8 Data collected by the wireless sensor with 4 MHz sampling rate

To validate the accuracy, a series of tests based on similar configurations were made with the help of a digital oscilloscope (Tektronix TDS420A) used to provide reference for comparison. Three collected data sets are plotted in Figure 3.9. The central frequency of the excitation signal is set to 40 kHz, 90 kHz and 200 kHz, respectively. The sampling rates of both the wireless sensor and the oscilloscope are set to 10 MHz. For the excitation at 40 kHz and 90 kHz, it can be seen that the data collected by the wireless sensor are almost identical to the data collected by the oscilloscope, and the curves in each picture almost entirely overlaps together. For the excitation at 200 kHz, minor differences can be observed.

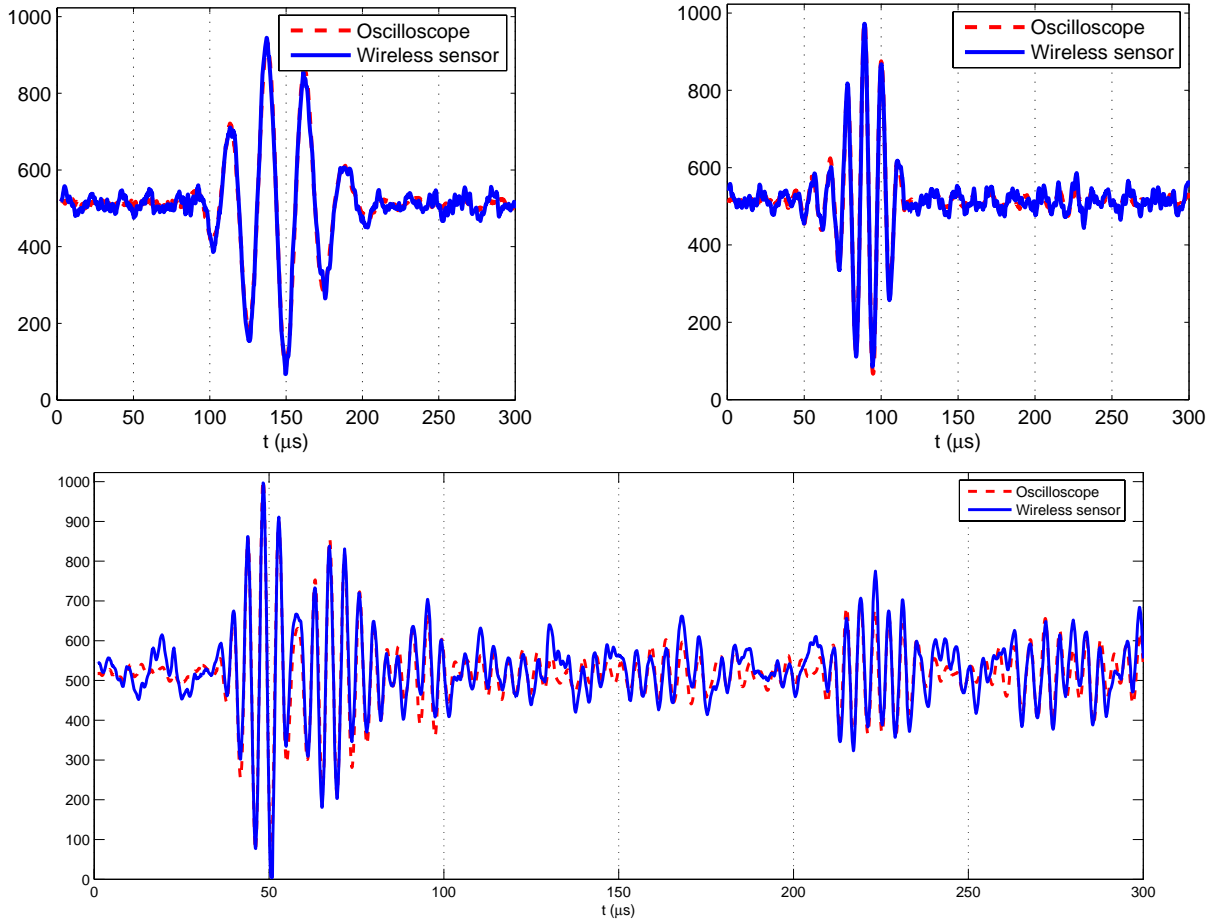


Figure 3.9 Comparison between data collected by the wireless sensor and an oscilloscope

Another experiment to verify the performance of low frequency applications is made to measure accelerations. The transduction module in the previous experiments is replaced by the one with an accelerometer and an external ADC. With ultra-low power consumption, this configuration is suited to real-time monitoring for low frequency applications. It must be noted that the frequency bandwidth is now determined by the RF communication rate since it is usually far below the I/O speed within the wireless sensor. A small shaker is used as the acceleration source and driven by the same function generator and the amplifier in the last experiments. The wireless sensor is mounted on the top of the shaker to measure acceleration with program written for real-time sensing. Since the data rate of CC2420 is about 2 kB/s, the sampling period is set to 2 ms and implemented by a timer in the MCU. Additionally, a wired

ceramic accelerometer, PCB352C22 from PCB Piezotronics, are mounted to the wireless sensor with a unity gain signal conditioner (482B06) to quantify the accuracy of the wireless sensor. It has to be noted that the output of the shaker does not strictly follow the driving signal because the power amplifier used is not within the manufacturer’s recommendation to provide large load. However, the wired accelerometer should be able to provide precise reference for the purpose of comparison with arbitrary signals.

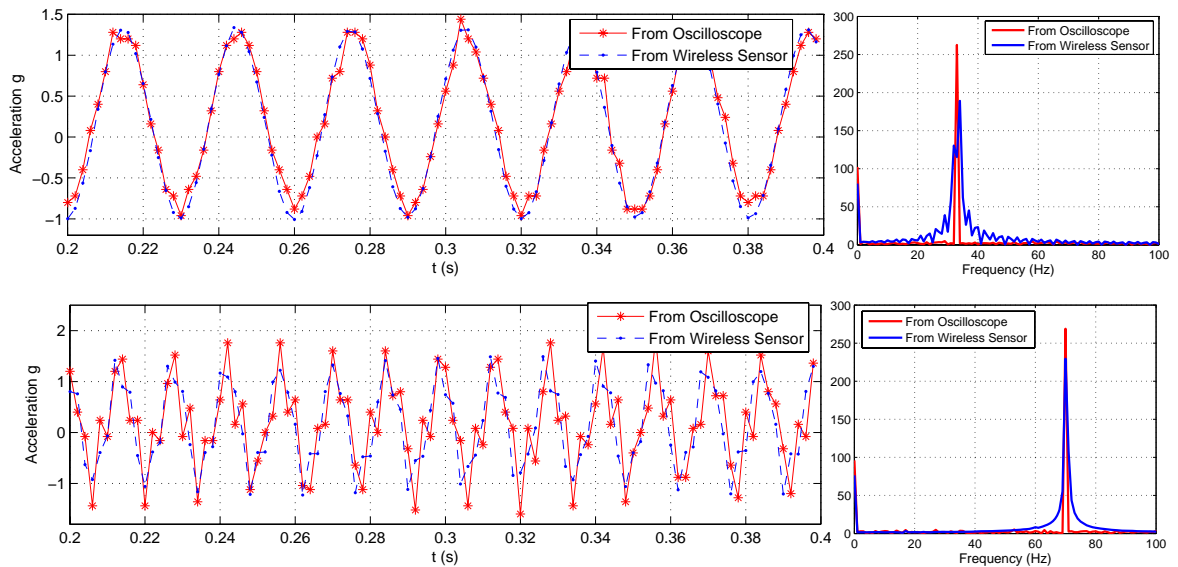


Figure 3.10 Real-time acceleration measurement and comparison

Figure 3.10 gives the comparison between the signals collected by the wireless sensor and the wired accelerometer under 33 Hz and 70 Hz sinusoid driving voltages on the shaker. From the figure, it can be seen that the data collected by the wireless sensor matches well with the data collected by the oscilloscope. Since the wired accelerometer has higher sensitivity and the oscilloscope has higher sampling rate, minor differences can also be observed around the peaks of the curves. For the case in which the frequency of driving signal is 70 Hz, the differences are slightly larger. This is due to the limited sampling rate in the wireless sensor which is set to 500 Hz to enable real-time transmission. Some

information of signal on high frequency band may be lost. Nevertheless, high frequency acceleration is not of interest in civil SHM applications, nor is the real-time transmission required.

These experiments have shown that the wireless sensor have good accuracy comparing to conventional approach. The sampling rate can reach at a maximum 10 MHz with the current hardware configuration. This unique feature enables the wireless sensor to be readily used to capture ultrasonic signal, such as foreign impact, acoustic emission, and etc.

Table 3.1 summaries the performance specification of the wireless sensor design.

Table 3.1 A summary on the hardware specification of the wireless sensor

	Attributes	Value with default configuration	Remarks
Processing Module	MCU clock speed	4 MHz	up to 20 MHz
	FPGA clock speed	10 MHz	external up to 20 MHz
	Sampling speed	10 MHz	adjustable by changing clock
	ADC channel	1	extendable on transducer module
	ADC resolution	10 bits	
	EEPROM	512 kb	up to 4 Mb
	External SRAM	4096 kb	256k × 16 bits
Supporting Module	Regulated voltage	3.3 volts	
	Startup voltage	0.8 volts	
	Current capacity	up to 200 mA	
	Radio frequency	2.4 GHz	16 channels
	Radio data rate	250 kbps	
	Radio current	18.8 mA (Rx)/ 17.4mA (Tx)	0.02 μ A in sleep mode.
	Radio range	20 m	indoor w/ PCB antenna
Transduction module	Piezoelectric support	Yes	For piezoelectric sensor
	Pass band	4 kHz – 500 kHz	
	Output range	0 volts - 2.0 volts	
	Stain gauge & accelerometer	Yes	with external serial ADC for strain gage and accelerometer
	Resolution	12 bits	
	Pass band	0 Hz – 1.5 kHz	
	Output range	0 volts – 3.3 volts	
Overall	Primary power supply	Dual N batteries	
	Interconnections	Dual 25-pins	
	Size	30 mm× 35 mm× 35 mm	with battery holder

4 Elastic Wave Propagation in Isotropic Plates

For active diagnosis, the characteristic of elastic wave propagation must be first investigated and modeled. Higher-order plate theory is used to derive dispersion relations, phase velocities and group velocities for isotropic plates. Due to the nature of dispersion occurred in wave propagations, a transient wave suffers from distortion, which makes methods to identify propagation distances by using the shape or phase information to be inexact. To use those methods to interpret dispersed waves, a linear mapping algorithm is developed to remove dispersion and recompress dispersed waves. Additionally, an energy decay model is developed to be used in active damage localization.

4.1 Dispersion Relations based on Higher-Order Plate Theory

Stress wave propagation in elastic medium has been thoroughly investigated over decades and can be found in the literature [19, 39-43]. In an infinite isotropic elastic solid, an arbitrary disturbance is propagated by means of three types of bulk waves, longitudinal (P) waves, shear vertical (SV), and shear horizontal (SH) waves, each traveling with its own constant velocity. For thin plate-like structures, the longitudinal and vertical shear waves experience repeated reflections at the upper and lower surfaces alternately and the resulting disturbance propagation from their mutual interference is guided by the plate surfaces and is directed along the plate, which can be effectively modeled by imposing surface boundary conditions on the equations of motion. However, dispersion phenomenon exists, that is, the velocity of propagation of a disturbance along the plate being a function of frequency, or equivalently, wavelength. Consequently, the shape of the signal of a wave packet (a short-time wave train) may vary with the distance and time of propagation.

For thin plates, constitutive relations are traditionally established on the classical plate theory or the first-order shear deformation plate theory. The classical plate theory, which is based on Kirchhoff hypothesis, which assumes that straight lines perpendicular to the mid-plane before deformation remain straight and normal to the mid-plane after deformation, and hence neglects transverse shear deformation effects. The first-order plate theory was developed by Mindlin by taking the effects of transverse shear deformation and rotary inertia into account [41]. Compared with both theories, higher-order plate theory can represent the kinematics better and yield more accurate stress distributions. Here a displacement approach for the solutions based on the higher-order plate theory has been recently formulated by [54] to describe the wave behavior in linearly isotropic thin plates, that is, solving the displacement equations of motion directly. This method may be further extended in analyzing anisotropic plates, i.e. composites.

4.1.1 Formulation of the higher-order plate theory

Considering an infinite plate of constant thickness h , the origin of a Cartesian coordinate system is defined to be located in the central $x_1 - x_2$ plane with the x_3 -axis being normal to this plane, as shown in Figure 4.1.

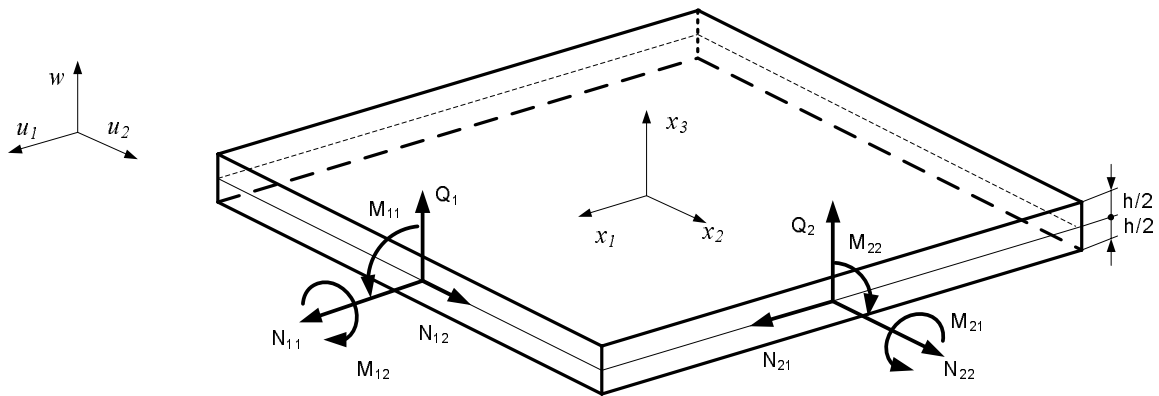


Figure 4.1 Sign convention for the displacements, stress and moment resultants in a plate

The stress and moment resultants, per unit length, can be defined as in the following terms [44]:

$$(N_{11}, N_{22}, N_{33}, N_{12}, Q_1, Q_2) = \int_{-h/2}^{h/2} (\sigma_{11}, \sigma_{22}, \sigma_{33}, \tau_{12}, \tau_{13}, \tau_{23}) dz \quad (4.1)$$

$$(M_{11}, M_{22}, M_{12}, R_1, R_2) = \int_{-h/2}^{h/2} (\sigma_{11}, \sigma_{22}, \tau_{12}, \tau_{13}, \tau_{23}) z dz \quad (4.2)$$

$$(S_{11}, S_{22}, S_{12}) = \frac{1}{2} \int_{-h/2}^{h/2} (\sigma_{11}, \sigma_{22}, \tau_{12}) z^2 dz \quad (4.3)$$

and the stress-strain relations at surfaces ($z = \pm h/2$) with respect to x_3 -axis can be given by:

$$\begin{Bmatrix} \sigma_{11} \\ \sigma_{22} \\ \sigma_{33} \\ \tau_{23} \\ \tau_{13} \\ \tau_{12} \end{Bmatrix} = \begin{bmatrix} C_{11} & C_{12} & C_{13} & 0 & 0 & 0 \\ C_{12} & C_{22} & C_{23} & 0 & 0 & 0 \\ C_{13} & C_{23} & C_{33} & 0 & 0 & 0 \\ 0 & 0 & 0 & C_{44} & 0 & 0 \\ 0 & 0 & 0 & 0 & C_{55} & 0 \\ 0 & 0 & 0 & 0 & 0 & C_{66} \end{bmatrix} \begin{Bmatrix} \varepsilon_{11} \\ \varepsilon_{22} \\ \varepsilon_{33} \\ \gamma_{23} \\ \gamma_{13} \\ \gamma_{12} \end{Bmatrix} \quad (4.4)$$

In modeling the transient wave propagation of thin plate structures using two-dimensional plate theory, rather than three-dimensional elasticity theory, it is possible, in principle, to expand the displacement field of a plate in terms of the thickness coordinate up to any desired degree. To account for the effects of transverse shear deformation and rotary inertia and to improve the accuracy of the extensional wave motion by taking the first-order normal strain and second-order transverse shear strains into consideration, a consistent displacement field may be presented by expanding the terms up to the second-order:

$$\begin{aligned} u_1(\mathbf{x}, z, t) &= u(\mathbf{x}, t) + z\psi_1(\mathbf{x}, t) + z^2\phi_1(\mathbf{x}, t) \\ u_2(\mathbf{x}, z, t) &= v(\mathbf{x}, t) + z\psi_2(\mathbf{x}, t) + z^2\phi_2(\mathbf{x}, t) \\ u_3(\mathbf{x}, z, t) &= w(\mathbf{x}, t) + z\psi_3(\mathbf{x}, t) \end{aligned} \quad (4.5)$$

where $\mathbf{x} = (x_1, x_2)$ and the x_1 - x_2 plane is chosen to lie along the mid-plane of the plate. The

generalized displacements (u, v, w, ψ_1, ψ_2) have the same physical meaning as in the first-order shear deformation theory [40-42], and three additional linear and quadratic terms of z associated with ψ_3, φ_1 , and φ_2 are added to the expansion of the displacement field. Note that the displacement field given by Eq. (4.5) suggests that the transverse normal to the mid-plane will induce elongation or contraction [45, 46]. The linear strains associated with the displacement field are

$$\begin{aligned}\varepsilon_{11} &= \varepsilon_{11}^{(0)} + z\varepsilon_{11}^{(1)} + z^2\varepsilon_{11}^{(2)}, \quad \varepsilon_{22} = \varepsilon_{22}^{(0)} + z\varepsilon_{22}^{(1)} + z^2\varepsilon_{22}^{(2)}, \quad \varepsilon_{33} = \varepsilon_{33}^{(0)} \\ \gamma_{12} &= \gamma_{12}^{(0)} + z\gamma_{12}^{(1)} + z^2\gamma_{12}^{(2)} \\ \gamma_{23} &= \gamma_{23}^{(0)} + z\gamma_{23}^{(1)}, \quad \gamma_{13} = \gamma_{13}^{(0)} + z\gamma_{13}^{(1)}\end{aligned}\tag{4.6}$$

where

$$\begin{aligned}\varepsilon_{11}^{(0)} &= u_{,1} \\ \varepsilon_{11}^{(1)} &= \psi_{1,1} \\ \varepsilon_{11}^{(2)} &= \varphi_{1,1}, \dots \\ \varepsilon_{33}^{(0)} &= \psi_3 \\ \gamma_{13}^{(0)} &= \psi_1 + w_{,1}, \quad \gamma_{13}^{(1)} = 2\varphi_1 + \psi_{3,1} \\ \gamma_{23}^{(0)} &= \psi_2 + w_{,2}, \quad \gamma_{23}^{(1)} = 2\varphi_2 + \psi_{3,2}\end{aligned}$$

However, the discrepancies between the actual displacement field and that of the approximate plate theory need to be corrected in order to improve the results obtained from the displacement assumptions of Eq. (4.5). Parameters κ_i are introduced in a manner similar to that in [47] for homogeneous isotropic plates, the following substitutions related to the thickness strains are made:

$$\begin{aligned}\kappa_3\varepsilon_{33}^{(0)} &\text{ for } \varepsilon_{33}^{(0)} \\ \kappa_1\gamma_{13}^{(0)} &\text{ for } \gamma_{13}^{(0)}, \quad \kappa_4\gamma_{13}^{(1)} \text{ for } \gamma_{13}^{(1)} \\ \kappa_2\gamma_{23}^{(0)} &\text{ for } \gamma_{23}^{(0)}, \quad \kappa_5\gamma_{23}^{(1)} \text{ for } \gamma_{23}^{(1)}\end{aligned}\tag{4.7}$$

where

$$\kappa_1 = \kappa_2 = \kappa_3 = \kappa = \pi/\sqrt{12}, \quad \kappa_4 = \kappa_5 = \pi/\sqrt{15}\tag{4.8}$$

These correction coefficients, κ_i , are obtained by matching the cut-off frequencies derived from the higher-order theory and 3-D elasticity theory as described in [46].

Substituting Eq. (4.6) into Eq. (4.4) and putting results into Eq. (4.1)~(4.3), the constitutive equations for isotropic plate can be yielded as:

$$\begin{Bmatrix} N_{11} \\ N_{22} \\ N_{12} \end{Bmatrix} = \begin{bmatrix} \lambda + 2G & \lambda & 0 \\ \lambda & \lambda + 2G & 0 \\ 0 & 0 & G \end{bmatrix} \left(h \begin{Bmatrix} u_{,1} \\ v_{,2} \\ u_{,2} + v_{,1} \end{Bmatrix} + \frac{h^3}{12} \begin{Bmatrix} \varphi_{1,1} \\ \varphi_{2,2} \\ \varphi_{1,2} + \varphi_{2,1} \end{Bmatrix} \right) + h\kappa\lambda \begin{Bmatrix} 1 \\ 1 \\ 0 \end{Bmatrix} \psi_3 \quad (4.9)$$

$$N_{33} = h[\kappa\lambda(u_{,1} + v_{,2}) + \kappa^2(\lambda + 2G)\psi_3] + \frac{h^3}{12}\kappa\lambda(\varphi_{1,1} + \varphi_{2,2}) \quad (4.10)$$

$$\begin{Bmatrix} R_2 \\ R_1 \end{Bmatrix} = \kappa^2 \frac{h^3}{12} G \begin{Bmatrix} 2\varphi_2 + \psi_{3,2} \\ 2\varphi_1 + \psi_{3,1} \end{Bmatrix} \quad (4.11)$$

$$\begin{Bmatrix} S_{11} \\ S_{22} \\ S_{12} \end{Bmatrix} = \begin{bmatrix} \lambda + 2G & \lambda & 0 \\ \lambda & \lambda + 2G & 0 \\ 0 & 0 & G \end{bmatrix} \left(\frac{h^3}{12} \begin{Bmatrix} u_{,1} \\ v_{,2} \\ u_{,2} + v_{,1} \end{Bmatrix} + \frac{h^5}{80} \begin{Bmatrix} \varphi_{1,1} \\ \varphi_{2,2} \\ \varphi_{1,2} + \varphi_{2,1} \end{Bmatrix} \right) + \kappa \frac{h^3}{12} \lambda \begin{Bmatrix} 1 \\ 1 \\ 0 \end{Bmatrix} \psi_3 \quad (4.12)$$

$$\begin{Bmatrix} M_{11} \\ M_{22} \\ M_{12} \end{Bmatrix} = \frac{h^3}{12} \begin{bmatrix} \lambda + 2G & \lambda & 0 \\ \lambda & \lambda + 2G & 0 \\ 0 & 0 & G \end{bmatrix} \begin{Bmatrix} \psi_{1,1} \\ \psi_{2,2} \\ \psi_{1,2} + \psi_{2,1} \end{Bmatrix} \quad (4.13)$$

$$\begin{Bmatrix} Q_2 \\ Q_1 \end{Bmatrix} = \kappa^2 h G \begin{Bmatrix} w_{,2} + \psi_2 \\ w_{,1} + \psi_1 \end{Bmatrix} \quad (4.14)$$

where λ and G are the Lamé's constants of elasticity, respectively.

With the linear strain-displacement relations, the equations of motion of the higher-order plate theory can be derived using the principle of virtual displacement or Hamilton's principle

$$0 = \int_{t_1}^{t_2} (\delta U + \delta V - \delta K) dt \quad (4.15)$$

where δU is the virtual strain energy, δV is the virtual work done by applied force, and δK is the virtual kinetic energy. A set of equations of motion is

$$\begin{aligned}
N_{11,1} + N_{12,2} + q_1 &= I_0 \ddot{u} + I_2 \ddot{\phi}_1 \\
N_{12,1} + N_{22,2} + q_2 &= I_0 \ddot{v} + I_2 \ddot{\phi}_2 \\
R_{1,1} + N_{2,2} - N_3 + m &= I_2 \ddot{\psi}_3 \\
S_{11,1} + S_{12,2} - R_1 + n_1 &= \frac{I_2}{2} \ddot{u} + \frac{I_4}{2} \ddot{\phi}_1 \\
S_{12,1} + S_{22,2} - R_2 + n_2 &= \frac{I_2}{2} \ddot{v} + \frac{I_4}{2} \ddot{\phi}_2
\end{aligned} \tag{4.16}$$

$$\begin{aligned}
Q_{1,1} + Q_{2,2} + q &= I_0 \ddot{w} \\
M_{11,1} + M_{12,2} - Q_1 + m_1 &= I_2 \ddot{\psi}_1 \\
M_{12,1} + M_{22,2} - Q_2 + m_2 &= I_2 \ddot{\psi}_2
\end{aligned} \tag{4.17}$$

where $(I_0, I_1, I_2, I_3, I_4) = \int_{-h/2}^{h/2} \rho(1, z, z^2, z^3, z^4) dz$, ρ is the mass density, and a number

of boundary conditions which must be specified on the plate edges:

$$\begin{aligned}
\begin{Bmatrix} q_\alpha \\ n_\alpha \end{Bmatrix} &= [\sigma_{\alpha 3}(h/2) - \sigma_{\alpha 3}(-h/2)] \begin{Bmatrix} 1 \\ h^2/4 \end{Bmatrix}, \quad m_\alpha = [\sigma_{\alpha 3}(h/2) + \sigma_{\alpha 3}(-h/2)] \frac{h}{2} \\
q &= \sigma_{33}(h/2) - \sigma_{33}(-h/2), \quad m = [\sigma_{33}(h/2) + \sigma_{33}(-h/2)] \frac{h}{2} \\
\alpha &= 1, 2
\end{aligned} \tag{4.18}$$

The equations of motion can be further expressed in terms of generalized displacements by substituting for the stress resultants from the constitutive equation (4.9)-(4.14). To make the variables dimensionless, the following non-dimensional variables and

quantities are defined by introducing a length scale $h/2$, a typical time scale $\tau = \frac{h}{2c_T}$:

$$\begin{aligned}
x'_i &= \frac{x_i}{h/2}, & t' &= \frac{t}{\tau}, & w' &= \frac{w}{h/2} \\
u' &= \frac{u}{h/2}, & v' &= \frac{v}{h/2}, & \phi'_\alpha &= \phi_\alpha h/2 \\
q'_\alpha &= \frac{q_\alpha}{2G}, & n'_\alpha &= \frac{n_\alpha}{Gh^2/20}, & m' &= \frac{m}{Gh/3} \\
q' &= \frac{q}{2G}, & m'_\alpha &= \frac{m_\alpha}{Gh/3} \\
k'_\alpha &= k_\alpha h/2, & \omega' &= \omega\tau
\end{aligned} \tag{4.19}$$

where k'_α , ω' are the non-dimensional wave number and frequency and $c_T = \sqrt{G/\rho}$ is the velocity of bulk transverse or shear vertical wave. Note that the non-dimensional quantities will be used in the following wave analysis and all the primes will be dropped except stated.

The dimensionless equations of motion can be expressed as:

$$\alpha u_{,11} + (\alpha - 1)v_{,12} + u_{,22} + [\alpha\phi_{1,11} + (\alpha - 1)\phi_{2,12} + \phi_{1,22}]/3 + \kappa(\alpha - 2)\psi_{3,1} + q_1 = \ddot{u} + \ddot{\phi}_1/3 \tag{4.20}$$

$$v_{,11} + (\alpha - 1)u_{,12} + \alpha v_{,22} + [\phi_{2,11} + (\alpha - 1)\phi_{1,12} + \alpha\phi_{2,22}]/3 + \kappa(\alpha - 2)\psi_{3,2} + q_2 = \ddot{v} + \ddot{\phi}_2/3 \tag{4.21}$$

$$\kappa_4^2(\psi_{3,11} + \psi_{3,22}) - [\kappa(\alpha - 2) - 2\kappa_4^2](\phi_{1,11} + \phi_{2,22}) - 3\kappa(\alpha - 2)(u_{,11} + v_{,22}) - 3\kappa^2\alpha\psi_3 + m = \ddot{\psi}_3 \tag{4.22}$$

$$\{\alpha u_{,11} + (\alpha - 1)v_{,12} + u_{,22} + [\kappa(\alpha - 2) - 2\kappa_4^2]\psi_{3,1} - 4\kappa_4^2\phi_1\}/3 + \alpha\phi_{1,11} + (\alpha - 1)\phi_{2,12} + \phi_{1,22} + n_1 = \frac{5}{3}\ddot{u} + \ddot{\phi}_1 \tag{4.23}$$

$$\{v_{,11} + (\alpha - 1)u_{,12} + \alpha v_{,22} + [\kappa(\alpha - 2) - 2\kappa_4^2]\psi_{3,2} - 4\kappa_4^2\phi_2\}/3 + \phi_{2,11} + (\alpha - 1)\phi_{1,12} + \alpha\phi_{2,22} + n_2 = \frac{5}{3}\ddot{v} + \ddot{\phi}_2 \tag{4.24}$$

and

$$\kappa^2(w_{,11} + w_{,22} + \psi_{1,1} + \psi_{2,2}) + q = \ddot{w} \tag{4.25}$$

$$\alpha\psi_{1,11} + (\alpha - 1)\psi_{2,12} + \psi_{1,22} - 3\kappa^2(w_{,11} + \psi_1) + m_1 = \ddot{\psi}_1 \tag{4.26}$$

$$\psi_{2,11} + (\alpha - 1)\psi_{1,12} + \alpha\psi_{2,22} - 3\kappa^2(w_{,22} + \psi_2) + m_2 = \ddot{\psi}_2 \tag{4.27}$$

where $\alpha = 2 + \lambda/G = 2(1 - \nu)/(1 - 2\nu)$ and ν is Poisson's ratio.

The non-dimensionalization shows its advantage in further discussion as the

equations only depend on a single parameter α or Poisson's ratio. Also, the equations (4.20)-(4.27) indicate that the extensional (or symmetric) waves with five degrees of freedom ($u, v, \psi_3, \varphi_1, \varphi_2$) are decoupled from the flexural (or anti-symmetric) waves with three degrees of freedom (w, ψ_1, ψ_2). The symmetric and anti-symmetric waves refer to the wave displacement profile symmetric and anti-symmetric with respect to the mid-plane of the plate, $z = 0$, respectively. By setting all mechanical loads to zero and seeking the plane wave elementary solutions

$$\mathbf{U} = \mathbf{a} \exp[i(\mathbf{k} \cdot \mathbf{x} - \omega t)] \quad (4.28)$$

where \mathbf{U} is the displacement vector, $\mathbf{k} = [k_1, k_2]^T$ is the wave vector, ω is the angular frequency, and \mathbf{a} is the complex-valued vector (or wave amplitude), the dispersion relations for extensional waves and flexural waves can be obtained separately as follows.

4.1.2 Dispersion relation for extensional wave

For extensional wave, the displacement vector takes the form of $\mathbf{U} = [u, v, \psi_3, \varphi_1, \varphi_2]^T$. Substituting Eq. (4.28) into Eq. (4.20)-(4.24), the following generalized eigenvalue problem is formed:

$$(\mathbf{K} - \omega^2 \mathbf{M})\mathbf{a} = \mathbf{0} \quad (4.29)$$

where

$$\mathbf{K} = \begin{bmatrix} \alpha k_1^2 + k_2^2 & (\alpha - 1)k_1 k_2 & -i\kappa(\alpha - 2)k_1 & (\alpha k_1^2 + k_2^2)/3 & (\alpha - 1)k_1 k_2 / 3 \\ (\alpha - 1)k_1 k_2 & k_1^2 + \alpha k_2^2 & -i\kappa(\alpha - 2)k_2 & (\alpha - 1)k_1 k_2 / 3 & (k_1^2 + \alpha k_2^2)/3 \\ 3i\kappa(\alpha - 2)k_1 & 3i\kappa(\alpha - 2)k_2 & \kappa_4^2(k_1^2 + k_2^2) + 3\alpha\kappa^2 & i[\kappa(\alpha - 2) - 2\kappa_4^2]k_1 & i[\kappa(\alpha - 2) - 2\kappa_4^2]k_2 \\ \frac{5}{3}(\alpha k_1^2 + k_2^2) & \frac{5}{3}(\alpha - 1)k_1 k_2 & -\frac{5}{3}i[\kappa(\alpha - 2) - 2\kappa_4^2]k_1 & \alpha k_1^2 + k_2^2 + \frac{20}{3}\kappa_4^2 & (\alpha - 1)k_1 k_2 \\ \frac{5}{3}(\alpha - 1)k_1 k_2 & \frac{5}{3}(k_1^2 + \alpha k_2^2) & -\frac{5}{3}i[\kappa(\alpha - 2) - 2\kappa_4^2]k_2 & (\alpha - 1)k_1 k_2 & k_1^2 + \alpha k_2^2 + \frac{20}{3}\kappa_4^2 \end{bmatrix}$$

$$\mathbf{M} = \begin{bmatrix} 1 & 0 & 0 & 1/3 & 0 \\ 0 & 1 & 0 & 0 & 1/3 \\ 0 & 0 & 1 & 0 & 0 \\ 5/3 & 0 & 0 & 1 & 0 \\ 0 & 5/3 & 0 & 0 & 1 \end{bmatrix}$$

Nontrivial solutions of Eq. (4.29) have to be related by setting the determinant of the coefficient matrix to zero; that is,

$$|\mathbf{K} - \omega^2 \mathbf{M}| = 0 \quad (4.30)$$

where \mathbf{k} is the wave vector with magnitude of $k = |\mathbf{k}|$ and wave propagation direction of ϕ .

Accordingly, $k_1 = k \cos \phi$, $k_2 = k \sin \phi$ and ω is a function of both the wave number k and the propagation direction $\omega = W(\mathbf{k}) = W(k, \phi)$. However, for isotropic plates, ω is independent of ϕ . Eq. (4.30) can be expanded to the following terms

$$\omega^2 = k^2 \quad (4.31)$$

$$\omega^2 = k^2 + \pi^2 \quad (4.32)$$

$$\begin{vmatrix} \alpha k^2 - \omega^2 & (\alpha k^2 - \omega^2)/3 & -i\kappa(\alpha - 2)k \\ \frac{5}{3}(\alpha k^2 - \omega^2) & \alpha k^2 + \frac{20}{3}\kappa_4^2 - \omega^2 & -\frac{5}{3}i[\kappa(\alpha - 2) - 2\kappa_4^2]k \\ 3i\kappa(\alpha - 2)k & i[\kappa(\alpha - 2) - 2\kappa_4^2]k & \kappa_4^2 k^2 + 3\alpha\kappa^2 - \omega^2 \end{vmatrix} = 0 \quad (4.33)$$

Or Eq. (4.33) can be written in the polynomial form as

$$\omega^6 + \alpha_1 \omega^4 + \alpha_2 \omega^2 + \alpha_3 = 0 \quad (4.34)$$

$$\begin{aligned} \alpha_1 &= -(2\alpha + \kappa_4^2)k^2 - 3(\alpha\kappa^2 + 5\kappa_4^2) \\ \alpha_2 &= \alpha(\alpha + 2\kappa_4^2)k^4 + 3[(\alpha^2 + 4\alpha - 4)\kappa^2 + 5\alpha\kappa_4^2]k^2 + 45\alpha\kappa^2\kappa_4^2 \\ \alpha_3 &= -[\alpha^2\kappa_4^2k^4 + 12\kappa^2(\alpha - 1)(\alpha k^2 + 15\kappa_4^2)]k^2 \end{aligned} \quad (4.35)$$

where

Total five pairs of wave modes are obtained. For Eq. (4.31) and (4.32), the corresponding wave displacements do not have the transverse component u_3 and are

perpendicular to the wave propagation direction. Because the displacements for the modes are symmetric with respect to $z = 0$, they may be called symmetric shear horizontal (SH) waves. The group velocity which takes the form of $d\omega/dk$ can be immediately obtained. For Eq. (4.34), a closed-form expression for ω^2 can be obtained by solving the cubic equation.

$$\omega^2 = \frac{p}{3u} - u - \frac{a_1}{3} \quad (4.36)$$

where $p = \alpha_2 - \frac{\alpha_1^3}{3}$, $q = \alpha_3 + \frac{2\alpha_1^3 - 9\alpha_1\alpha_2}{27}$ and $u = \sqrt[3]{\frac{q}{2} \pm \sqrt{\frac{q^2}{4} + \frac{p^3}{27}}}$. However, it is convenient to obtain group velocity by taking partial derivative of Eq. (4.34) with respect to k , which yields

$$c_g = \frac{d\omega}{dk} = -\frac{\alpha'_1\omega^4 + \alpha'_2\omega^2 + \alpha'_3}{6\omega^5 + 4\alpha_1\omega^3 + 2\alpha_2\omega} \quad (4.37)$$

where the prime ‘’ denotes partial derivative of k . Figure 4.3 plots the relationship of ω versus k as Poisson’s ratio ν is set to 0.33, and Figure 4.2 depicts the corresponding phase velocity ω/k with respect to non-dimensional angular frequency.

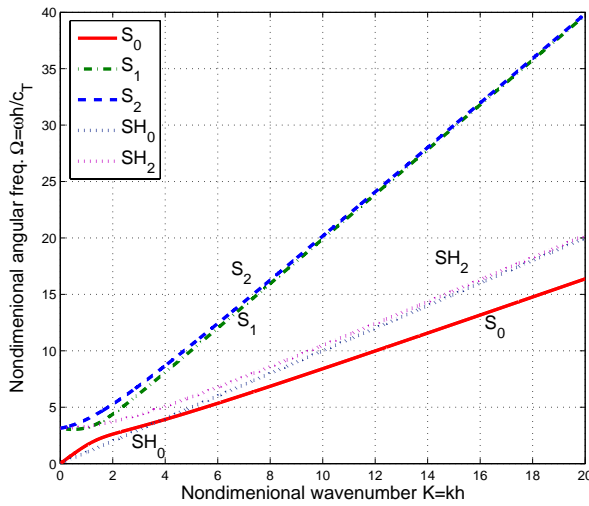


Figure 4.3 Dimensionless dispersion relation for extensional wave ($\nu = 0.33$)

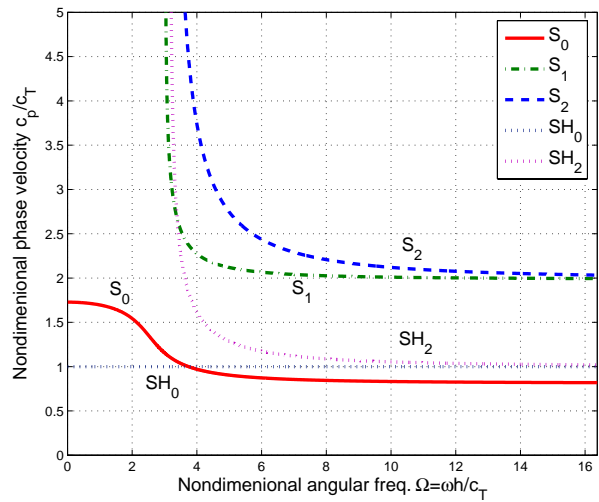


Figure 4.2 Dimensionless phase velocity for extensional wave ($\nu = 0.33$)

4.1.3 Dispersion relation for flexural wave

For flexural wave, the displacement vector takes the form of $\mathbf{U} = [w, \psi_1, \psi_2]^T$.

Substituting Eq. (4.28) into Eq. (4.25)-(4.27) yields a standard eigenvalue problem

$$(\mathbf{A} - \omega^2 \mathbf{I})\mathbf{a} = \mathbf{0} \quad (4.38)$$

where

$$\mathbf{A} = \begin{bmatrix} \kappa^2 k^2 & -i\kappa^2 k_1 & -i\kappa^2 k_2 \\ 3i\kappa^2 k_1 & \alpha k_1^2 + k_2^2 + 3\kappa^2 & (\alpha - 1)k_1 k_2 \\ 3i\kappa^2 k_2 & (\alpha - 1)k_1 k_2 & k_1^2 + \alpha k_2^2 + 3\kappa^2 \end{bmatrix}$$

Similar to the case of extensional wave, nontrivial solutions of Eq. (4.38) can be given by setting the determinant of the coefficient matrix to zero; that is,

$$|\mathbf{A} - \omega^2 \mathbf{I}| = 0 \quad (4.39)$$

and can be further decomposed to into two equations as

$$\omega^2 - k^2 - \pi^2 / 4 = 0 \quad (4.40)$$

$$\omega^4 - [(\alpha + \kappa^2)k^2 + 3\kappa^2]\omega^2 + \alpha\kappa^2 k^4 = 0 \quad (4.41)$$

There exist three pairs of wave modes. For Eq. (4.40), the corresponding wave displacements do not have the transverse component u_3 , and it represents for anti-symmetric SH wave. For Eq. (4.41), a closed-form expression for ω^2 can be given by

$$\omega^2 = \frac{(\alpha + \kappa^2)k^2 + 3\kappa^2}{2} \pm \sqrt{\left[\frac{(\alpha - \kappa^2)k^2 + 3\kappa^2}{2}\right]^2 + 3\kappa^4 k^2} \quad (4.42)$$

and group velocity can be immediately derived due to the explicit form. Figure 4.4 plots the relationship of ω versus k as Poisson's ratio ν is set to 0.33, and Figure 4.5 depicts the corresponding phase velocity ω/k with respect to non-dimensional angular frequency.

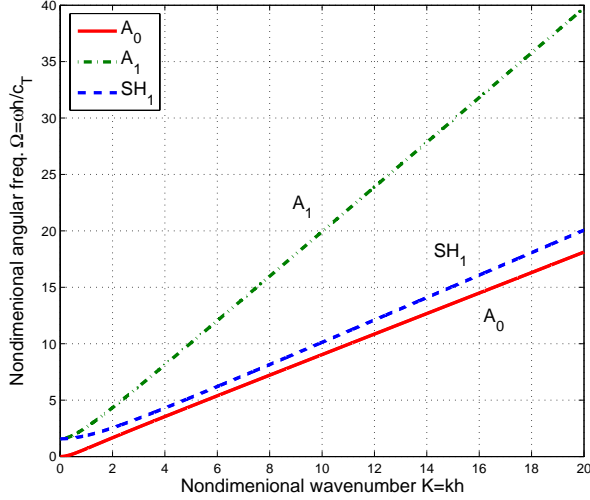


Figure 4.4 Dimensionless dispersion relation for flexural wave ($\nu = 0.33$)

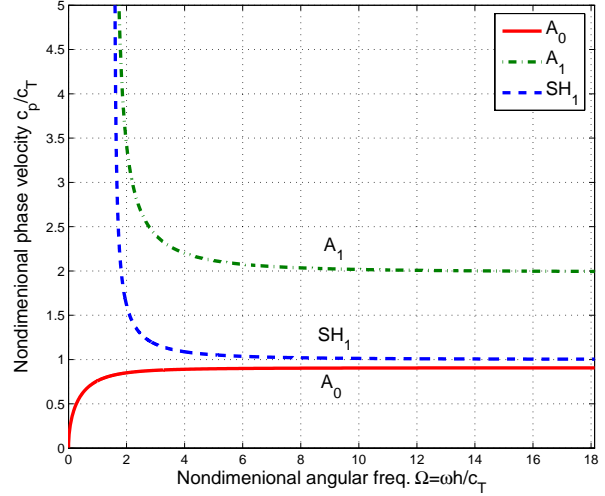


Figure 4.5 Dimensionless phase velocity for flexural wave ($\nu = 0.33$)

4.2 Transient Wave Propagation in Dispersive Mediums

In SHM, transient stress waves are usually excited from actuators and used for active diagnosis. Through Fourier or wavelet analysis, the transient wave can be decomposed in terms of a number of steady harmonic waves with a spectrum of frequencies. As the different frequency components propagate with different phase velocity, the transient waves will spread or be *dispersive* in both space and time. This section will describe the dispersion effect of transient wave propagating in 1-D dispersive mediums using Fourier analysis.

Suppose a narrowband incident wave is excited at the origin, $x = 0$, with a form of

$$f(t) = m(t)e^{i\omega_0 t} \quad (4.43)$$

where $m(t)$ is a slowly varying modulation function which has small bandwidth in frequency domain, and ω_0 is the central frequency. Due to the modulation, both the envelope of $f(t)$ in time domain and its frequency spectrum will be affected by $m(t)$. A Fourier transform pair can be established to express the relationship of the incident transient wave and its frequency spectrum

$$f(t) = \frac{1}{2\pi} \int_{-\infty}^{\infty} F(\omega) e^{i\omega t} d\omega \quad (4.44)$$

$$F(\omega) = \int_{-\infty}^{\infty} f(t) e^{-i\omega t} dt \quad (4.45)$$

As a wave propagates to the position x , each frequency component of the wave will arrive at x with time delay as $\frac{x}{c_p} = \frac{kx}{\omega}$. By replacing t by $t - \frac{kx}{\omega}$ in Eq (4.44), an expression

for a 1-D wave of arbitrary waveform traveling in the positive direction can be obtained

$$f(x, t) = \frac{1}{2\pi} \int_{-\infty}^{\infty} F(\omega) e^{i(\omega t - kx)} d\omega \quad (4.46)$$

where $k = K(\omega)$. For a positive-going wave, ω must have the same sign as k . The equation implies that the wave $f(x, t)$ can be expressed by the superposition of a continuous spectrum of waves $e^{i(\omega t - kx)}$ of complex amplitude $\frac{1}{2\pi} F(\omega) d\omega$. The FT ($F(\omega)$), which can be found from the wave at $x=0$ using Eq. (4.45), expresses the density of the complex amplitude spectrum as a function of frequency. Substituting Eq. (4.43) into Eq. (4.45) and (4.46) gives

$$f(x, t) = \frac{1}{2\pi} \int_{-\infty}^{\infty} M(\omega - \omega_0) e^{i(\omega t - kx)} d\omega \quad (4.47)$$

where $M(\omega) = \int_{-\infty}^{\infty} m(t) e^{-i\omega t} dt$.

For the description of the propagation of a narrowband wave, $f(0, t)$, the dispersion relation, $k = K(\omega)$, can be expanded in a Taylor series around the central frequency ω_0 as

$$k = K(\omega) = k_0 + k_1(\omega - \omega_0) + k_2(\omega - \omega_0)^2 + \dots \quad (4.48)$$

where $k_0 = \frac{\omega_0}{c_p}$, $k_1 = \left. \frac{dk}{d\omega} \right|_{\omega=\omega_0}$, $k_2 = \left. \frac{1}{2} \frac{d^2k}{d\omega^2} \right|_{\omega=\omega_0}$.

If $K(\omega)$ is a linear function of ω , only the first two terms of the expansion are non-zero. Substituting Eq. (4.48) into Eq. (4.47) yields

$$f(x, t) = \frac{1}{2\pi} e^{-ik_0 x} \int_{-\infty}^{\infty} M(\omega - \omega_0) e^{-ik_1 x(\omega - \omega_0)} e^{i\omega t} d\omega \quad (4.49)$$

and can be further simplified by using the translation and shifting properties of the FT

$$f(x, t) = m(t - k_1 x) e^{i(\omega_0 t - k_0 x)} \quad (4.50)$$

Physically, Eq. (4.50) means that the phase of the central frequency component is shifted by $k_0 x$ with the phase velocity $\omega_0/k_0 = c_p$, and the modulation envelope retains the original shape and travels with the velocity of $1/k_1 = \frac{d\omega}{dk}$, which is referred as *group velocity* and will be denoted as c_g hereafter. The derivation also implies that, if k_2 and higher-order coefficients in Eq. (4.48) can be neglected, the wave propagates with a constant envelope shape, or without dispersion.

Figure 4.6 and Figure 4.7 give the group velocities of extensional and flexural waves in isotropic plates ($\nu = 0.33$) obtained from Section 4.1.2 and Section 4.1.3 based on the higher-order plate theory. For extensional waves, three extensional wave modes and two shear-horizontal (SH) wave modes are shown in the figure. One of the extensional modes, S_0 , has no cutoff frequency, and the other two modes, S_1 and S_2 , have cut-off frequencies at $\sqrt{3\alpha\kappa}$ and $\sqrt{15\kappa_4}$ respectively. Similarly, for flexural waves excluding the anti-symmetric SH_1 mode, only one mode, A_1 , has a dimensionless cutoff frequency at $\pi/2$. The numerical solution from 3-D elasticity theory is also obtained and plotted in Figure 4.8 (the SH wave modes have been omitted). Although there are infinite modes based on 3-D theory, only the first five of each symmetric and anti-symmetric mode are displayed respectively. In

comparison with 3-D elasticity theory, the higher-order theory that gives very close results. However, closed-form solutions by solving polynomials can be provided by the higher-order theory as opposed to solving transcendental equations based on 3-D theory. It can be seen from the figures that group velocities for all wave modes have complex shapes with respect to frequency or wave number.

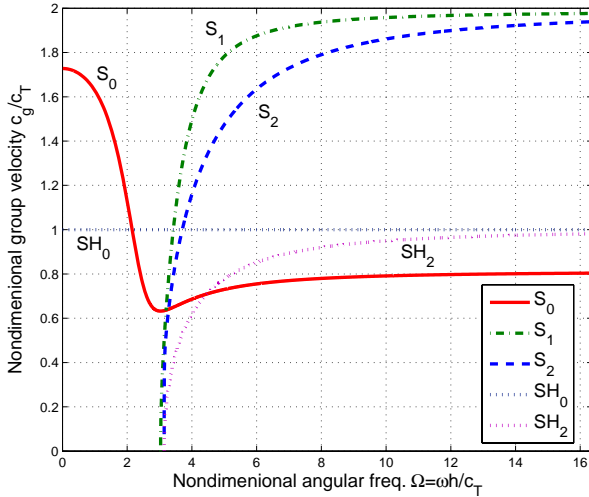


Figure 4.6 Dimensionless group velocity for extensional wave from higher-order plate theory ($\nu = 0.33$)

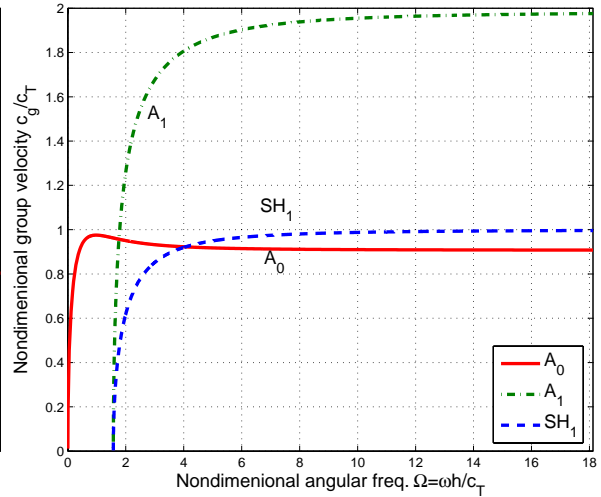


Figure 4.7 Dimensionless group velocity for flexural wave from higher-order plate theory ($\nu = 0.33$)

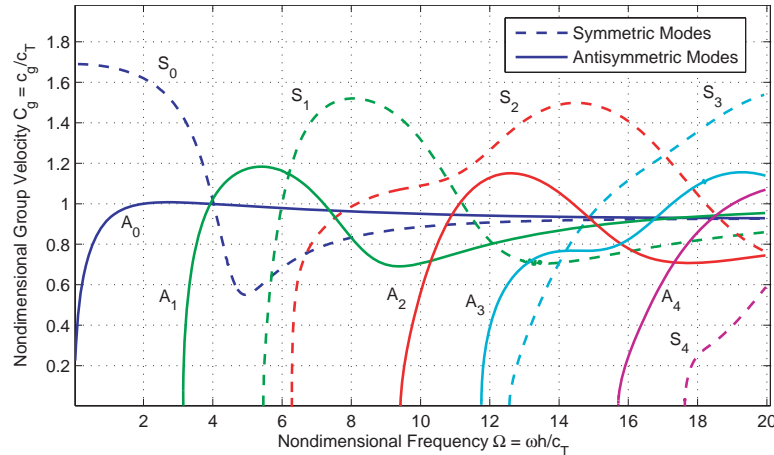


Figure 4.8 Dimensionless group velocity calculated from 3-D elastic theory ($\nu = 0.33$)

To encompass the complex shapes of group velocities, the Taylor expansion (4.48) is truncated after the third term to obtain the second-order approximation solution (the error of

truncation is $o(\omega - \omega_0)^3$ and the expression is exact when $K(\omega)$ is a quadratic function of ω). Substituting the expansion into Eq. (4.47) and rearranging the exponential terms leads to

$$f(x, t) = \frac{1}{2\pi} e^{-ik_0 x} \int_{-\infty}^{\infty} \left(M(\omega - \omega_0) e^{-ik_1 x(\omega - \omega_0)} \right) \left(e^{-ik_2 x(\omega - \omega_0)^2} \right) e^{i\omega t} d\omega \quad (4.51)$$

Eq. (4.51) can be interpreted as the inverse FT of the product of two FTs which are identified by the brackets of the integrand in the integral. The former is $m(t - k_1 x)$ and the latter is

$$q(t) = \sqrt{\alpha/\pi} e^{-\alpha t^2} \quad (4.52)$$

where $\alpha = (4ik_2 x)^{-1}$. Using the convolution theorem, Eq (4.51) can be further simplified as

$$f(x, t) = [m(t - k_1 x) \otimes q(t)] e^{i(\omega_0 t - k_0 x)} \quad (4.53)$$

where \otimes denotes convolution. Due to the convolution, specifically with a Gaussian function $q(t)$, distortion and spread of the modulation envelope will be observed in time domain along with the phase shift of the central frequency component. Comparing Eq. (4.53) with Eq. (4.50), the dispersion is presented by convoluting the modulation function with the Gaussian function $q(t)$ related to the second-order term.

For example, a Gaussian wave packet, which is a typical narrowband transient wave, may be expressed by

$$f(0, t) = A e^{-\left(t/2\sigma_0\right)^2} e^{i\omega_0 t} \quad (4.54)$$

where A stands for the initial amplitude and σ_0 depicts the root-mean-square time spread.

The dispersed Gaussian wave packet with propagation distance of x can be derived as

$$f(x, t) = \frac{A\sigma_0}{\sigma} e^{-\left[(t - k_1 x)/2\sigma\right]^2} e^{i(\omega_0 t - k_0 x)} \quad (4.55)$$

where $\sigma^2 = \sigma_0^2 + ik_2 x$ is defined as a complex time spread of the wave packet. The second-

order term contributes to the propagation of the waves in two aspects: (1) the time spread of

the wave packet, $|\sigma| = \sigma_0 \sqrt{1 + \frac{k_2^2 x^2}{\sigma_0^4}}$, increases with the propagation distance x ; and (2) the

amplitude of the wave packet simultaneously decreases with x , in such a manner that the area

under $|f(x, t)|^2$ is constant.

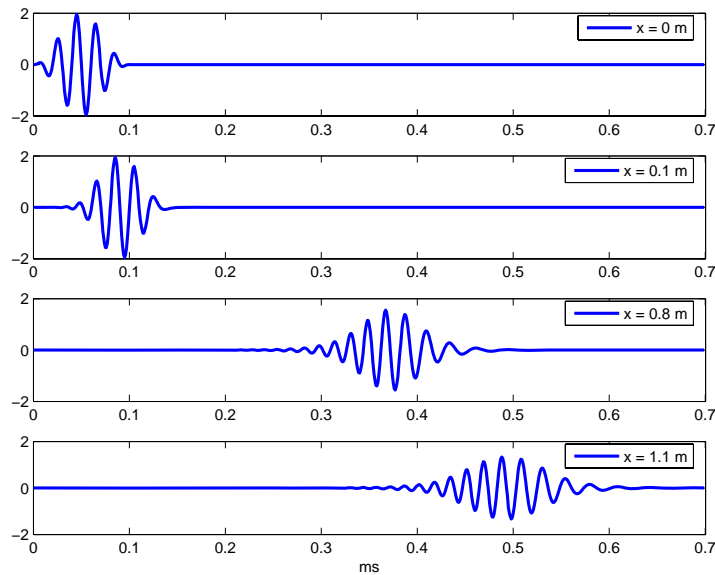


Figure 4.9 Dispersion of transient wave propagating in aluminum plate

Figure 4.9 gives an illustration for 1-D transient wave propagation of a five-peaked wave, which is described in Appendix C and will be used as excitation throughout this research. Material properties of aluminum Al6061, listed in Table 4.1, were used to derive the dispersion relations. Waveforms with three different propagation distances are calculated using Eq. (4.46). The dispersion is evidently shown as the wave is spread out and distorted with decreased amplitude of the envelope.

Table 4.1 Material properties and geometry of an Al 6061 plate

E (GPa)	ν	ρ (kg/m ³)	h (mm)	Dimension (m×m)
72	0.3	2730	3.175	0.91×0.91

4.3 Dispersion Removal

Due to the increase in duration, several dispersed waves have higher chance of overlapping. It is relatively hard to resolve separate waves from different arrivals, and consequently the resolution may be decreased when diagnostic waves are used to detect damages. In addition, the dispersive nature can make the interpretation of the recorded signal less straightforward. For example, some techniques including the cross-correlation method which will be introduced and used later in this work may not be used. For these reasons, the excitation of diagnostic waves for active diagnosis system is mostly restricted to a non-dispersive region (horizontal) on the group velocity curve.

Different techniques have been proposed to remove dispersion. Some methods are dependent on the propagation distance [48] and experimental setup [49]. Such restrictions make them less practical. Several authors have proposed and developed a “spectral warping” method, i.e., a nonlinear rescaling of the frequency axis, to remove dispersion from a signal in time-space domain using frequency transformation to interpret the seismic signal [50-53]. The rescaling is defined mathematically by a composition of the spectrum of the trace with a function closely related to the dispersion relation [52]. The advantage of this method is that it is independent of propagation distances and can be applied to signals consisting of multiple arrivals with the same dispersion relation. Since the dispersion relation is usually unknown in geophysical field, the polynomial form for the dispersion relation must be iteratively changed and tried to find an optimal point by checking the arrival envelope widths [53]. Robinson *et al.* [54] also proposed time-variable inverse filters to de-convolve signals with dispersion due to absorption. Both methods are essentially analogous to a 1-D, frequency-domain migration which accounts for dispersion [52]. Lately, Li [55] reviewed the spectral warping method and

derived a method of signal compression by using scaling properties in the FT. More recently, Wilcox [56] presented a numerical procedure to obtain the dispersion compensated distance-trace by mapping the frequency domain data to the wave number domain using the known dispersion relation.

From the viewpoint of SHM systems, the compression in time domain, or the elimination of dispersion in time domain, can be more convenient and enable easier interpretation. In this section, an algorithm, called *linear mapping*, is developed to remove wave dispersion in time-domain directly by using the known dispersion relation.

4.3.1 Linear mapping algorithm

In Section 4.2, geometrical spreading, attenuation (k is real) and the reflection (scattering) dependence of any form have been neglected to formulate the 1-D wave propagation. Assuming that the mode conversion of the reflections is of insignificant magnitude, Eq. (4.46) is modified to be in the form of

$$f(x, t) = \frac{1}{2\pi} \int_{-\infty}^{\infty} A(\omega) F(\omega) e^{i(\omega t - kx)} d\omega \quad (4.56)$$

where $A(\omega)$ presents attenuation and/or reflection coefficient. When transient waves are used to detect damage in a plate, the signal received by a sensor can be written as a superposition of multiple waves in time domain,

$$g(t) = \sum_{n=1}^N f_n(r_n, t) = \frac{1}{2\pi} \int_{-\infty}^{\infty} F(\omega) \sum_{n=1}^N \left(A_n(\omega) e^{-ikr_n} \right) e^{i\omega t} d\omega \quad (4.57)$$

where N is the total number of propagating wave paths and r_n is the n^{th} wave path. The frequency spectrum $G(\omega)$ can be obtained from Eq. (4.44)

$$G(\omega) = F(\omega) \sum_{n=1}^N \left(A_n(\omega) e^{-ikr_n} \right) \quad (4.58)$$

which depicts the frequency components superposed from N numbers of propagating wave packets. As discussed in previous section, the dispersion depends on the dispersion relation, $k = K(\omega)$. If $k = K(\omega)$ is a quadratic or higher-order function of ω around ω_0 , $G(\omega)$ represents the frequency spectrum of dispersed wave packets; If $K(\omega)$ is a linear function of ω , $G(\omega)$ is the frequency spectrum of non-dispersed wave packets. For isotropic thin plate, the dispersion relation can be derived from the higher-order plate theory in Eq.(4.31)-(4.34) or Eq. (4.40)-(4.41).

If $k = K(\omega)$ in Eq. (4.58) can be replaced by the first-order Taylor expansion, the dispersion can be removed. The wave signal in time-domain will be seen as recompressed to a non-dispersive form, and the group velocity, or the time of arrival in the sense of diagnostic information, will be kept the same.

For a particular case where N can be reduced to one and propagation distance is known (which represents direct propagation from an actuator to a sensor), dispersion removal can be made by eliminating the quadratic term in the Taylor expansion of $K(\omega)$ since the contribution of the higher terms is minor. Mathematically, it can be expressed as

$$\mathfrak{G}(\omega) = \left(F(\omega) A_n(\omega) e^{-ikr_1} \right) e^{ik_2(\omega-\omega_0)^2 r_1} \quad (4.59)$$

where $\mathfrak{G}(\omega)$ is the frequency spectrum after dispersion removal and r_1 is the distance between the actuator and the sensor. The recompressed waveform in time domain can be immediately deduced by applying inverse Fourier transform of $\mathfrak{G}(\omega)$. However, since the propagation distance is usually unknown and N may be larger than one due to reflection from boundaries and damages, such dispersion removal is not practically useful.

To allow dispersion removal for general cases, the dispersion relation is firstly examined. Figure 4.10 interprets the dispersion relation (A_0 mode) and its Taylor expansions of first-order and second-order for an aluminum plate with 1/8 in. thickness. The solid line shows $K(\omega)$ derived from the higher-order plate theory for an aluminum plate with thickness of 1/8 in., while the dash-dot line indicates the first-order Taylor expansion and the dash line represents the second-order Taylor expansion. The thin dash line marks the central angular frequency ($\omega_0 = 2\pi \cdot 50kHz$). It can be noticed that the second-order Taylor expansion still has minor deviation from the theoretical relationship due to the contribution of higher-order terms. Thus, the dispersion would be more severe than that modeled in the previous section.

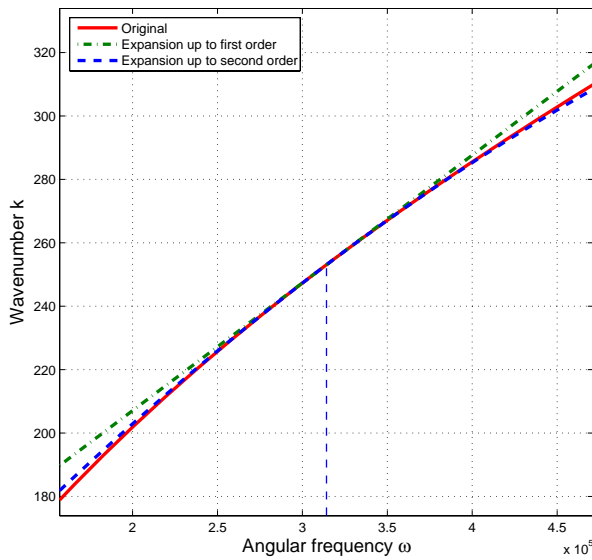


Figure 4.10 The dispersion relation and its Taylor expansions for 1/8 in. plate

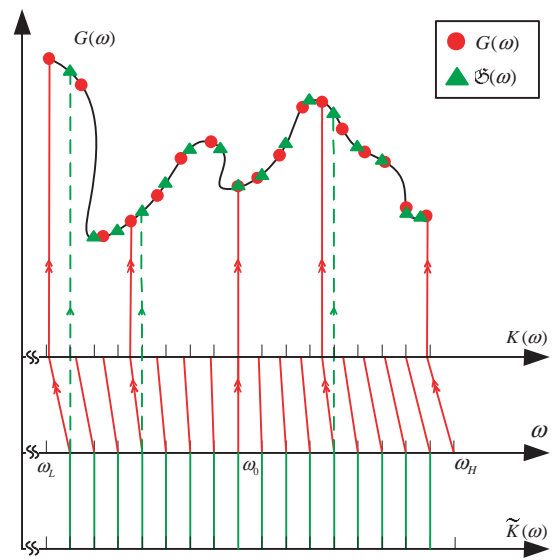


Figure 4.11 Illustration of the linear mapping for dispersion removal

Also, it can be seen from the figure that $K(\omega)$ is a monotonic function of ω in the region around ω_0 for the given case. This implies that ω can be also a function of k in a corresponding region. Eq. (4.58) can be written in a composite function of $K(\omega)$

$$G(\omega) = \tilde{G}(k) \circ K(\omega) \quad (4.60)$$

where \circ is composition operator, and $\tilde{G}(k)$ is an implicit function of k from Eq. (4.58). By changing $K(\omega)$ to its first-order Taylor expansion, a modified frequency spectrum $\mathfrak{G}(\omega)$ can be obtained since $\tilde{G}(k)$ is known. The modified frequency spectrum, then, can be readily used to obtain a recompressed signal in time domain. In other words, $K(\omega)$ is mapped into a linear function $\tilde{K}(\omega)$ to use the frequency spectrum to obtain a new frequency spectrum $\mathfrak{G}(\omega)$. This procedure of dispersion removal is referred as *linear mapping*. Practically, since narrowband waves are used and the mapping is made within a narrow frequency band around ω_0 , the statement, $K(\omega)$ is monotonic, can be usually satisfied.

Figure 4.11 explains the linear mapping graphically. By applying discrete fast Fourier transform (DFFT) on a collected signal, the frequency spectrum $G(\omega)$ can be easily obtained as a sequence of complex numbers. Due to the difficulty of presenting complex numbers in a 2D plot, $G(\omega)$ is illustrated by a curve with three horizontal axes in the figure. The red lines between the top axis and the middle axis, noted with $K(\omega)$ and ω respectively, indicate the function composition described in Eq. (4.60). The frequency spectrum can be seen to be obtained by firstly mapping a sequence of equally spaced values of ω into a sequence of $k = K(\omega)$ and then mapping the sequence of k into another sequence of $G(\omega) = \tilde{G}(k)$ which is marked as red dots in the figure. It must be noted that the red dots are not evenly distributed with respect to ω . To remove dispersion, the dispersion relation $K(\omega)$ may be replaced with its first-order Taylor expansion. The green lines between the middle axis and the bottom axis, which is $\tilde{k} = \tilde{K}(\omega)$, depicts the replacement in the figure. Since $\tilde{K}(\omega)$ is a linear function, all these green lines are in parallel vertically. Noticing that the new frequency

spectrum $\mathfrak{G}(\omega)$ may be still obtained by using $\mathfrak{G}(\omega) = \tilde{G}(k)$, interpolation can be made on $\tilde{G}(k)$ to find values corresponding to $\tilde{k} = \tilde{K}(\omega)$.

After the linear mapping, recompressed signal in time domain can be reconstructed by using inverse FT. Comparing with Eq. (4.59), the linear mapping does not require information on propagation distance and is able to handle reflections. $K(\omega)$ can be in arbitrary shape as long as it is monotonic in a region around ω_0 . The higher-order terms in the Taylor series expansion is not of importance as their influence can be eliminated through the interpolation.

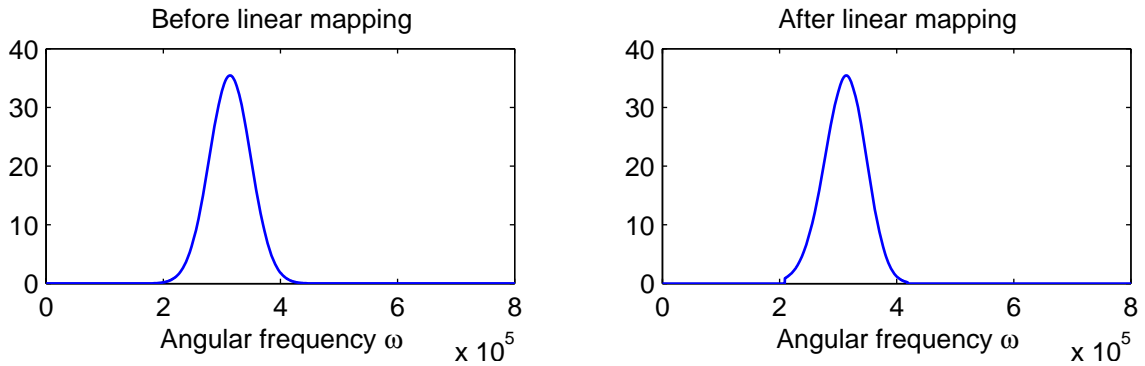


Figure 4.12 Comparison of amplitude spectrum before and after linear mapping

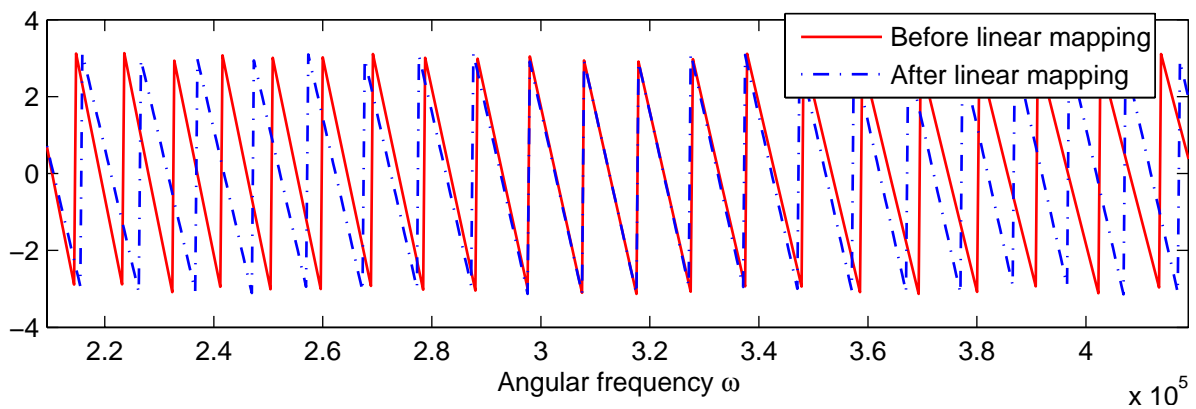


Figure 4.13 Comparison of phase spectrum before and after linear mapping

To depict the dispersion removal by the linear mapping, A Gaussian wave packet with central frequency of 50 kHz was modeled to propagate with the dispersion relation

shown in Figure 4.10. Figure 4.12 compares the amplitude spectrum before and after the linear mapping. As expected, the amplitude spectrum after the linear mapping is almost unchanged since the mapping from $K(\omega)$ to $\tilde{K}(\omega)$ only corrects the phases, which are compared in Figure 4.13. It can be seen from Figure 4.13 that: (1) two phase spectrums are almost identical in the region around ω_0 ; (2) the phase after the linear mapping oscillates more rapidly than the phase before the linear mapping in the region far beyond ω_0 ; (3) the phase after the linear mapping oscillates slowly in the region far below ω_0 . This is a good agreement with that shown Figure 4.10 by examining the change of slope of the dispersion relation. Figure 4.14 depicts the same phase spectrum comparison except the phases are unwrapped to remove the discontinuity at the multiples of 2π . It clearly shows that the phase of $G(\omega)$ given by Eq. (4.58) is stretched from a semi-quadratic curve into an approximately straight line.

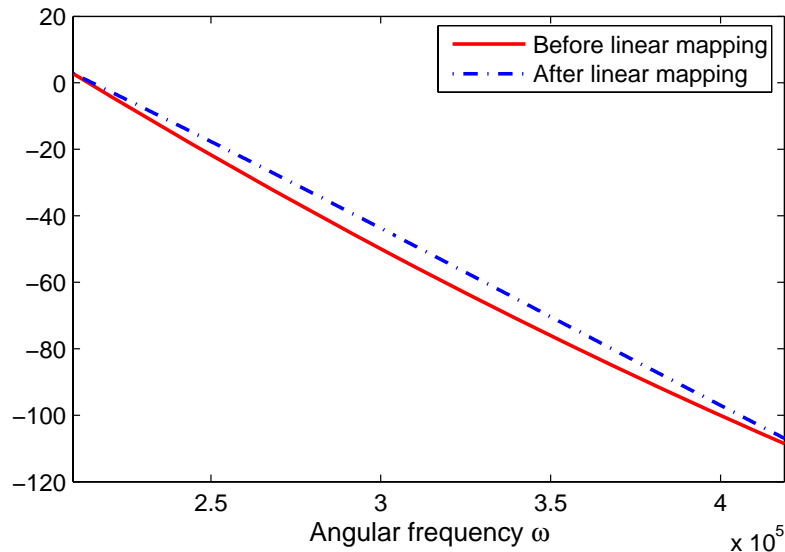


Figure 4.14 Comparison of unwrapped phase spectrum before and after linear mapping

It has been found that a simple linear interpolation works adequately, provided that the frequency step in the original $G(\omega)$ is small compared to the rate at which it is changing.

To achieve this, zero padding to the received time-series signal may be usually necessary in order to enhance resolution (or reduce the step size of frequency). The zero padding is also beneficial to reduce interpolation errors, at the expense of increased computational time and memory requirements. Moreover, the width of the mapping region, or the bandwidth of mapping, must be determined depending on the frequency bandwidth of the original signal. If the bandwidth is set too small, part of spectrum information may be lost, resulting in unacceptable error in the dispersion removal. On the other hand, if the bandwidth is chosen too large, $K(\omega)$ may be not a monotonic function in the selected region, thus causing discrepancy in the interpolation. Finally, it may be noted that the linear mapping can be performed in positive-only frequency region of $G(\omega)$ since $G(\omega)$ is an even function and half-plane of frequency is a mirror to the other.

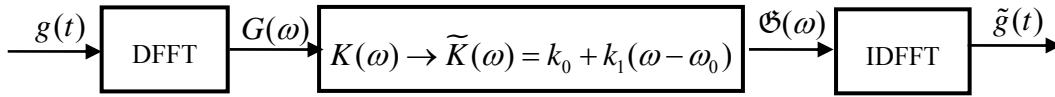


Figure 4.15 Block diagram of the dispersion removal procedure

To summarize, a block diagram for the dispersion removal is given in Figure 4.15, and steps to apply dispersion removal are as follows:

- Pad the received time-series signal, $g(t)$, with zeros to yield a sequence that provides good resolution in frequency domain.
- Perform DFFT on the zero-padded signal to obtain $G(\omega)$.
- Calculate the dispersion relation, $K(\omega)$, of the specific mode through the higher-order plate theory; or simply retrieve data from a pre-calculated table.
- Interpolate $G(\omega)$ to obtain $\mathfrak{G}(\omega)$ by linearly mapping $K(\omega)$ to $\tilde{K}(\omega) = k_0 + k_1(\omega - \omega_0)$ in the region with proper bandwidth centered around ω_0 .

- Pad $\mathfrak{G}(\omega)$ with both leading and trailing zeros; or simply use the corresponding values from $G(\omega)$.
- Apply IDFFT to $\mathfrak{G}(\omega)$ to obtain recompressed signal, $\tilde{g}(t)$.
- Trim $\tilde{g}(t)$ to remove the excessive part which is brought by the zero-padding in the first step.

4.3.2 Simulation and experimental verification

The verification is firstly conducted on simulated data. Four transient waves are assumed to be excited simultaneously and arrive a sensor after traveling different distances, $r_i = [0.4, 1.32, 1.6, 1.92] m$. The dispersion relation is assumed to be as the same as that of A_0 mode for an aluminum plate, and Eq. (4.46) is used to model the wave propagation and reconstruct dispersed transient waves. The simulated data is obtained by superposing individual dispersed transient waves (or wave packets).

The comparison between data before and after the dispersion removal is shown in Figure 4.16. The original simulated signal is presented in the figure with thick dash line. Clearly, slightly dispersion can be observed on the first wave packet. As the propagation distances increase, the last three wave packets suffer more dispersion and it is not easy to distinguish them from each other. The signal after the dispersion removal is plotted in the figure with thin dash line. After the dispersion removal, it can be seen that all wave packets are recompressed towards the shape of the excitation and it is very easy to identify individual wave packet. As the ambiguity in the evaluation of the shape of dispersed wave packets has been eliminated, the recompressed signal is ready for further processing, i.e., calculating propagation distances with the group velocity provided.

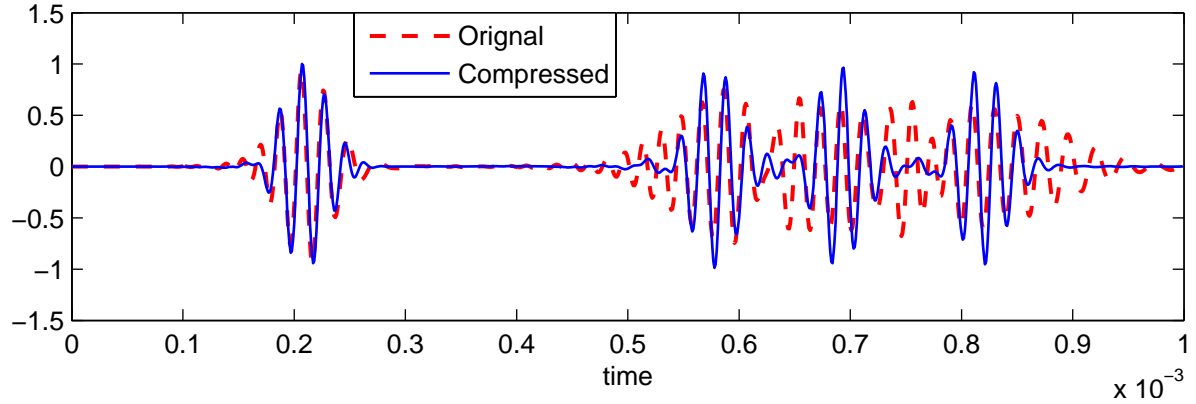


Figure 4.16 Dispersion removal applied to the simulated data

Verifications are also made to apply dispersion removal to wave propagation in aluminum plates. An AE (acoustic emission) sensor (PAC Micro-80) is placed on an aluminum plate, with the distance of about 0.254m (10 inch) to the actuators which are two piezoelectric discs bonded oppositely on the center of the plate. With a function generator (HP 33120A), a power amplifier (KH-7602) and a digital oscilloscope ((TDS210A), data are collected using actively excited flexural waves. Due to the reflections from the edges of the plate, multiple reflections (echoes) will be present followed by the direct arrival. The strength of the excitation was adjusted through changing the gain of the amplifier to make the amplitudes of the reflections significantly distinguishable from noise. It must be noted that parasitic extensional wave may also be excited due to the imperfectness of the actuator placement. However, since the extensional wave has smaller amplitude, but much faster group velocity comparing with the flexural wave, the influence of parasitic extensional waves can be neglected due to attenuation.

The upper plot in Figure 4.17 shows the collected data from a 1/8 inch plate. At about 0.1 ms, the wave packet with the largest amplitude is identified as the first arrival flexural wave packet. It is followed by a slightly dispersed wave packet at 0.3 ms with weakened amplitude. This wave packet is attributed to the first reflection through the shortest path,

which is about twice of the length of the perpendicular distance from the AE sensor to the nearest plate edge. After 0.4 ms, numerous wave packets which are overlapped with each other can be seen. It can be observed that these wave packets have larger amplitudes than that of the first reflection. Although this observation may seem to be not consistent with attenuations, it may be noted that these wave packets may represent multiple reflections which are superposed together and are not distinguishable in time domain due to the same propagation distances. After dispersion removal, the recompressed signal is retrieved and presented in the lower plot in Figure 4.17. Remarkable degree of dispersion compensation is achieved in this experiment setup. All dispersed wave packets are well recompressed into a nearly non-dispersive form in time domain. The originally overlapped wave packets are fairly separated; especially for the wave packets after 0.4 ms.

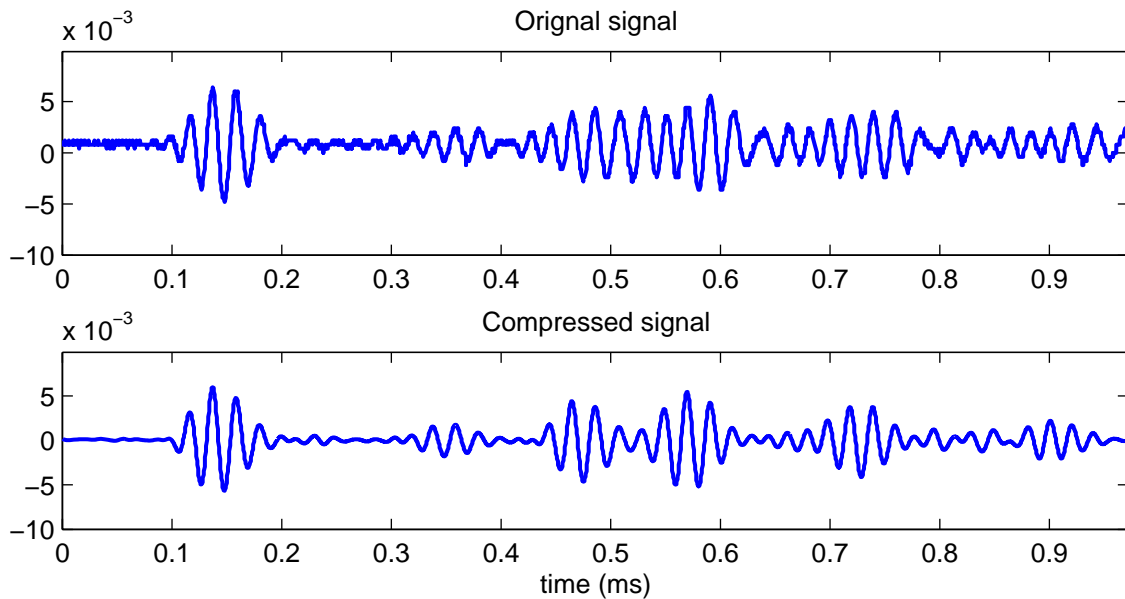


Figure 4.17 Original signal and compressed signal from 1/8 inch plate

Another experiment with similar configuration is also conducted. The thickness of the plate is 1/16 inch, half of the thickness in the previous experiment, while the central frequency of the excitation signal is twice of that in the previous experiment. Another

difference is that the distance between actuators and sensor is 15.24cm (6 inch). Since the plate is thinner, propagating waves suffer less attenuation thus that allows us to examine multiple times of reflection. Figure 4.18 shows the comparison between the original signal and the compressed signal. The result also shows that the proposed dispersion removal with the linear mapping algorithm performs very well.

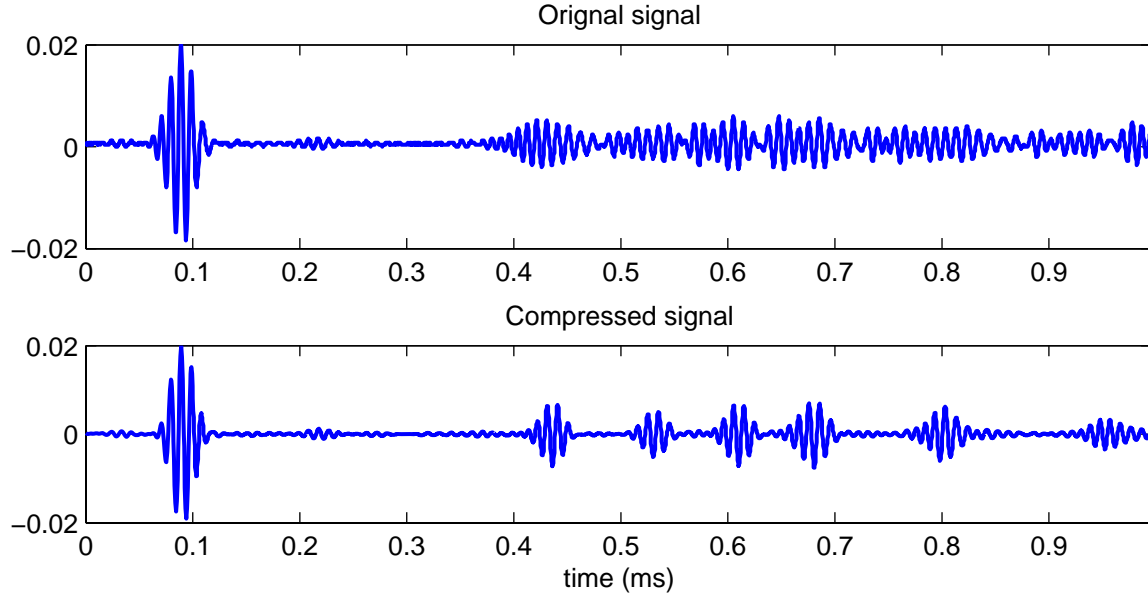


Figure 4.18 Original signal and compressed signal from 1/16 inch plate

4.4 Energy Decay Model

In this section, the leading-order asymptotic expansion in isotropic plates under axisymmetric load by using the higher-order plate theory and 3-D theory are introduced. An elastic energy decay model for detecting damage location will be developed accordingly.

4.4.1 The higher-order plate theory

Under axisymmetric loads in isotropic solids, all variables are expressed as functions of the radial coordinate r and time t . In this higher-order plate theory, a consistent displacement field can be expressed with cylindrical coordinates as

$$u_r(r, z, t) = u(r, t) + z\psi(r, t) + z^2\varphi(r, t) \quad (4.61)$$

$$u_3(r, z, t) = w(r, t) + z\psi_3(r, t) \quad (4.62)$$

where (u_r, u_3) are the radial and transverse displacements respectively, ψ is the rotation of transverse normal. These equations described displacements generated by both extensional and flexural waves. However, since the two types of waves are uncoupled from each other, (u, φ, ψ_3) and (ψ, w) can be solved by substituting Eq. (4.61) and (4.62) into motion equations of the extensional and flexural waves, respectively.

For extensional wave, the dimensionless motion equation can be established as

$$\alpha(\nabla^2 - \frac{1}{r^2})(u + \frac{1}{3}\varphi) + (\alpha - 2)\kappa \frac{\partial \psi_3}{\partial r} + q_r = \ddot{u} + \frac{1}{3}\ddot{\varphi} \quad (4.63)$$

$$\alpha(\nabla^2 - \frac{1}{r^2})(\frac{5}{3}u + \varphi) + \frac{5}{3}[\kappa(\alpha - 2) - 2\kappa_4^2] \frac{\partial \psi_3}{\partial r} - \frac{20}{3}\kappa_4^2\varphi + n_r = \frac{5}{3}\ddot{u} + \ddot{\varphi} \quad (4.64)$$

$$\kappa_4^2 \nabla^2 \psi_3 + [2\kappa_4^2 - \kappa(\alpha - 2)] \frac{1}{r} \frac{\partial}{\partial r}(r\varphi) - 3\kappa(\alpha - 2) \frac{1}{r} \frac{\partial}{\partial r}(ru) - 3\kappa^2 \alpha \psi_3 + m = \ddot{\psi}_3 \quad (4.65)$$

where $\nabla^2 = \frac{1}{r} \frac{\partial}{\partial r}(r \frac{\partial}{\partial r})$. Applying Laplace and first-order Hankel transforms to Eq. (4.63)

and (4.64), and applying Laplace and the zero-order Hankel transforms to Eq. (4.65). and define the following transformed variables,

$$\begin{aligned} \tilde{u}(k, s) &= \int_0^\infty \exp(-st) dt \int_0^\infty r J_1(kr) u(r, t) dr \\ \tilde{\varphi}(k, s) &= \int_0^\infty \exp(-st) dt \int_0^\infty r J_1(kr) \varphi(r, t) dr \\ \tilde{\psi}_3(k, s) &= \int_0^\infty \exp(-st) dt \int_0^\infty r J_0(kr) \psi_3(r, t) dr \\ \tilde{m}(k, s) &= \int_0^\infty \exp(-st) dt \int_0^\infty r J_0(kr) m(r, t) dr \end{aligned} \quad (4.66)$$

where $s = i\omega$ is the Laplace transform parameter, k the Hankel transform parameter, $\tilde{u}, \bar{u}, \tilde{\tilde{u}}, \dots$ are the Hankel transform, Laplace transform, and the joint Hankel and Laplace

transform of function u , respectively, $\dots, J_n(kr)$ is the Bessel function of order n . Eq. (4.63)-

(4.65) can be written in matrix form as

$$(\mathbf{T} + s^2\mathbf{M})\tilde{\mathbf{U}} = \tilde{m}\mathbf{I}_3 \quad (4.67)$$

$$\mathbf{T} = \begin{bmatrix} \alpha k^2 & \alpha k^2 / 3 & \kappa(\alpha - 2)k \\ \frac{5}{3}\alpha k^2 & \alpha k^2 + \frac{20}{3}\kappa_4^2 & \frac{5}{3}[\kappa(\alpha - 2) - 2\kappa_4^2]k \\ 3\kappa(\alpha - 2)k & [\kappa(\alpha - 2) - 2\kappa_4^2]k & \kappa_4^2 k^2 + 3\alpha k^2 \end{bmatrix} \quad (4.68)$$

$$\mathbf{M} = \begin{bmatrix} 1 & 1/3 & 0 \\ 5/3 & 1 & 0 \\ 0 & 0 & 1 \end{bmatrix} \quad (4.69)$$

where $\tilde{\mathbf{U}} = [\tilde{u}, \tilde{\varphi}, \tilde{\psi}_3]^T$ is the generalized displacement, $\mathbf{I}_3 = [0, 0, 1]^T$.

The solution of Eq. (4.67) is given by

$$\tilde{\mathbf{U}} = (\mathbf{T} + s^2\mathbf{M})^{-1} \tilde{m}\mathbf{I}_3 = \frac{\text{adj}(\mathbf{T} + s^2\mathbf{M})}{|\mathbf{T} + s^2\mathbf{M}|} \tilde{m}\mathbf{I}_3 \quad (4.70)$$

and the eigenvalues of matrix $\mathbf{T} + s^2\mathbf{M}$ are with respect to different extensional wave modes, which may be expressed in the form:

$$\omega^2 = W_1^2(k), W_2^2(k), W_3^2(k) \quad (4.71)$$

Eq. (4.70) can be further decomposed into the form of matrix as

$$\tilde{\mathbf{U}} = \mathbf{A}_T \begin{Bmatrix} (s^2 + W_1^2)^{-1} \\ (s^2 + W_2^2)^{-1} \\ (s^2 + W_3^2)^{-1} \end{Bmatrix} \tilde{m} \quad (4.72)$$

and

$$\mathbf{A}_T = \mathbf{D}_T \mathbf{\Omega}^{-1} = \begin{bmatrix} 0 & m_{12}T_{23} - T_{13} & T_{12}T_{23} - T_{22}T_{13} \\ 0 & m_{21}T_{13} - T_{23} & T_{21}T_{13} - T_{11}T_{23} \\ 1 - m_{12}m_{21} & T_{11} + T_{22} - m_{12}T_{21} - m_{21}T_{12} & T_{11}T_{22} - T_{12}T_{21} \end{bmatrix} \begin{bmatrix} 1 & W_2^2 + W_3^2 & W_2^2W_3^2 \\ 1 & W_3^2 + W_1^2 & W_3^2W_1^2 \\ 1 & W_1^2 + W_2^2 & W_1^2W_2^2 \end{bmatrix}^{-1} \quad (4.73)$$

where T_{ij} and m_{ij} are the elements of the \mathbf{T} and \mathbf{M} matrices.

By taking inverse Laplace transform to Eq. (4.72), and using the formula of Laplace transform $L^{-1}\left\{\frac{1}{s^2 + W_i^2}\right\} = \frac{\sin W_i t}{W_i}$ and the convolution theorem, it yields:

$$\tilde{\mathbf{U}}(\mathbf{k}, t) = \mathbf{A}_T \int_0^t \begin{Bmatrix} W_1^{-1} \sin W_1(t - \xi) \\ W_2^{-1} \sin W_2(t - \xi) \\ W_3^{-1} \sin W_3(t - \xi) \end{Bmatrix} \tilde{m}(k, \xi) d\xi \quad (4.74)$$

Applying inverse Hankel transform of $\tilde{\mathbf{U}}$ leads to

$$\begin{Bmatrix} u \\ \varphi \\ \psi_3 \end{Bmatrix} = \int_0^t k \text{diag} [J_1(kr), J_1(kr), J_0(kr)] \mathbf{A}_T \mathbf{H}(t, k) dk \quad (4.75)$$

$$h_i(t, k) = W_i^{-1} \int_0^t \sin W_i(t - \xi) \tilde{m}(k, \xi) d\xi \quad (4.76)$$

where $\mathbf{H} = [h_1, h_2, h_3]^T$, and $i = 1, 2, 3$. Although the integrals in Eq. (4.75) represent exact solutions for displacement vector, it is usually very difficult to directly evaluate them. The alternatives are numerical evaluation, or an approximate analytical evaluation. Asymptotic method can be applied to resolve the difficulty. For long duration (time) and far field (distances), the Bessel functions in Eq. (4.75) can be replaced by their asymptotic expansions

$$\begin{aligned} J_0(kr) &\sim \sqrt{\frac{2}{\pi kr}} \cos(kr - \pi/4) \\ J_1(kr) &\sim \sqrt{\frac{2}{\pi kr}} \sin(kr - \pi/4) \end{aligned} \quad (4.77)$$

After matrix manipulation and applying the method of stationary phase, the solution for a pure impulsive point load can be given by:

$$\begin{cases} u(r,t) \\ \varphi(r,t) \\ \psi_3(r,t) \end{cases} \sim \frac{1}{2\pi\sqrt{rt}} \operatorname{Re} \sum_i \sum_{\substack{\text{stationary} \\ \text{points } k}} \frac{F_{ji}(k)}{\sqrt{|W_i''(k)|}} \exp i[kr - W_i(k)t - \frac{\pi}{4} \operatorname{sgn} W_i''(k)] \quad (4.78)$$

where sgn stands for the sign function, $j, i = 1, 2, 3$, $F_{ji}(k)$ are associated with the initial conditions or loading with respect to the three variables, r is the wave propagation distance, $t = r/c_g$ is the traveling time, $k = k(r, t)$ is the stationary point which is the root of the equations,

$$W_i'(k) = \frac{r}{t}, \text{ and } k > 0, \frac{r}{t} > 0 \quad (4.79)$$

Eq. (4.78) and (4.79) indicate that the amplitudes of displacements are proportional to $1/\sqrt{rt}$ while the approximation only breaks down near points when $W_i''(k_0) = 0$. As in the previous section, the transient wave packet propagates a constant velocity c_g at central frequency ω_0 , it can be further concluded that the amplitude of extensional wave decays at a rate inversely proportional to the propagation distance based on the assumption of long time and far field.

For flexural wave, the dimensionless motion equation can be written as

$$\ddot{w} - \kappa^2 \nabla^2 w - \frac{\kappa^2}{r} \frac{\partial}{\partial r} (r\psi) = q, \quad t > 0 \quad (4.80)$$

$$\ddot{\psi} + 3\kappa^2 \left(\psi + \frac{\partial w}{\partial r} \right) - \alpha \left(\nabla^2 - \frac{1}{r^2} \right) \psi = 0 \quad (4.81)$$

In a similar approach to the extensional waves, the flexural wave in the plate can be solved by using the Laplace and the Hankel transformations.

$$\mathbf{U}(r, t) = \int_0^\infty k \operatorname{diag} [J_0(kr), J_1(kr)] \mathbf{A}_b dk \int_0^t \begin{cases} W_1^{-1} \sin W_1(t - \xi) \\ W_2^{-1} \sin W_2(t - \xi) \end{cases} \tilde{q}(k, \xi) d\xi \quad (4.82)$$

$$\mathbf{A}_b = \frac{1}{W_1^2 - W_2^2} \begin{bmatrix} W_1^2 - \alpha k^2 - 3\kappa^2 & -W_2^2 + \alpha k^2 + 3\kappa^2 \\ -3\kappa^2 k & 3\kappa^2 k \end{bmatrix} \quad (4.83)$$

For a pure impulsive point load, the solution can be evaluated by asymptotically

$$\begin{cases} w(r, t) \\ \psi(r, t) \end{cases} \sim \frac{1}{2\pi\sqrt{rt}} \operatorname{Re} \sum_i \sum_{\substack{\text{stationary} \\ \text{points } k}} \frac{F_{ji}(k)}{\sqrt{|W_i'(k)|}} \exp i[kr - W_i(k)t - \frac{\pi}{4} \operatorname{sgn} W_i''(k)] \quad (4.84)$$

Similar conclusion as that for the extensional waves can be yielded for the flexural waves. Note that the elastic wave propagation in a plate has similar properties of acoustic wave traveling in air. For isotropic plates, the elastic wave propagates omni-directionally and the amplitude attenuation is identical on a circle of which the center is the position of the excitation source; for anisotropic plates, the attenuation rate varies directionally.

4.4.2 The 3-D elasticity theory

For comparison with the higher-order plate theory, the wave behavior under axisymmetric deformation in an isotropic plate provided by “exact” three-dimensional elasticity is derived below. The displacement equations of motion in cylindrical coordinates are

$$(\lambda + 2G)(\nabla^2 u - \frac{u}{r^2}) + G \frac{\partial^2 u}{\partial z^2} + (\lambda + G) \frac{\partial^2 w}{\partial r \partial z} + F_r = \rho \ddot{u} \quad (4.85)$$

$$G \nabla^2 w + (\lambda + 2G) \frac{\partial^2 w}{\partial z^2} + (\lambda + G) \frac{1}{r} \frac{\partial^2 (ru)}{\partial z \partial r} + F_z = \rho \ddot{w} \quad (4.86)$$

where u and w are the displacement components in the radial and thickness directions, respectively. F_r and F_z are the body forces. To make the variables dimensionless, the following non-dimensional variables and quantities are defined by introducing a length scale

$$h/2, \text{ a typical time scale } \tau = \frac{h}{2c_T} :$$

$$r' = \frac{r}{h/2}, \quad z' = \frac{z}{h/2}, \quad t' = \frac{t}{h/(2c_r)}, \quad u' = \frac{u}{h/2}, \quad w' = \frac{w}{h/2}, \quad F'_i = \frac{F_i}{2G/h} \quad (4.87)$$

The dimensionless equations of motion is

$$\alpha(\nabla^2 u - \frac{u}{r^2}) + \frac{\partial^2 u}{\partial z'^2} + (\alpha - 1) \frac{\partial^2 w}{\partial r \partial z'} + F_r = \ddot{u} \quad (4.88)$$

$$\nabla^2 w + \alpha \frac{\partial^2 w}{\partial z'^2} + (\alpha - 1) \frac{1}{r} \frac{\partial^2}{\partial r \partial z'}(ru) + F_z = \ddot{w} \quad (4.89)$$

with the traction-free boundary conditions, $\sigma_{zz} = \tau_{rz} = 0$, on the two plate surfaces, which can be written as

$$\begin{aligned} \alpha w_{,z} + (\alpha - 2) \left(\frac{u}{r} + u_{,r} \right) &= 0 \\ u_{,z} + w_{,r} &= 0 \end{aligned} \quad (4.90)$$

where at $z = \pm 1$. The solution of Eq. (4.88)-(4.89) is the sum of a particular solution and the general solution of the associated homogeneous equation.

For $F_r = F_z = 0$, Eq. (4.88) and (4.89) can be reduced to ordinary differential equations

$$\frac{d^2 \hat{u}}{dz^2} + (\omega^2 - \alpha k^2) \hat{u} - (\alpha - 1) k \frac{d\hat{w}}{dz} = 0 \quad (4.91)$$

$$\alpha \frac{d^2 \hat{w}}{dz^2} + (\omega^2 - k^2) \hat{w} + (\alpha - 1) k \frac{d\hat{u}}{dz} = 0 \quad (4.92)$$

with boundary conditions

$$\begin{aligned} \alpha \frac{d\hat{w}}{dz} + (\alpha - 2) k \hat{u} &= 0 \\ \frac{d\hat{u}}{dz} - k \hat{w} &= 0 \end{aligned} \quad (4.93)$$

where \hat{u} and \hat{w} as the displacements after applying FT with respect to t and the Hankel

transform with respect to r

$$\begin{aligned}\hat{u}(k, z, \omega) &= \int_{-\infty}^{\infty} e^{-i\omega t} dt \int_0^{\infty} r J_1(kr) u(r, z, t) dr \\ \hat{w}(k, z, \omega) &= \int_{-\infty}^{\infty} e^{-i\omega t} dt \int_0^{\infty} r J_0(kr) w(r, z, t) dr\end{aligned}\quad (4.94)$$

Solving Eq. (4.91)-(4.93), two uncoupled systems of linear equations are formed

$$\begin{bmatrix} \frac{\omega^2 - 2k^2}{k} \cos p & -2k \cos q \\ -2p \sin p & -\frac{\omega^2 - 2k^2}{q} \sin q \end{bmatrix} \begin{Bmatrix} a_1 \\ a_3 \end{Bmatrix} = 0 \quad (4.95)$$

$$\begin{bmatrix} \frac{\omega^2 - 2k^2}{k} \sin p & -2k \sin q \\ 2p \cos p & \frac{\omega^2 - 2k^2}{q} \cos q \end{bmatrix} \begin{Bmatrix} a_2 \\ a_4 \end{Bmatrix} = 0 \quad (4.96)$$

The requirement of the nontrivial solutions for a_i leads to dispersion relation by solving the following equation

$$\omega^4 = 4k^2 q^2 \left[1 - \frac{p \tan(p + \gamma)}{q \tan(q + \gamma)} \right] \quad (4.97)$$

where $\gamma = 0$ and $\pi / 2$ represent symmetric modes and anti-symmetric modes, respectively. Eq. (4.97) is identical to the Rayleigh-Lamb equation which was derived from 2-D plane strain deformation of elastic plates. The dispersion relation results in an infinite number of wave modes ordered by S_0, S_1, S_2, \dots and A_0, A_1, A_2, \dots for symmetric and anti-symmetric modes, respectively.

To compose the complete solution the principle of superposition may be applied to the linear system for all values of k and all modes of n ,

$$u(r, z, t) = \sum_{n=1}^{\infty} \int_0^{\infty} kJ_1(kr)A_n(t, k)u_n(k, z)dk \equiv H_1^{-1}\{A_n u_n\} \quad (4.98)$$

$$w(r, z, t) = \sum_{n=1}^{\infty} \int_{-\infty}^{\infty} kJ_0(kr)A_n(t, k)w_n(k, z)dk \equiv H_0^{-1}\{A_n w_n\} \quad (4.99)$$

where

$$A_n(t, k) = \frac{1}{2\pi} \int_{-\infty}^{\infty} a_n(k, \omega)e^{i\omega t} d\omega \equiv F^{-1}\{a_n(k, \omega)\} \quad (4.100)$$

and $F^{-1}\{\}$, $H_0^{-1}\{\}$, $H_1^{-1}\{\}$ are the inverse operators of the Fourier, Hankel zero-order and first-order transforms, respectively. Further, Eq. (4.98) and (4.99) can be evaluated by stationary phase approximation for large values of t and they also indicate that if a disturbance is produced at a point of an elastic plate, then the waves can be considered as plane waves at a great distance from the center of disturbance by expanding the Bessel's functions.

For $F_r \neq 0, F_z \neq 0$, Eq. (4.88) and (4.89) can be written in matrix form,

$$\mathbf{L}\tilde{\mathbf{U}} - s^2\tilde{\mathbf{U}} = -\tilde{\mathbf{F}} \quad (4.101)$$

with boundary conditions

$$\begin{bmatrix} 1 & 0 \\ 0 & \alpha \end{bmatrix} D\tilde{\mathbf{U}} + \begin{bmatrix} 0 & -k \\ (\alpha-2)k & 0 \end{bmatrix} \tilde{\mathbf{U}} = \mathbf{0} \quad \text{at } z = \pm 1 \quad (4.102)$$

where $\tilde{\mathbf{U}} = [\tilde{u}, \tilde{w}]^T$, $\hat{\mathbf{F}} = [\tilde{F}_r, \tilde{F}_z]^T$, $\mathbf{L} = \begin{bmatrix} D^2 - \alpha k^2 & -(\alpha-1)kD \\ (\alpha-1)kD & \alpha D^2 - k^2 \end{bmatrix}$, $D = \frac{d}{dz}$, $D^2 = \frac{d^2}{dz^2}$, and

$$\begin{aligned} \tilde{F}_r(z, s, k) &= \int_0^{\infty} e^{-st} dt \int_0^{\infty} rJ_1(kr)F_r(r, z, t) dr \\ \tilde{F}_z(z, s, k) &= \int_0^{\infty} e^{-st} dt \int_0^{\infty} rJ_0(kr)F_z(r, z, t) dr \end{aligned} \quad (4.103)$$

The homogenous solution of Eq. (4.101) also represents a standard eigenvalue problem. Note that a complete set of eigenfunctions have been developed by [57] in a finite plate. The transient wave solutions in an infinite plate can be constructed from the above eigenfunctions in a finite plate. Considering a transverse point force with magnitude P at $(0, 0, z_0)$, its dimensionless expression is given by

$$F_r = 0, F_z = I \frac{\delta(r)}{2\pi r} \delta(z - z_0) \delta(t) \quad (4.104)$$

where $I = 4P/(Gh^2)$ is the normalized magnitude of the applied point force. In this case, the homogenous solution can be given by

$$\begin{Bmatrix} u \\ w \end{Bmatrix} = \frac{I}{2\pi} \sum_{n=1}^{\infty} \int_0^{\infty} k \begin{Bmatrix} J_1(kr)u_n(z, k) \\ J_0(kr)w_n(z, k) \end{Bmatrix} \frac{w_n(z_0, k)}{M_n(k)\omega_n} \sin \omega_n t dk \quad (4.105)$$

Note that if the force P is applied on the mid-plane ($z_0 = 0$), or two equal forces $P/2$ with same direction acting along the z axis on the two plate surfaces at the same time, the contribution from the symmetrical modes is zero. On the other hand, if two equal opposite forces $P/2$ act along the z axis on the two plate surfaces at the same time, then the contribution from the anti-symmetric modes is zero. For large values of r and t , the leading order asymptotic expansions of Eq. (4.105) is

$$u(r, z, t) \sim \frac{I}{2\pi\sqrt{rt}} \operatorname{Re} \sum_{n=1}^{\infty} \frac{k^{3/2} u_n(z, k) w_n(z_0, k)}{\sqrt{|\omega_n''|} M_n(k) \omega_n} \exp i(kr - \omega_n t + \theta_1) \quad (4.106)$$

$$w(r, z, t) \sim \frac{I}{2\pi\sqrt{rt}} \operatorname{Re} \sum_{n=1}^{\infty} \frac{k^{3/2} w_n(z, k) w_n(z_0, k)}{\sqrt{|\omega_n''|} M_n(k) \omega_n} \exp i(kr - \omega_n t + \theta_2) \quad (4.107)$$

where $\theta_1 = -\pi(\operatorname{sgn} \omega'' + 1)/4$, $\theta_2 = -\pi(\operatorname{sgn} \omega'' - 1)/4$ and $k = k(r, t)$ is the stationary point which is a root of

$$\omega'_n(k) = \frac{r}{t}, \quad k > 0, \quad \frac{r}{t} > 0 \quad (4.108)$$

It can be immediately seen that these equations have similar form as those solutions derived in the last Section. The solution of response to axisymmetric load by using 3-D elastic theory also infers that the amplitude of extensional wave decays in proportional to $1/r$ based on the assumption of long times and far field. The results also hold true unless ω''_n approaches zero. In that case, the decay proceeds more rapidly where Airy approximation may be required.

4.4.3 Energy decay model

It is concluded based on the higher-order theory and the 3-D elastic theory that at far field the intensity of the envelope of a stress wave propagating through a plate attenuates at a rate that is inversely proportional to the distance from the excitation source. The derivation of this geometric spreading has been made as described in the previous section. Experiments to verify the conclusion are made with the same configuration used in the section 4.3.2 and the results are plotted in Figure 4.19. The only difference in the verification study is that the AE sensor is initially located 2.54 cm away from the center of the actuator, and then gradually increase the distance with increment of 5.08 cm (2 inch).

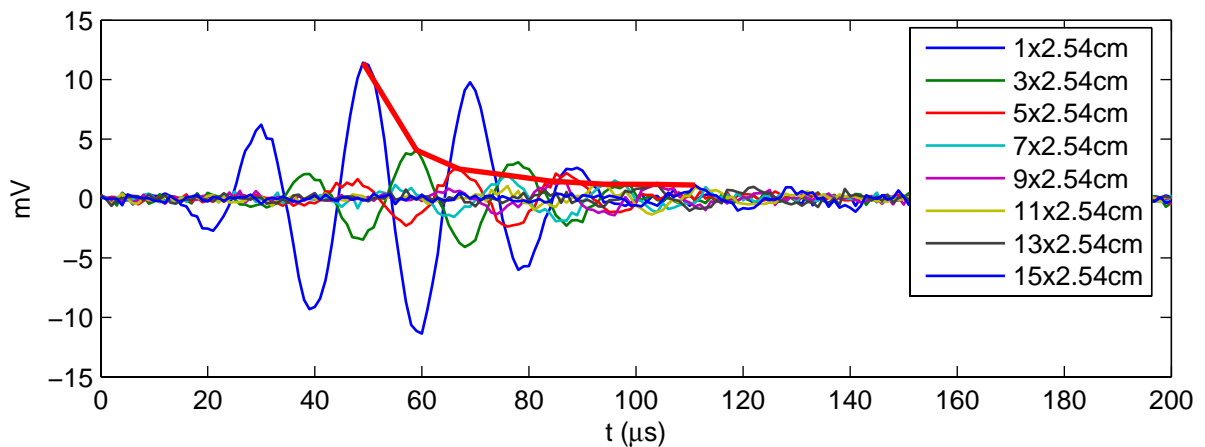


Figure 4.19 Measured time-series signals with different distances

Nine sensor data, which have been filtered to include only the first arrival of the wave packet, are plotted in the figure. Since the disturbance from boundary reflections has been excluded by the filtering, the waveforms exactly record the surface displacements of the symmetrical excitation (wave propagates in S_0 mode). As the propagating distance increases, the signals can be seen as gradually

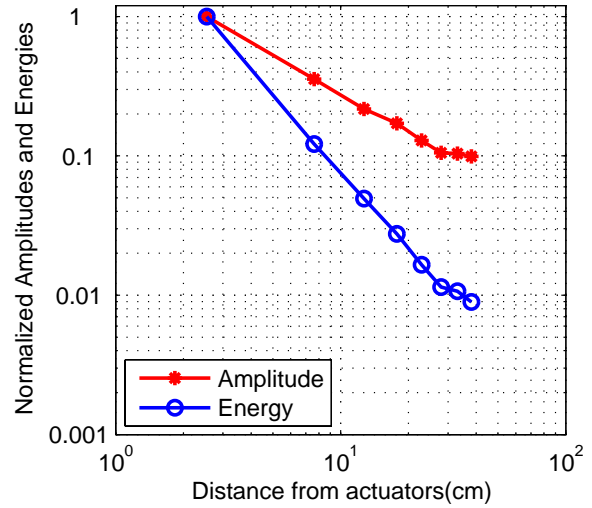


Figure 4.20 Normalized amplitude and signal energy decay ratios

shifting along the time axis and deducing significant decay in amplitude. A curve drawn by a bold line is formed by connecting the top peaks of each waveform, which are the largest amplitudes. Since the dispersion is not significant and the wave packet travels in constant group velocity, the curve effectively reveals the geometric spreading between amplitude and distance.

To reveal the relationship clearly, the peak amplitudes and distances are imported to be displayed in coordinates with logarithm-scale, which are shown in Figure 4.20 as the line marked with asterisks. From this plot, it can be seen that the slope of the line is approximately -1, except minor variances at the large distance. Since the amplitude of the propagating wave continuously decreases whereas the strength of noise remains at the same level for a given environment, the SNR (signal-noise ratio) gradually decreases. The measurements are eventually contaminated by noise and the largest amplitude may not truly indicate the peak of the propagating wave. Therefore, variances arise as the propagating distance increases. Nevertheless, the amplitude decay rate matches well with the prediction

within the coverage area where the signal strength is still sufficiently large. The *instantaneous power* of a deterministic signal $s(t)$ can be defined as

$$P_s(t) = s^2(t) \quad (4.109)$$

The *total energy*, thus, can be calculated as the integral of $P_s(t)$ over all time, i.e.,

$$T_s(t) = \int_{-\infty}^{\infty} s^2(t) dt = \frac{1}{2\pi} \int_{-\infty}^{\infty} |S(\omega)|^2 d\omega \quad (4.110)$$

where $S(\omega)$ is the FT of $s(t)$ and the equality in the time and frequency domains is in accordance with Parseval's theorem. In practice, a continuous signal can only be collected in discrete time during finite duration. Thus, it is meaningful to measure the *average power* for discrete time signals which may be expressed as the expectation of the square of the amplitude:

$$P_s = E[s^2] = \frac{1}{N} \sum_{n=1}^N s^2(n) \quad (4.111)$$

where $E[]$ represents expectation. From the amplitude decay rate being inversely proportional to the propagation distance, it is straightforward that the average power is inversely proportional to the square of distance. Figure 4.20 also plots the average power of collected data versus propagating distance in the line with circle marks.

As noticed in both figures, the noise is not always ignorable especially at locations away from the excitation source as the signal attenuates greatly. Based on the assumption that the SNR is significant large such that the signal is distinguishable from the noise, the collected signal can be modeled as a superposition of scattered wave and noise to take into account the effect of noise

$$x_p(n) = s_p(n) + v_p(n) \quad (4.112)$$

and

$$s_p(n) = \gamma_p \sum_{m=1}^M a_m(n) \quad (4.113)$$

where $n = 1 \cdots N$, N is the number of the collected data;

$p = 1 \cdots P$, P is the number of sensors deployed on the plate;

$m = 1 \cdots M$, M is the number of excitation;

$x_p(n)$ is the n^{th} discrete data of the received waveform at the p^{th} sensor;

$s_p(n)$ is the synthesized scattered waveforms received by the p^{th} sensor;

$v_p(n)$ is the background noise;

γ_p is the sensor gain factor;

$a_m(n)$ is the amplitude of waveform scattered from m^{th} excitation.

The average power may be expressed by combing Eq. (4.111) and (4.112)

$$\begin{aligned} E[x_p^2(n)] &= \frac{1}{N} \sum_{n=1}^N (s_p(n) + v_p(n))^2 \\ &= \frac{1}{N} \sum_{n=1}^N s_p^2(n) + \frac{1}{N} \sum_{n=1}^N v_p^2(n) + \frac{2}{N} \sum_{n=1}^N s_p(n)v_p(n) \end{aligned} \quad (4.114)$$

If the noise can be modeled as additive white Gaussian noise (AWGN) characterized by a stationary Gaussian distribution which is subject to distribution $\sim N(0, \sigma_n^2)$ and provided that the wave signal can be uncorrelated from the noise, the third term in the right hand side (RHS) of Eq. (4.114) can be decomposed as

$$\frac{2}{N} \sum_{n=1}^N s_p(n)v_p(n) = \frac{2}{N} \left(\sum_{n=1}^N s_p(n) \right) \left(\sum_{n=1}^N v_p(n) \right) \quad (4.115)$$

Since the expectation of noise is zero, the term (4.115) equals to zero and can be eliminated from Eq. (4.114). Also, the square of the background noise, $v_p^2(n)$, has a χ^2

distribution with mean $E[v_p^2(n)] = \sigma_n^2$ and variance $\frac{2\sigma_n^4}{N}$. Note that according to central

limit theorem, if N is large enough, the second term of the RHS in Eq. (4.114), $\frac{1}{N} \sum_{n=1}^N v_p^2(n)$,

can be approximated well with a normal distribution, namely, $\frac{1}{N} \sum_{n=1}^N v_p^2(n) \sim N(\sigma_n^2, \frac{2\sigma_n^4}{N})$. As

a result, Eq. (4.114) can be simplified as

$$z_p = E[s_p^2(n)] + \sigma_n^2 \quad (4.116)$$

where the scalar $E[x_p^2(n)]$ is defined as z_p , In practice, the average power can be calculated by using ensemble average over a time window, and the variance of background noise can be obtained from measurements. Furthermore, if there is only one excitation source, the conclusion for amplitude decay of propagating wave in a plate can be immediately applied and leads to a more concise form as,

$$z_p = \frac{\gamma_p^2 P_{s0}}{\|\mathbf{p} - \mathbf{r}_p\|^2} + \sigma_n^2 \quad (4.117)$$

where P_{s0} denotes the average power of the excitation, \mathbf{p} and \mathbf{r}_p are the position vector of excitation and the p^{th} sensor, respectively, and $\|\cdot\|$ indicates Euclidean distance. In this equation, three unknown variables, $\mathbf{p} = (x, y)$ and the sensor gain γ_p are present. Thus, at least three or more sensors are needed to provide solution for the location of the excitation. Modeling based on Eq. (4.117) is often called *energy decay model*.

4.5 Summary

In this chapter, the higher-order plate theory has been used to obtain dispersion

relation for both extensional and flexural waves. Phase and group velocities are derived, and are compared with those from 3-D elastic theory. Although the higher-order theory only gives finite number of modes opposed to infinite numbers of mode based on 3-D theory, the first few modes, A_0 or S_0 mode, have been more than sufficient for locating damage in active diagnosis. The comparison shows that the dispersion curves from the higher-order plate theory are in agreement with those from 3-D elastic theory, especially in the region where the frequency is lower than the cut-off frequency. Since the 3-D elastic theory can only evaluate dispersion relation numerically, the higher-order theory outperforms it in resource-restrained application, such as wireless sensor, and gives sufficiently accurate results.

The dispersion phenomenon is illustrated by applying Fourier transform to 1-D transient wave, and analytic expressions of wave dispersion for two types of narrowband wave are given. Based on the analysis, a linear mapping algorithm is proposed to remove dispersion. After applying the dispersion removal, dispersed waves can be recompressed in time domain. Multiple wave packets that overlap due to multiple reflections can be more easily distinguished. Additionally, since the dispersion is almost removed, many methods to detect damages using time of arrival are beneficial from the dispersion removal.

Leading-order asymptotic solutions of the wave field in isotropic plates are derived by both the high-order theory and the 3-D elastic theory for axisymmetric load which can be used to model piezoelectric actuator used in active damage localization. Both results prove that the amplitude of elastic wave propagated in plate decays inversely proportional to the propagation distance at long times and far field. The conclusion is further used to develop an energy decay model, which can be summarized as that the energy contained in an elastic wave packet decays inversely proportional to the square of the propagation distance.

5 Active Damage Localization for Isotropic Plates

5.1 Overview of Active Damage Localization

For active diagnosis, guided waves such as Lamb wave are widely used because they can propagate over long distances and cover relatively large areas of plate-like structures. For SHM, embedding piezoelectric elements into structures to excite and sense Lamb waves as an online method to assess damages has received considerable attention since initial efforts were conducted by Cawley and Chang [20, 58-60].

Damage localization methods for active diagnosis may fall into three categories: direction of arrival (DOA), time difference of arrival (TDOA), and sensor signal strength or energy. DOA extracts damage location from the phase differences of collected signals and is strictly applicable when the acoustic source emits a coherent narrowband signal [61-63]. TDOA measures relative time delays among sensors to search damage location. Although it has been extensively investigated and is also suited to for broadband excitation [64, 65], precise inter-sensors synchronization is required. Nevertheless, wireless sensors typically suffer from large latency for communication and processing, which is a key barrier to impede the usage of TDOA with wireless sensors. The third type of method was inspired from an energy based method for sound-source localization reported in [66-68]. In contrast with other two methods, the energy based approach does not require accurate time synchronization and does not need extreme high sampling speed. Thus, the requirement for communication and processing capability of wireless sensors can be lessened. In particular for active diagnosis, since excitations are normally given narrowband signals, it is very efficient to use this method to reduce the energy consumption on individual sensor and to make energy-efficient wireless sensor to be practical.

Additionally, redundant information from different sensors is usually encountered and leads damage localization to nonlinear least-squares (NLS) problems. The evaluation of Jacobian matrices in NLS formulations impedes NLS problems to be solved resources-constrained wireless sensors. This chapter establishes and compares damage localization algorithms based on the TDOA and the energy approach, and develops algorithms to facilitate their applications in local wireless sensor network.

5.2 Active Damage Localization Using Correlation

For conventional damage localization techniques, the time-of-flight (time of arrival) of reflected waves from damage needs to be measured in combination with specific algorithms to locate the damage [69, 70]. Traditionally, either first threshold crossing or envelop peak detection is used to determine the difference in time of arrival, followed by a triangulation scheme to locate the damage. For example, the first threshold crossing can be defined as to obtain the time at which received diagnostic signals crosses a preset threshold. However, if the structural geometry is complicated, the signals are subject to noise, and dispersion is significant, the ambiguity of evaluating of time-of-flight is not negligible and may result in significant variations in damage localization.

Therefore, it is desirable to devise a method that would allow the detection of specific phase point in the signals so that the same phase point could be determined. A typical technique to measure time delays in acoustics emission is cross-correlation. The cross-correlation function (CCF) is defined as the product of two functions, where one function is shifted version of the other

$$C_{xy}(t) = \int_{-T}^T x(\tau)y(\tau+t)d\tau \quad (5.1)$$

Strictly speaking, such an approach holds only in non-dispersive or at most slightly dispersive mediums, e.g., the propagation of sound waves in air [71].

Ziola and Gorman [72] proposed a phase point detection method for dispersive medium using the cross-correlation technique and such method was also recently explored in [73, 74]. The basic idea behind this method is to use a single frequency cosine wave modulated by a Gaussian pulse to be cross-correlated with received signal. It was concluded in [72] that good results were obtained. It is must be noted that, mathematically, the method is equivalent to apply a band-pass filter to collected signals and must be based on an assumption that the pass-band is narrow enough to make dispersion insignificant. Effectively, this is still a method based on narrowband waves. Wavelet or other signal processing techniques, which can construct similar filters, may also yield comparable or even better results. However, this method is inexact since the assumption may be violated in many practical cases.

In signal processing, the cross-correlation is a measure of similarity of two signals and is a function of the relative time between the signals. For continuous function, the CCF has been already given in Eq. (5.1); while for discrete functions, the CCF can be written as

$$C_{xy}(m) = \sum_{n=1}^N x(n)y(n+m) \quad (5.2)$$

where N is the number of digital samples and m is the lag number which must be less than N . A similar function, cross-covariance function, can be defined as

$$\bar{C}_{xy}(m) = \sum_{n=1}^N (x(n) - \overline{x(n)})(y(n+m) - \overline{y(n)}) \quad (5.3)$$

where $\overline{x(n)}$ and $\overline{y(n)}$ represent the mean of the two sensor signals, respectively. Both $C_{xy}(m)$ and $\bar{C}_{xy}(m)$ are second-order measures and provide a statistical comparison of the

two signals except the mean values of the two signals are removed in $\bar{C}_{xy}(m)$. The CCF reflects the various frequency components held in common and also holds information about the relative phases of shared frequency components. From a practical point of view, CCF is useful to extract time differences between two signals [75]. That is, when the peak values in two data series are correlated, there is a peak in the correlation efficient curve, and the corresponding time lag represents the difference in the arrival time of these two peaks.

From the definition, the cross-correlation is similar in nature to the convolution of two sensor signals, and can be related to convolution by

$$C_{xy}(\tau) = f(-t) \otimes g(t) \quad (5.4)$$

where \otimes denotes convolution. If either f or g is an even function, CCF is identical to the convolution.

In [72], since the Gaussian pulse modulated cosine wave is symmetric with respect to its peak, CCF is identical to the convolution which convolutes the collected signal to an even function. From the convolution theorem of FT, it is identical to an inverse FT of the product of two signals in frequency spectrums. Noticing that the Gaussian pulse modulated cosine wave is a narrowband wave whose frequency spectrum concentrates around the central frequency, the product effectively eliminates “unwanted” frequencies and enables the analysis to be operated in a narrowband. This is the reason that the phase point detection method is applicable to AE measurement.

For wideband excitations, i.e., lead break, the phase point detection method holds promise. For active diagnosis applications where excitation signals are known narrowband waves, however, it is doubtful that such method can provide correct results. The variable x and y in Eq. (5.2) are usually set to be identical as the collected data [73], and in nature Eq.

(5.2) is changed to an autocorrelation function. In such cases, the filtering is not useful any longer since significant dispersion may be still encountered for narrowband waves when the sensor is far away from the damage. For instance, Eq. (4.55) gives the exact expression for the dispersed Gaussian pulse. The correlation physically compares a non-dispersed wave with a dispersed wave and finds the similarity of two different data sequences. As a result, the correlation method does not provide physically meaningful results, though it can yield results with tolerable error.

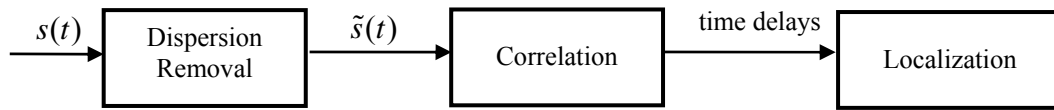


Figure 5.1 Procedure of correct correlation with dispersion removal

Notably, the linear mapping algorithm for dispersion removal developed in the last chapter may be used to make the cross-correlation method effective without the assumption. It is already shown that the dispersion can be approximately removed using the linear mapping algorithm. Regardless of propagation distance, dispersed signals can be compressed to non-dispersed forms and are ready to be used for the cross-correlation. Thus, it is advantageous to perform the dispersion removal before the cross-correlation is conducted to eliminate the ambiguity caused by the dispersion. Not only would the problem of the first threshold crossing be eliminated, but damage location determination could then be performed by using dispersive flexural waves. The combination is of importance in larger structures where, due to attenuation, only flexural waves will be able to propagate to long distances. A procedure to apply the modified correlation technique to detect excitation source is illustrated in Figure 5.1.

After the time delays have been obtained by the cross-correlation, the localization is

made through finding the solution of a group of equations, which may be expressed as

$$\|\mathbf{p} - \mathbf{r}_p\| = c_g \Delta t_p \quad (5.5)$$

where \mathbf{p} and \mathbf{r}_p are the position vector of excitation and the p^{th} sensor, respectively, $\|\cdot\|$ indicates Euclidean distance, c_g is the group velocity of the central frequency and Δt_p is the time delay calculated from the correlation. It must be noted that Eq. (5.5) is used to locate the position of the excitation source since the time delays are obtained by cross-correlating the excitation with the received signal. As there are two unknowns (the position vector of the excitation), data from at least two sensors are required. However, at least three sensors may be needed to get a unique solution. If four or more sensors exist, the solution of either Eq. (5.5) can be seen as a typical NLS problem. Gradient descent optimization or other efficient optimization methods (which will be introduced in the next section) may be used.

It must be emphasized that the implementation of the linear mapping algorithm for the dispersion removal is not practical locally inside the wireless sensor in this research. This is because the linear mapping requires intensive computational resources (memory and MCU time) as FFT and interpolations are used. To use the correlation method locally in wireless sensors, the assumption that the dispersion is not significant must be still made.

5.3 Active Damage Localization Using the Energy Decay Model and Optimization Methods

The energy decay model discussed in the last chapter indicates that the average power contained in the received signals at different locations decays inversely proportional to the square of the propagating distance. Since the dispersion has been considered in the formulation of the model, the ratio of propagating distances can be directly attained from the

received signals without removing the influence of dispersion. This distinct feature of the energy decay model outperforms other methods when significant dispersion is encountered.

To inversely locate the excitation source (or the damage), the decay ratio needs to be correctly interpreted. Basically, it is the same type of inverse problems as encountered in TDOA. The damage localization system, which typically has more sensors than required (three in the single source case), becomes over-determined with non-linear equations to be solved for the values of the unknown parameters. Least-squares regression method has earned its place as a primary tool for process modeling because of its effectiveness and completeness. With a series of measured data, least-squares regression attempts to minimize the sum of the squares of the ordinate differences between points generated by the function and corresponding points in the data. Wang [76] has proposed a damage localization technique based on least-squares regression with gradient descent optimization. The cost function is defined as:

$$F(x) = \frac{1}{2} \sum_{p=1}^P (z_p - \hat{z}_p)^2 \quad (5.6)$$

where z_p is the measured wave energy and \hat{z}_p is the modeled wave energy at the p^{th} sensor, respectively. Local minimum of the cost function can be iteratively searched by taking steps proportional to the negative of the gradient (or the approximate gradient) of the cost function.

Nevertheless, the gradient optimization may take too many iterations to converge, especially if the curvature in contrary directions is divergent. In [76], only fixed step sizes are taken to evaluate the cost function, thus hundreds of iterations may be required to reach convergence. Significant amount of computational work is required in each iteration for interpreting the gradients of the cost function. Solving the problem in such a manner in

computers is trivial, but not the case for embedded systems, e.g. wireless sensors. For instance, the memory volume is limited and the operating frequency (speed) is not even comparable with that of the computer, thus eliminating the possibility for using large matrices. Furthermore, there is usually no floating-point coprocessor in wireless sensors. Approaches which require large number of iterations will push heavy burden on the MCU in wireless sensors and will result in considerable latency and more power consumption. As the power consumption is of major concern in wireless sensors [25], solutions for either reducing computational complexity or optimizing computation schema must be sought to enable embedding SHM algorithm in wireless sensors.

In many cases the gradient optimization converges towards minimum in two different stages [77]. When the initial value is far from the solution, slower convergence may be anticipated to move the result steadily towards the solution; while at the final stages, faster convergence is desired to reduce the computation cost. Correspondingly, the convergence pattern can be distinguished in different classes, such as linear convergence, quadratic convergence and super-linear convergence [78]. To improve efficiency, other advanced methods, such as Gauss-Newton (G-N) method and Levenberg-Marquardt (L-M) method, can be used to reduce computational complexity and yield faster convergence.

The L-M method is inherently a damped version of G-N method and is widely used as an alternative in finding the minimum. It can be derived by applying Taylor series expansion to $f(x) \equiv (z_p - \hat{z}_p)$ provided that the function has continuous second partial derivatives as

$$f(x+h) = f(x) + J(x)h + O(\|h\|^2) \quad (5.7)$$

where $\|h\|$ is sufficiently small and $J(x)$ is the Jacobian matrix which contains the first

partial derivatives of the function components. Accordingly, the cost function given by Eq. (5.6) can be written as

$$F(x+h) \approx L(h) = F(x) + h^T J^T f + \frac{1}{2} h^T J^T J h \quad (5.8)$$

where the gradient matrix and the Hessian matrix of $L(h)$ can be expressed as

$$L'(h) = J^T f + J^T J h \quad (5.9)$$

$$L''(h) = J^T J \quad (5.10)$$

It can be seen that the Hessian matrix is independent of step h and symmetric. If the column of $J(x)$ are linearly independent, $L''(h)$ is also positive definite. Also, when h equals to zero, $L'(h)$ actually take the same form of $F'(x)$, which implies that $L(h)$ has a unique minimum that can be solved by

$$(J^T J + \mu \mathbf{I})h = -J^T f \quad (5.11)$$

where \mathbf{I} is an identity matrix, μ are nonnegative scalars used as the damping parameters in the L-M method, and h can be used for optimal step sizes.

The damping parameters μ introduced here influence both the direction and the size of the step, and are updated in each iteration by measuring gain ratio which takes the form of

$$g = \frac{F(x) - F(x+h)}{L(0) - L(h)} \quad (5.12)$$

If g is large, it indicates that $L(h)$ is in good agreement with $F(x+h)$. Thus the damping parameters can be decreased for the next iteration to increase step size for faster convergence. Effectively, the algorithm is equivalent to classical Gaussian-Newton method. If g is small, it denotes that $L(h)$ is a poor approximation. The damping parameters must be increased to get closer to the steepest descent direction and reduce step size. In fact, step

sizes are differed in the beginning stages and the final stages to obtain optimal results and quadratic convergence can be achieved while approaching the solution [78]. The convergence criterion can be given by comparing $F'(x)$ with a preset threshold and checking the gradual change of relative step size. The procedure of the L-M algorithm can be summarized as the following,

Initialization:

Initialize damage positions $\{\mathbf{p}\}$

Initialize damage reflection factors α

Initialize μ

Repeat until convergence

Calculate g

Calculate $L'(0)$ and $L''(h)$

Update $\{\mathbf{p}\}$ and α

Update μ

5.4 Improvement on the Localization Methods: Matrix solutions

Both localization methods described in Section 5.2 and 5.3 are reduced to NLS problems. Although the Levenberg-Marquardt method can significantly improve the speed of the optimization process, it is still not practical to be entirely embedded into wireless sensor due to the iterative evaluation. To enable a fully embedded SHM system with wireless sensors, the NLS problem must be simplified for better computational efficiency. In this section, the localization with both methods is converted into linear least squares (LLS) problem, which can be solved by singular value decomposition and pseudo-inverse matrix.

5.4.1 Matrix solution for the correlation method

Suppose the position vector of the excitation and three sensors $p=i, j, k$ are represented by $\boldsymbol{\rho} = (x, y)^T$, $\mathbf{r}_i = (x_i, y_i)^T$, $\mathbf{r}_j = (x_j, y_j)^T$ and $\mathbf{r}_k = (x_k, y_k)^T$, respectively.

Substituting them into Eq. (5.5) yields

$$\begin{cases} (x-x_i)^2 + (y-y_i)^2 = (c_g \Delta t_i)^2 \\ (x-x_j)^2 + (y-y_j)^2 = (c_g \Delta t_j)^2 \\ (x-x_k)^2 + (y-y_k)^2 = (c_g \Delta t_k)^2 \end{cases} \quad (5.13)$$

Expanding Eq. (5.13) and subtracting each other to eliminate the terms x^2 , y^2 , and t_d give

$$\begin{cases} 2x(x_i - x_j) + 2y(y_i - y_j) = (x_i^2 + y_i^2) - (x_j^2 + y_j^2) - c_g^2 (\Delta t_i^2 - \Delta t_j^2) \\ 2x(x_i - x_k) + 2y(y_i - y_k) = (x_i^2 + y_i^2) - (x_k^2 + y_k^2) - c_g^2 (\Delta t_i^2 - \Delta t_k^2) \\ 2x(x_j - x_k) + 2y(y_j - y_k) = (x_j^2 + y_j^2) - (x_k^2 + y_k^2) - c_g^2 (\Delta t_j^2 - \Delta t_k^2) \end{cases} \quad (5.14)$$

Discarding one of the linearly dependent equations, the rest of the two equations can be formed

$$\mathbf{A}\boldsymbol{\rho} = \mathbf{b} \quad (5.15)$$

where $\mathbf{A} = \begin{bmatrix} x_i - x_j & y_i - y_j \\ x_i - x_k & y_i - y_k \end{bmatrix}$ and $\mathbf{b} = \frac{1}{2} \begin{bmatrix} (x_i^2 + y_i^2) - (x_j^2 + y_j^2) - c_g^2 (\Delta t_i^2 - \Delta t_j^2) \\ (x_i^2 + y_i^2) - (x_k^2 + y_k^2) - c_g^2 (\Delta t_i^2 - \Delta t_k^2) \end{bmatrix}$. It is clear

that the NLS problem has been converted into a LS problem. For P sensors, the coefficient matrix \mathbf{A} have dimension of $(P-1) \times 2$ and \mathbf{b} is a $(P-1) \times 1$ vector. When the number of sensor exceeds three, the problem becomes an over-determined LS problem. The solution of the position vector can be immediately obtained by methods in linear algebra.

5.4.2 Matrix solution for the energy decay model

For the correlation method, since the cost function is relatively simple, performance

gain may not be significant. However, for the method based on the energy decay model, the Jacobian matrices have fairly complex forms and the evaluation of such matrices in each iteration is very time-consuming in Section 5.3. Therefore, it is more desirable to obtain a matrix form solution. Inspired from the last Section, geometry information is also introduced to simplify the problem. As such, Eq. (4.117) gives

$$\|\mathbf{p} - \mathbf{r}_p\|^2 = \frac{\gamma_p^2 P_{s0}}{z_p - \sigma_n^2} \quad (5.16)$$

If the sensor gains γ_p are fixed for all sensors, distance ratios can be defined as

$$\frac{\|\mathbf{p} - \mathbf{r}_i\|^2}{\|\mathbf{p} - \mathbf{r}_j\|^2} = \kappa_{ij}^2 \quad (5.17)$$

where $\mathbf{r}_i = (x_i, y_i)$ and $\mathbf{r}_j = (x_j, y_j)$ are the position vectors of arbitrary two sensors, and

$\kappa_{ij}^2 = \frac{z_j - \sigma_n^2}{z_i - \sigma_n^2}$ is defined as energy ratio. It must be noted that γ_p is now refined as the

generalized sensor gain which also includes the reflection factor. Using scattered wave information from damage to localization, the assumption for “constant γ_p ” implies that the damage scatters excitation wave omni-directionally with equal intensity and the physical gain of individual sensor has been pre-calibrated. One of the advantages of using the energy ratio is that γ_p is removed in the formulation and not of concern any more.

For $\kappa_{ij}^2 \neq 1$, Eq. (5.17) can be simplified as

$$(x - x_{ij})^2 + (y - y_{ij})^2 = r_{ij}^2 \quad (5.18)$$

where $(x_{ij}, y_{ij}) = \left(\frac{x_i - \kappa_{ij}^2 x_j}{1 - \kappa_{ij}^2}, \frac{y_i - \kappa_{ij}^2 y_j}{1 - \kappa_{ij}^2} \right)$ and $r_{ij} = \frac{\kappa_{ij} \sqrt{(x_i - x_j)^2 + (y_i - y_j)^2}}{|1 - \kappa_{ij}^2|}$. Eq. (5.18)

indicates that the excitation source should be potentially located on a circle where the center is (x_{ij}, y_{ij}) and the radius is r_{ij} .

For a special case $\kappa_{ij}^2 = 1$ where the damage lies on the midline of the connection between two sensors, the location can be given by

$$2(x_i - x_j)x + 2(y_i - y_j)y = (x_j^2 + y_j^2) - (x_i^2 + y_i^2) \quad (5.19)$$

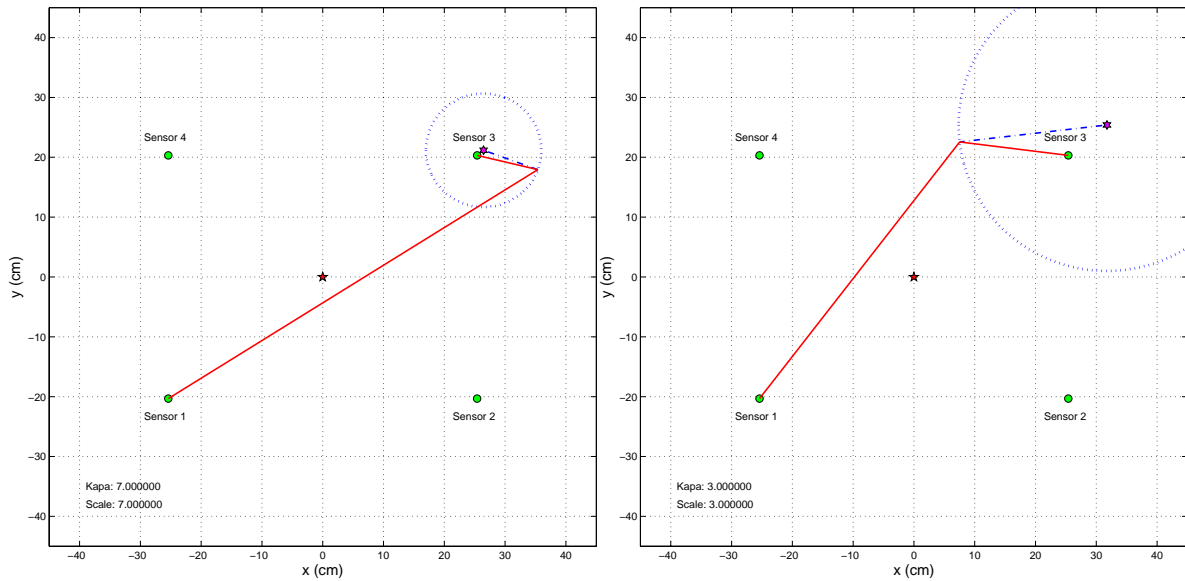


Figure 5.2 The circle and its center for potential damage locations with given $\kappa = 7$ and 3

Figure 5.2 depicts such circles and their centers with respect to the geometry of sensors. The energy ratio is set to 7 and 3 in the example. As the energy ratio decreases, the radius of the circle decreases. The center of the circle moves away from sensors, yet staying on the line which crosses both sensors. Each pair of sensors yields a circle and obviously at least three sensors may yield a unique intersection. In other words, for P sensors, C_p^2 pairs of energy ratios give the location of the damage by finding the intersection. However, the equations are still non-linear and an optimization method must be used through iteratively evaluating cost functions as it occurs in a typical over-determined system.

Comparing Eq. (5.13) and Eq. (5.18), it can be seen that both of these equations share a similar form. The only difference is the notation and the RHS part. By using a similar approach in the Section 5.4.1, the NLS problem can also be converted into a LLS problem,

$$\mathbf{A}\boldsymbol{\rho} = \mathbf{b} \quad (5.20)$$

where $\mathbf{A} = \begin{bmatrix} x_{ij} - x_{ik} & y_{ij} - y_{ik} \\ x_{ij} - x_{jk} & y_{ij} - y_{jk} \end{bmatrix}$ and $\mathbf{b} = \frac{1}{2} \begin{bmatrix} (x_{ij}^2 + y_{ij}^2) - (x_{ik}^2 + y_{ik}^2) - (r_{ij}^2 - r_{ik}^2) \\ (x_{ij}^2 + y_{jk}^2) - (x_{ik}^2 + y_{jk}^2) - (r_{ij}^2 - r_{jk}^2) \end{bmatrix}$.

5.4.3 Singular value decomposition (SVD)

SVD is the method of choice for solving most LLS problems and has been widely applied in signal processing to solve over-determined linear algebraic equations. SVD can be found in many literature [77, 79]. For the sake of clarity, a procedure how pseudo-inverse of a matrix is used to find the best approximation is briefly described.

SVD can be described by a theorem based on the linear algebra: Any $M \times N$ matrix \mathbf{A} may be written as the product of any $M \times N$ column-orthogonal matrix \mathbf{U} whose column are eigenvectors of $\mathbf{A}\mathbf{A}^T$, an $N \times N$ diagonal matrix \mathbf{W} with non-negative elements (the singular values), and the transpose of an $N \times N$ orthogonal matrix \mathbf{V} whose rows are eigenvectors of $\mathbf{A}^T\mathbf{A}$ [77]. Namely,

$$\mathbf{A} = \mathbf{U} \cdot [\text{diag}[\omega_j]] \cdot \mathbf{V}^T \quad (5.21)$$

where $\mathbf{U}^T\mathbf{U} = \mathbf{V}^T\mathbf{V} = \mathbf{I}$, $j = 1, \dots, N$. Thus, the pseudo-inverse of \mathbf{A} is,

$$\mathbf{A}^+ = \mathbf{V} \cdot [\text{diag}[\frac{1}{\omega_j}]] \cdot \mathbf{U}^T \quad (5.22)$$

where $\frac{1}{\omega_j}$ is replaced by zero if $\omega_j = 0$ (singularity).

For homogeneous linear equations $\mathbf{A}\mathbf{x} = 0$, the solution can be immediately obtained

by SVD and any column of \mathbf{V} whose corresponding ω_j is zero yields a solution; For inhomogeneous linear equations, $\mathbf{Ax} = \mathbf{b}$, the solution can be obtained by using the pseudo-inverse matrix as

$$\mathbf{x} = \mathbf{A}^+ \mathbf{b} = \mathbf{V} \cdot [\text{diag}[\frac{1}{\omega_j}]] \cdot \mathbf{U}^T \cdot \mathbf{b} \quad (5.23)$$

Eq. (5.23) actually gives the solution directly. In the sense of the least-squares error, it is the best linear approximation to the actual solution. In many cases, the coefficient matrix \mathbf{A} can be decomposed just once, and then the decomposition can be used many times. Specifically for Eq. (5.15), since the locations of the sensors are essentially known, the pseudo-inverse can be pre-calculated and integrated in the program, making the damage location determination very efficient. For instance, if four sensors are located in the vertices of a 0.3m×0.3m square area, the pseudo-inverse matrix is given as

$$\mathbf{A}^+ = \begin{bmatrix} -1.1111 & -0.5556 & 0.5556 \\ 0.5556 & -0.5556 & -1.1111 \end{bmatrix} \quad (5.24)$$

5.5 Results from Simulated Data

In this section, the proposed active damage localization algorithms are applied to simulation data which assumes that experiments are conducted on an aluminum plate (Al-6061) with the material properties previously listed in Table 4.1. A finite difference algorithm based on Mindlin plate theory is used to synthesize the diagnostic waves in a plate [80]. With the origin of the coordinate system set at the center of the plate, a 600×600 finite difference mesh with uniform square grid space $\Delta x = \Delta y = 2.54\text{mm}$ is superimposed on the plate region. One damage is located at (20, 10) cm by setting the bending stiffness at the point damage 16 times larger than the undamaged area. In addition, four sensors are

modeled, locating at (-30,-30) cm, (30, -30) cm, (30, 30) cm and (-30, 30) cm. The central frequency of the excitation signal, a five-peaked wave, is set as 50 kHz which is less than the first cut-off frequency such that only the lowest anti-symmetric wave A_0 exists. The group velocity of the A_0 mode is calculated by the higher-order theory and equals to 2107m/s. Since the plate is large enough to ensure that no wave is reflected from the boundary during the time span of data record. White Gaussian noise is added to the data afterward to simulate noises encountered in practice.

Two sets of data are calculated with different standard variances of $\sigma = 0.15$ and $\sigma = 0.95$, respectively, shown in Figure 5.3. It may be seen that the waves are still packed in the time domain, but the slight dispersion effect can still be observed, especially at sensor 1 and sensor 4 which are far away from the damage. As the noise intensity increases, the signal at sensor 4 becomes vague and is hard to identify the time of arrival due to the attenuation and the noise.

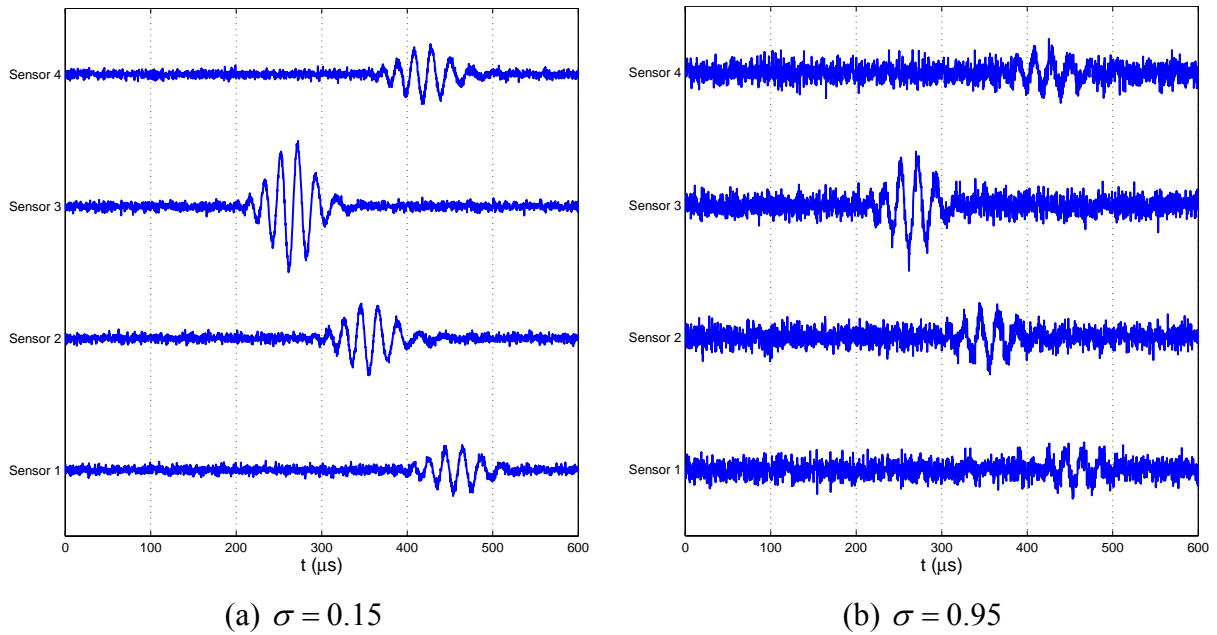


Figure 5.3 Simulated scattered wave by finite difference method with AWGN added

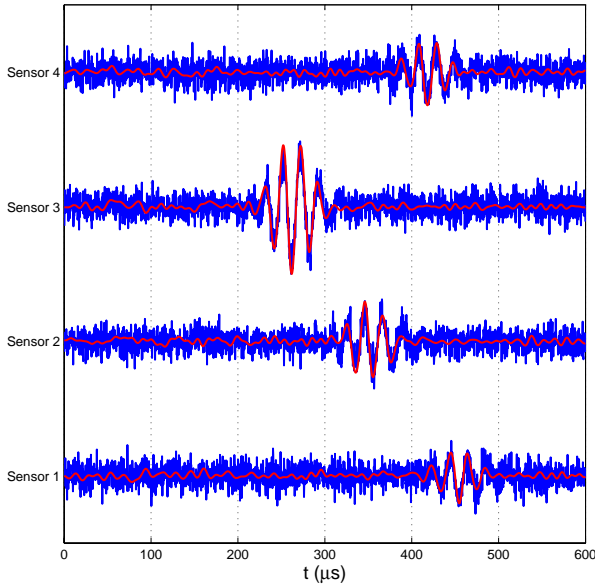


Figure 5.4 Comparison between contaminated signal and compressed signal

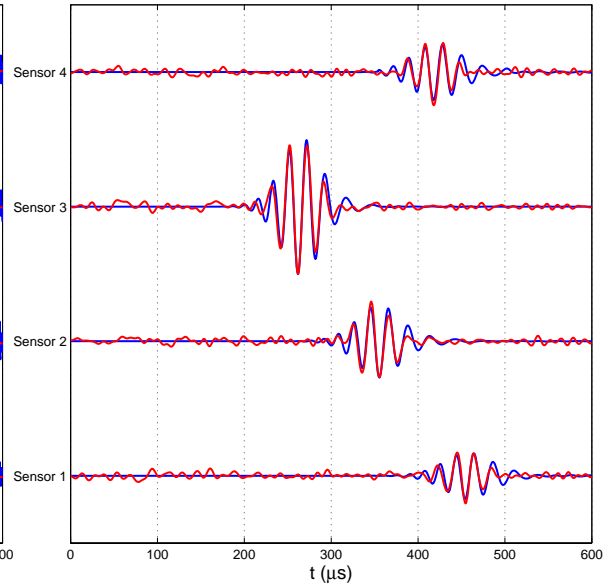


Figure 5.5 Comparison between uncontaminated signal and compressed signal

Firstly, the modified cross-correlation method was applied to the simulated sensor signals. The linear mapping algorithm for dispersion removal was initially applied to both sensor data to compress the dispersed and contaminated signals. To better illustrate the result of the dispersion removal, the compressed signals are compared with the contaminated signals with $\sigma = 0.95$ and the uncontaminated signals, and plotted in Figure 5.4 and Figure 5.5 respectively. Compared with the contaminated signals, the original diagnostic signal (five-peaked wave) is almost perfectly restored after the dispersion removal. Noises are almost completely removed because the linear mapping algorithm also acts as a band-pass filter. Examining the signal at sensor 1 which is the farthest away from the damage and subjects to low SNR, the time of arrival is more easily interpreted. Compared with the uncontaminated signal, the concentration of the dispersed signals can be clearly seen. That is, the compressed signals have better similarity with the original excitation over the dispersed ones. In theory, the accuracy of the correlation method applied on the compressed signals

should be better than that over dispersed signal.

It has been mentioned previously that fully embedding the dispersion removal in the miniature wireless sensor is not practical since it requires FFT and interpolations on a large amount of data. In practice, if the dispersion is not significant such as that in this simulation study, the original cross-correlation method can still provide reasonable results. To enable the practicability that the cross-correlation can be embedded into wireless sensors to locally estimate the damage location in this research, the assumption of insignificant dispersion is still made. To validate the assumption, the cross-correlation method is applied on both the compressed signal and the contaminated signal to obtain the damage location.

Figure 5.6 displays and compares the cross-correlation function of the contaminated signals ($\sigma = 0.95$, solid lines) and the compressed signals (dash lines). The signals from all sensors are cross-correlated with a pre-set sequence to present original excitation. Since only the time differences are of interest, the use of the pre-built sequence has the same effect as the use of the real excitation signal. Notably, such replacement can greatly reduce the power consumption of wireless sensor in field applications since no extra communication is required to transmit the excitation signal. The position of the actuator is no longer of importance as long as the minimum time difference calculated is larger than the propagating time required for the wave of direct arrival. The time delays corresponding to the peak of the cross-correlated functions exactly indicate the time differences. In the figure, horizontal lines mark the peaks and the corresponding time delays. It can be found that the time delays at each sensor are almost identical for both cases whether it is from the contaminated signals or the compressed signals. This confirms the assumption that the direct use of the contaminated signals can still give reasonable results.

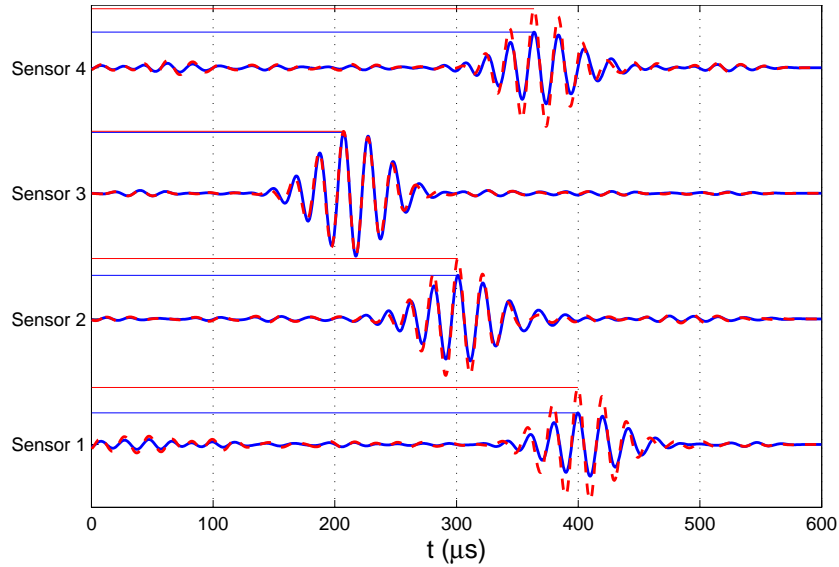


Figure 5.6 The cross-correlated sequences of contaminated signals and compressed signals

It is still of interest to compare the accuracy for both cases. The time differences are further used to localize the damage by using Eq. (5.15) and Eq. (5.24). Besides using the SVD method, L-M method is also used to calculate results of equations, which have similar forms of Eq. (5.13), for comparison purpose. The tolerated error was set to 10^{-10} for the L-M method, while a standard routine SVD() in Matlab was used. Figure 5.7 graphically illustrates the solution of the cross-correlation method using NLS. As an inverse problem, the position vector of the damage and t_d in Eq. (5.13) was found simultaneously after convergence at three iterations. The circles with different colors in the figure indicate the propagating distances, or equivalently, the propagating times. Theoretically, the damage can be found at the common intersection of all these circles. The figure also marks the modeled damage location. However, it is covered by the six-pointed star symbol which is used to show the calculated damage location.

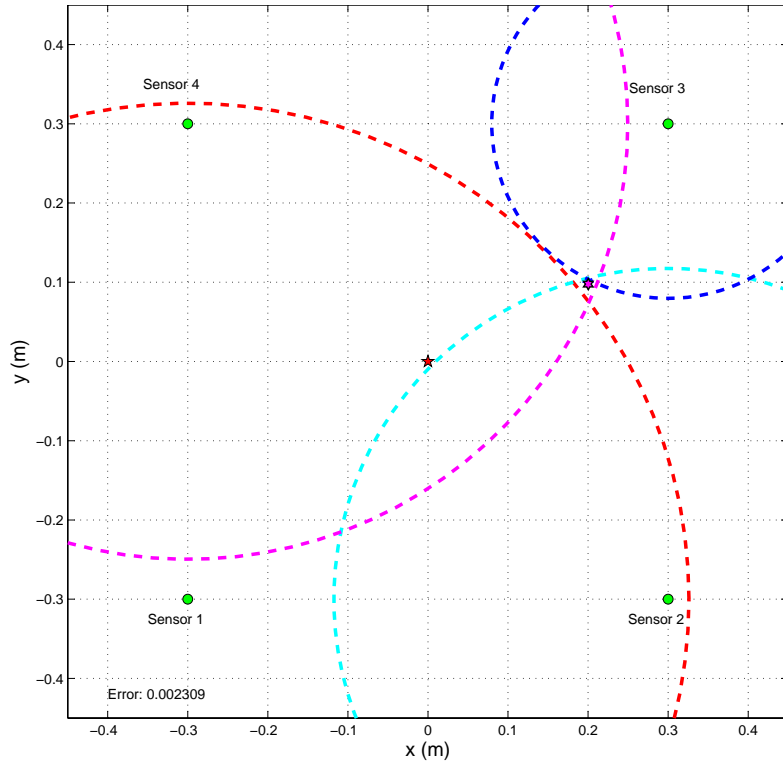


Figure 5.7 Damage localization using cross-correlation and NLS

Table 5.1 gives the observations from different cases. It is interesting to note that the results from the L-M method have higher accuracy than the SVD solution under the same circumstance. This can be attributed to the smaller tolerated error used in the L-M method. From the standpoint of dispersion removal, it can be seen that the results after dispersion removal applied is slightly better than those without dispersion removal. However, the discrepancies are not very significant, thus confirming that the cross-correlation method can be directly applied in wireless sensors. Also, it can be seen that the L-M method reaches convergence very quickly due to the simplicity of the cost function. To be precise, the L-M method takes average 0.04 seconds, whereas SVD gets results almost instantly in PC. However, this does not mean that SVD has no merit over the L-M method while running inside wireless sensors. Finally, the simulation shows that the cross-correlation method is very stable. Damage can be localized even with signals containing moderate noises.

Table 5.1 Comparison of the solution of damage localization using cross-correlation

#	Noise STD σ	Dispersion Removal Applied?	Solution method for the cross-correlation				
			SVD		L-M		
			Position (cm)	Offset (cm)	Iteration Numbers	Position (cm)	Offset (cm)
1	0.15	No	(20.73,9.72)	0.78	3	(20.03,9.77)	0.23
2		Yes	(20.70,9.74)	0.74	3	(20.00,9.80)	0.20
3	0.95	No	(20.71,9.71)	0.77	3	(20.10,9.76)	0.24
4		Yes	(20.70,9.69)	0.76	3	(20.30,9.78)	0.22

Secondly, the methods based on the energy decay model are applied to the simulated sensor signals for damage localization. The L-M method and the gradient descent method are used and compared in PC and the localization errors are presented in Figure 5.8. The initial position vectors are both set to (-20.00, -15.00) cm and the initial reflection factors are set to 0.2. The gradient method takes 480 iterations to converge with the estimated damage location at (20.12,10.68) cm in about 55 seconds (programmed in Matlab), while the L-M method only requires 53 iterations with 217 times of function evaluation and completes within 16 seconds with the estimated damage location at (20.78, 10.49) cm. The result from the gradient method is deviated from the targeted damage location by 0.89 cm; while the result from the L-M method is deviated by 0.92 cm.

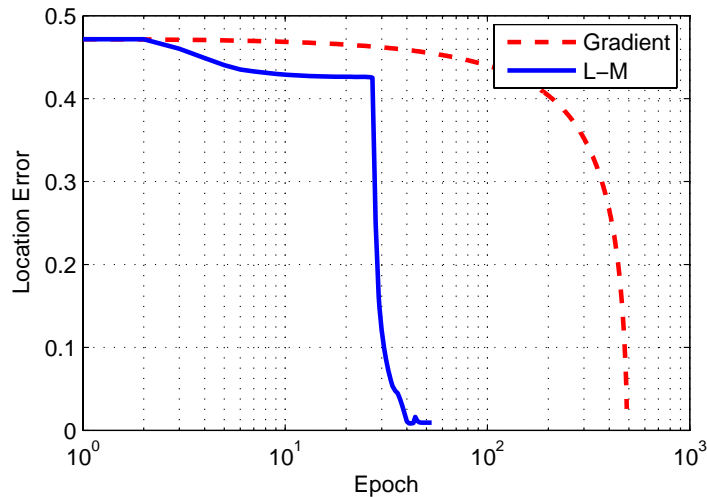


Figure 5.8 Comparison of localization error by using L-M and gradient descent

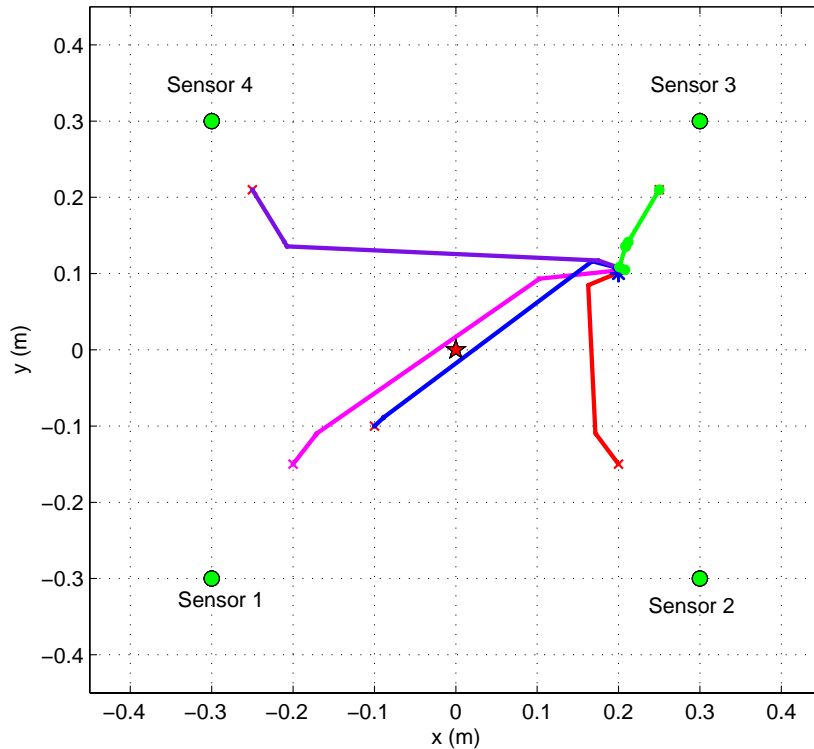


Figure 5.9 Searching paths with different initial guess positions for L-M method

Comparing the deviation with the geometry of the measuring area, the errors are very small and both methods are acceptable in practical applications. From the figure, it can be seen that the L-M method requires fewer number of iterations and time than those required by the gradient method. Both simulated sensor signals with different values for initial guesses are used for both the gradient method and the L-M method. From these experiments, it is shown that the L-M method is generally three times faster than the gradient method. This is due to both the step size and the direction are “adaptively” chosen in each iteration with the help of the damping parameters. Moreover, the L-M method also exhibits better stability than the gradient method. As the SNR ratio decreases, the gradient method may fail to converge because the fixed step sizes used in the gradient method must be manually chosen to adapt varying conditions. However, the L-M method still can successfully find reasonable estimated locations even in extreme cases. Figure 5.9 shows an example for searching paths

with different initial guess positions. The L-M method appears to have more robust performance than the gradient method.

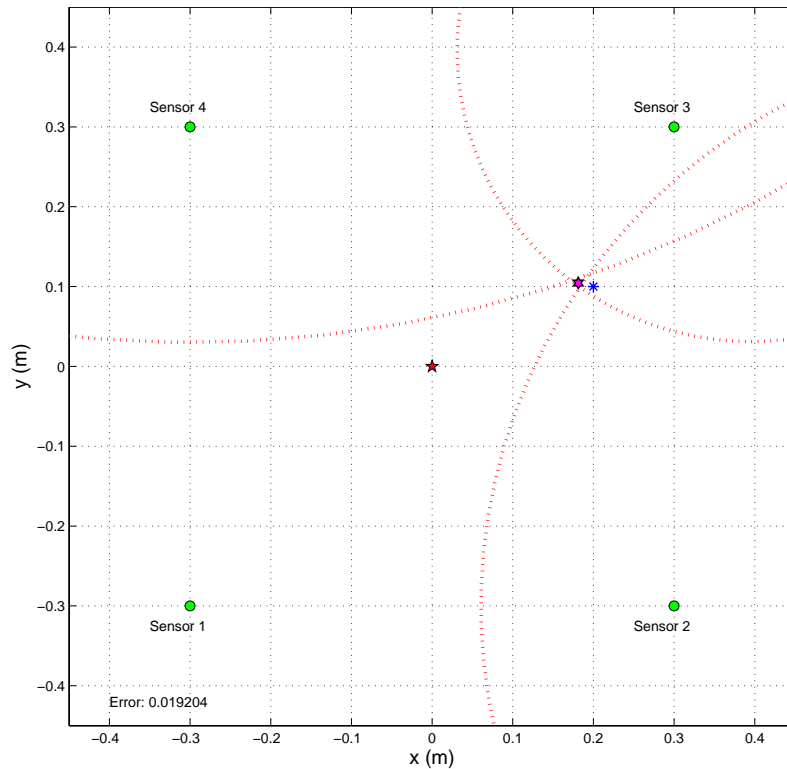


Figure 5.10 Damage localization through SVD

Nevertheless, the procedures based on the L-M method are still very time-consuming. As the MCUs on wireless sensors are far slower than the CPU in PC, the solution for the matrix form is carried out. Figure 5.10 illustrates the damage location found through the SVD method. It must be noted that in Eq. (5.20), for some situations the vector \mathbf{b} becomes all zeros and Eq. (5.20) actually becomes a homogenous problem. Additionally, it may not be worthy in performing SVD in wireless sensors considering the time cost and program size. In these situations, Eq. (5.18) provides a concise form for a simple NLS problem.

Finally, the correlation method and the energy based method are compared. Both methods yield acceptable results and tolerate noise well according to the simulated data. Although theoretically the correlation method may fail to give correct results for long

distance wave propagation, practical applications can still use it. When both methods are executed in PC, there is virtually no major difference. However, when computational cost is of concern, care must be taken to check each method. For the matrix solution, both methods require calculations of specific ratios, either time difference ratios or energy ratios. Assuming the total length of a individual data set is N , there are $N(N-1)/2$ times multiplication and $N(N-1)/2$ summation in total for the evaluation of the cross-correlation function; while there are only N times multiplication and N times summation for obtaining the energy value. For the wireless sensors developed in this research, as well as other prototypes with power concern, MCU is only 8-bit and no floating-point processor is included. Floating type (or double type) mathematic operations are made in software approach. It is not unusual that a single summation or subtraction needs tens of MCU cycles and a multiplication needs hundreds or even thousands of MCU cycles. For example, a simple experiment reveals that a 3000 times of multiplication of 16-bits integer takes about 1.42 second on a 4MHz Atmel MCU. Although this number is not a strict measurement since the time or duration may vary under different circumstances, such as the program, the compiler, and its setting, it is still a good base for estimation. For the cross-correlation, it will need at least 2130 seconds (or 35 minutes) to complete, which may be unrealistic. From this point, the energy decay model outperforms the correlation method. On the other hand, SVD for the correlation method can be pre-calculated and coded into programs, but SVD operations for the energy decay model must be calculated every time. Generally speaking, the proposed method based on the energy decay model is a promising method for active damage localization, though consideration must be taken according to specific applications to choose the proper algorithm.

5.6 Summary

In this chapter, two methods for active damage localization are proposed, presented and compared, that is, the correlation method and the energy decay based method. Since the correlation method essentially compares the similarity of two signals, the method may theoretically fail to correctly indicate time differences when severe dispersion exists. Dispersion removal developed in the previous chapter is proposed to recompress signals before applying the correlation method. In contrast, the energy decay based method does not require such process since the dispersion relation has been already considered in the formulation of the model. Regarding the computational performance of the two methods, the latter is more desirable.

Also, to enhance the computational efficiency, further simplifications by introducing geometry information of sensor locations are made for both methods. It has been shown that NLS problems can be transformed to LLS problems and SVD and pseudo-inverse matrix can be used to quickly obtain results. Especially for the latter method, which has more complex form of “cost functions”, the simplification may greatly reduce the computation cost, and may hold promise in the application to wireless sensors.

Comparisons are made on simulated data sets with various noise intensities. Note that the simulated data are chosen intentionally to only have slightly dispersion to check the results with and without dispersion removal for the correlation method. Since the dispersion removal requires FFT and interpolation, it is not desirable to be implemented in the newly developed wireless sensor at the present time. Interpretation from the simulated data has proven that direct application of the correlation method can still yield reasonable results for slightly dispersed waves.

Furthermore, it shows that two methods can yield results with similar accuracy regardless of noise. However, the noise can be directly removed by the correlation method, while the energy decay model must use the known STD of noise to remove the influence of noise. This may affect the accuracy of the energy based method since the measurement of the STD of the noise must be taken in advance and may not faithfully present the noise contained in the signals for damage localization.

6 Experimental Validation of Distributed Active Damage Localization within Wireless Sensor Network

As the early part of this research focuses on providing a hardware platform of high speed wireless sensor to reduce the *acquisition consumption*, the *communication consumption* and the *computation consumption* are implicitly discussed in the last two chapters by investigating active damage localization algorithms. In this chapter, experimental validation of the developed wireless sensors and algorithms has been conducted. A SHMS performed in the laboratory with three-tier wireless sensor network (WSN) for active damage localization on plate-like structures is constructed. Following the detailed description on power efficiency of the proposed WSN, experimental results are provided to show the promise of the proposed approach.

6.1 A Three-Tier Network for Active Damage Localization

A three-tier wireless sensor network is proposed to be used for active damage localization. Namely, the entire sensor network is divided into three tiers: slave sensor nodes, master sensor nodes, and base station. Several slave nodes, with piezoelectric sensors connected, and a master node form a group to cover certain geometrical areas. Many such groups and a base station constitute a large scale sensor network, as shown in Figure 6.1.

Each sensor node has a local ID (identification) and a group ID, which are further combined to form a unique address for communication. To minimize power consumption and avoid congestion which may occur on wireless channels, slave sensor nodes operate with reduced radio radiation power that is just enough to reach their corresponding master sensor node. In contrast, the master sensor nodes work with full radio power which must satisfy a

critical prerequisite that a master sensor node can communicate with at least one adjacent master sensor node. Functioning as the coordinators for the group, the master sensor nodes also relay the data transmitted in the network. The base station, which has a special address, is in charge of all master nodes and reach, send or request data to/from individual group through direct or relayed communication links.

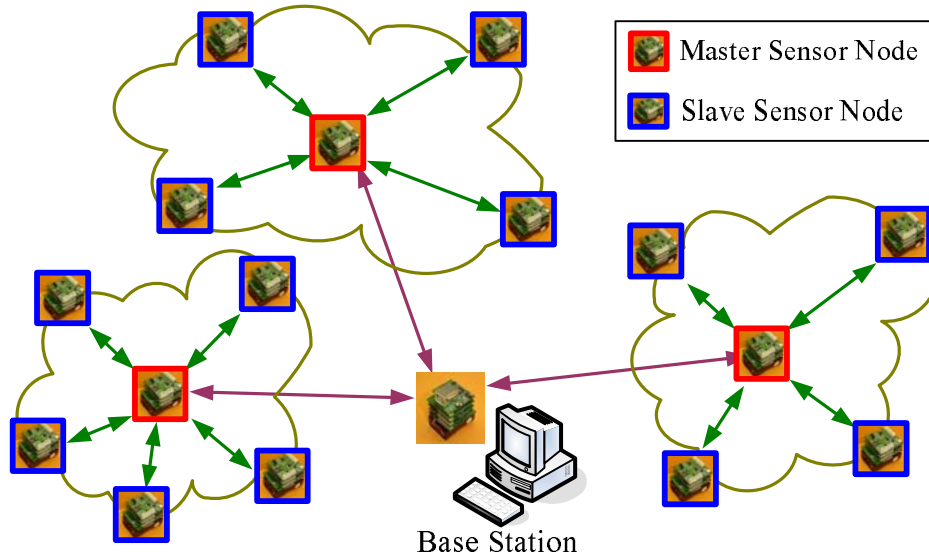


Figure 6.1 Illustration of the three-tier sensor network for active diagnosis

All sensor nodes stay in sleeping mode with the quiescent current consumption at μA level. Periodically, the master node in a group wakes up to monitor the wireless channel and inquiry incoming message from the base station. If there is a package addressed to it or a command to activate its group, the master node will interpret the package or inform and activate all slave nodes; otherwise, the master node will return back to sleeping mode. Slave nodes work in similar manner except that they only inquiry the incoming messages from their master nodes. Using such procedures, the overall power consumption can be dynamically manageable. It must be noted that many other optimizations on network organization and routing are investigated in-depth to improve power efficiency [81-83]. However, such topics

are beyond of the scope in this dissertation since the embedded algorithms are focused.

A typical structural evaluation is initiated from the base station by sending commands to the master node in the target group. After waking up all the slave nodes, the master node then broadcasts commands for sensing to all slave nodes and simultaneously starts the actuation. The actuation may be directly made by the master node by using a transduction module for piezoelectric driving, or may be made by an external device that is triggered by the master node. In the first case, external power supplies, i.e., power lines, may be required for the master node. Concurrently, the slave sensors immediately take measurements after the reception of the sensing command and record the data within themselves. Since all slave sensors can receive the broadcasted sensing command simultaneously and parse it in the same manner, the recognition of the sensing command and the sampling should start at the same time. Effectively, the relative synchronization errors among sensor nodes are confined within one MCU clock. Considering the group velocity of the excitation signal, the error is very small, thus can be neglected. After the transient duration of actuation/sensing, the slave nodes report their status to the master node in case that one node may fail to correctly receive the sensing command. If all slave nodes report positive, the master node will consider the evaluation procedure succeed; otherwise, the above procedure may be repeated. Upon successful measurement, the recorded data are either processed locally in slave nodes or transmitted to the base station for further analysis.

The distinct advantage of the proposed three-tier hierarchy can be explained by examining the communication consumption. First of all, the transmission range requirement of slave nodes is significantly reduced. Slave nodes require less power to transmit out given amount of data. Since majority of WSN is composed of slave nodes, this extensively reduces

the energy consumption of the entire WSN. Secondly, the radio interference between groups may be reduced as well. Since frequency channel is an exclusive resource, radio protocols, such as the IEEE 802.15.4 which is used for WSN, are usually preemptive based on CSMA/CA (Carrier Sense Multiple Access with Collision Avoidance) technique. CSMA/CA acts to prevent collisions before they happen. If a node has data to be sent, it listens to the channel to make sure that there is no transmission in progress (or listen before talk). If the channel is idle, then data is sent; If the channel is not idle, the node waits a random amount of time, and then checks again to see if the channel is idle. This amount of time is called the back-off factor and is counted down. If the channel is idle when the back-off counter reaches zero, the node transmits data. If the channel is not idle when the back-off counter reaches zero, the back-off factor is set again and the process is repeated. CSMA/CA improves the energy efficiency by avoiding overhearing among neighboring nodes. However, when WSN increases to large scale, such listen-talk procedure may repeat several times and evenly occur in all nodes, the efficiency of the communication may degrade considerably when a large amount of sensors exist. 50-80% of energy may be wasted in overcoming packet collisions [84]. By reducing the transmission range of slave nodes, the possibility of collision can be minimized, thus the proposed three-tier hierarchy is more applicable than that described in [5].

Most importantly, local processing and data fusion performed inside groups defined under the three-tier hierarchy further reduce power consumption by providing tradeoffs in communication versus computation energy. The improvement of energy efficiency can be best explained through an example. Including the overhead of communication protocol, processing time and acknowledge latency, the communication rate is about 2 kilobyte per

second which may be even lower when the radio channel is busy. Assuming that 3100 points of raw time-history record will be collected in a slave sensor node and giving that each data point is represented by a 10-bit integer generated by the ADC, the length of the data is in total 31000 bits. Without local processing, the whole data set is required to be transmitted out to the base station, and the total energy consumption only includes the communication consumption. Since it at least requires 2 second to keep sensor node in active and the average current draw at transmission mode, in which MCU, SRAM, FPGA and radio module are in active mode, is 38mA given in the previous chapter, the total amount of energy consumed is $E_t = V \times I \times t = 3.3V \times 38mA \times 2s = 250.8mJ$. In comparison, the total energy consumption is the sum of the computation consumption and the communication consumption. However, since only one package is required to be transmitted, the entire duration for radio module in active mode may be only around 1 ms, thus the communication consumption can nearly be neglected comparing to E_t . Particularly, computation of the sum of the square of the 3100 points data can be done in the wireless sensor in about 1.24 second with the 4 MHz clock. As the current draw in computation mode is only 17 mA, the consumed energy is $E_c = 3.3V \times 17mA \times 1.24s = 69.56mJ$. The improvement of power efficiency is evident in this experiment that almost 70% energy can be saved. Nevertheless, this example only gives a rough estimation of a single group of wireless sensor nodes. When sensor network expands to be large scale, in which complex network topology is involved, the improvement may be more substantial since additional energy costs for the interference mentioned in the last paragraph.

6.2 Experimental Setup

The proposed three-tier WSN and the active damage localization algorithms are experimentally verified on an aluminum plate which are similar to that applied in the simulation study as shown in Figure 6.2 and Figure 6.3.

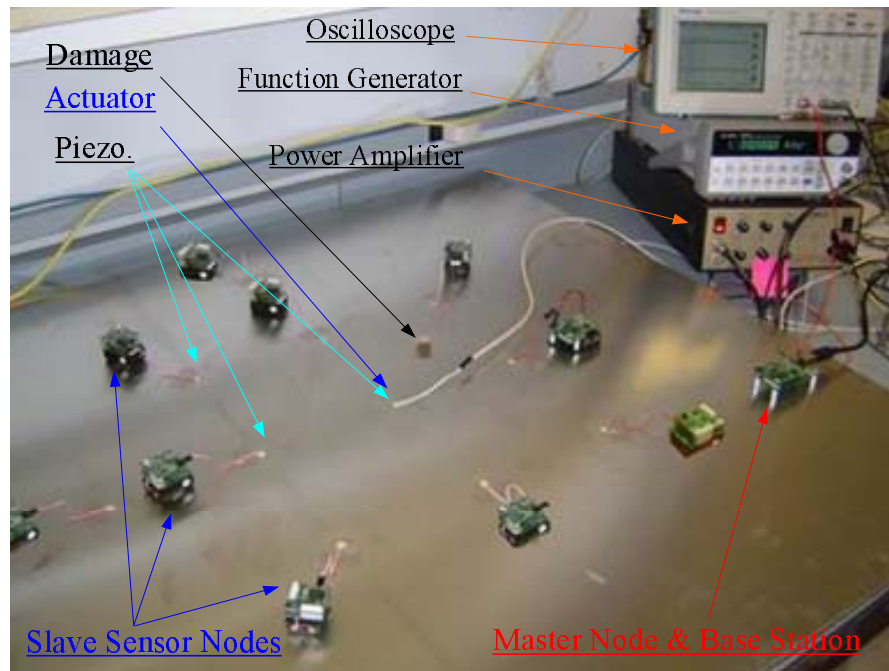


Figure 6.2 Experimental setup for active damage localization

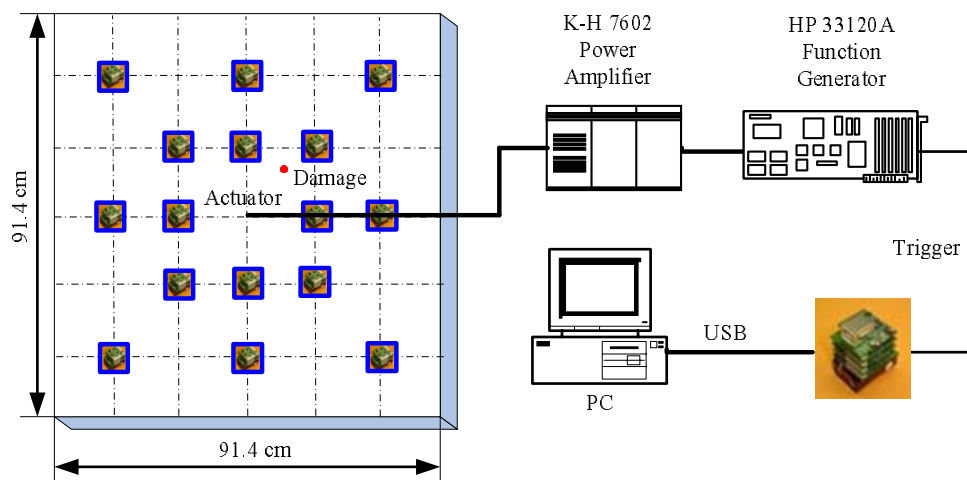


Figure 6.3 Schematic for the experimental setup

Two aluminum plates Al-6061 with dimension of 91.44 cm×91.44 cm (36 inch×36 inch), were prepared for the experiments. The thickness of the plate is 1.588 mm (1/16 inch) and 3.175 mm (1/8 inch) respectively. The thin plate is evenly partitioned into many square areas with mesh size of 15.24 cm (6 inch). Piezoelectric discs (PKI502) are bonded at all intersections on the top side of the plate. Specially, another piezoelectric disc is bonded at the bottom side of the plate at the center point, opposite to the one on the top side. These two are used as actuators to excite waves. By changing the polarity of voltages applied on the actuators, flexural waves and extensional waves can be excited alternatively. All other piezoelectric discs are to be connected to a wireless sensor to compose a slave sensor node. The diameter and the thickness of piezoelectric discs are 7.0 mm and 0.4 mm, respectively. Similarly, the thick plate is also arranged with piezoelectric discs bonded. Only four sensors are available in the thick plate, forming a 25.4 cm × 20.32 cm rectangular region around the central points of the plate.

To avoid making permanent scathe to the plate, rare-earth magnet stones are used to imitate damage on the plate. By placing two circular rare-earth magnet stones on opposite sides of the plate with antipodes, a damage area is imitated by the large magnetic force attracting the plate. The diameter of the magnet stones is 1.2 cm that is much smaller than the measurement region, thus can be considered as a point damage.

The experimental setup also includes a HP 33120A function generator, a KH-7602 power amplifier, a Tektronix TDS 210 digital oscilloscope, a desktop PC, and several wireless sensors. Beside the slave sensor nodes, a wireless sensor with an interface module is connected to the PC through USB interface and serves as both the master node and the base station in the experiments. The function generator is externally triggered by the base station

to generate five-peaked signals. The KH-7602 amplifier provides appropriate gain for the signal from the function generator. Additionally, the digital oscilloscope is used to monitor the excitation signal and the response signals.

Since each transduction module in wireless sensors connected to the piezoelectric discs may have different sensitivity due to the mounting of the piezoelectric discs and drifts of the electric components, calibration must be firstly made before measurements. The digital oscilloscope is used to measure the outputs from the amplifier stage of slave sensors' transduction modules. By making excitation with the same parameters used in experiments, the output amplitudes of the amplifier on the transduction module are adjusted to be identical. Consequently, the gain factors can be set to be normalized to 1.

6.3 Experiments on Active Damage Localization

It must be noted that the algorithms given in the previous Chapter are solely developed to localize the emission source or the foreign object impact. To evaluate structure and find potential damage, an assumption must be made that the incipient damage area is small enough that the scattered wave can be treated as a secondary omni-directional point wave source. Additionally, in order to obtain the reflected waves solely from damages, the response wave signals at each sensor are measured twice: before and after damages. Since a SHMS usually installed in the field while structure is in healthy status, the requirement of the priori knowledge, the pre-damage wave, will not bring any issue or increase power consumption for additional measurements since only one time collection of the pre-damage wave is required which can be stored inside the wireless sensors permanently. Then, the reflected wave signals can be obtained by subtracting the post-damage signals from the pre-damage signals.

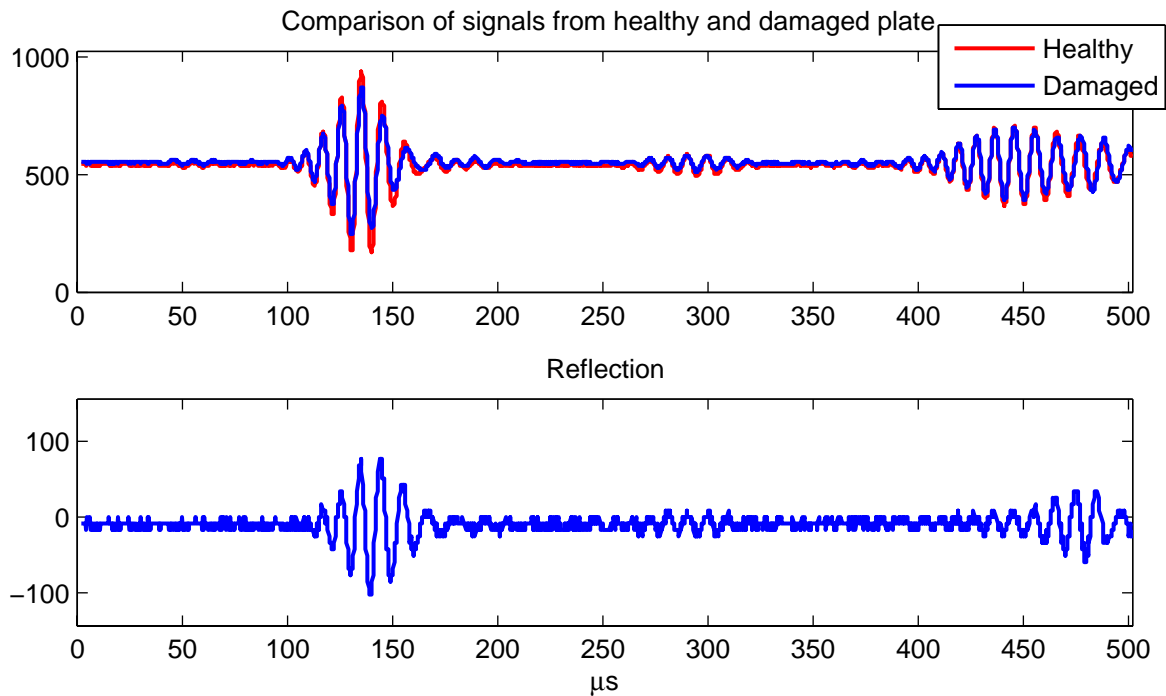


Figure 6.4 Pre-damage wave, post-damage wave, and their difference (reflection wave)

Figure 6.4 plots the wave signals collected by a wireless sensor before and after damage and the reflected wave in time domain. The excitation voltage is ± 12 V and the central frequency is 100 kHz in this experiment. Since the input span of the ADC is set to 0-2 V and the resolution is 10-bit, the unit of vertical axes is $2V/1024$. The figure includes the data in 500 μs duration with 10MHz sampling rate. In the upper plot, the first wave packets can be identified as the five-peaked waves propagated from the actuator to the sensor through the shortest path with slight dispersion effect. Since the damage interferes with the direct propagation, the post-damage sensor signal has smaller amplitude than the one before damage. After subtracting them, the difference presents the reflection solely from the damage, which is shown in the lower plot. Besides the first wave packet, several additional wave packets, which arrive at the sensor after 400 μs , also can be observed in the figure. These wave packets are generated by the boundary reflection of the plate. In practice, these

wave packets can be precluded by setting an appropriate time window.

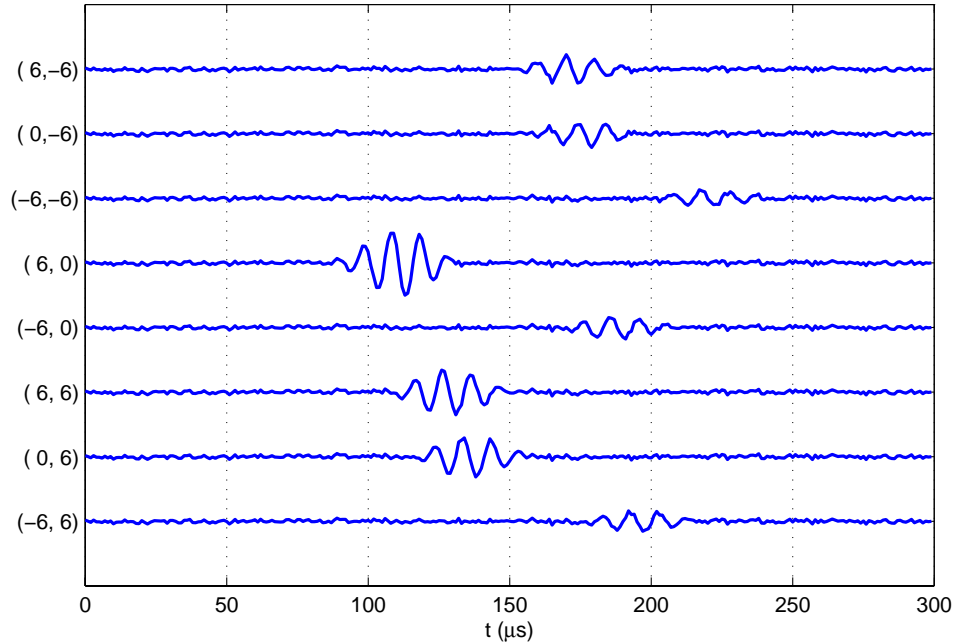


Figure 6.5 The reflection waves recovered in wireless sensors with the 1/16 inch plate

Figure 6.5 shows the normalized plots of reflection waves collected and calculated in the wireless sensors. The imitated damage is located northeastward inside the most inner square area surrounding the actuators. The numbers in the parentheses along the y-axis indicates sensor locations in the unit of inch as previously described grid. It can be clearly seen that reflection waves reach different sensors with different amplitudes at different times. All reflection waves are still packed in the time domain under the five-peaked wave excitation. Dispersion effect can be observed as well. Among these signals, signals from wireless sensors which is nearby the damage have stronger amplitude and the SNR of these signals are obviously better than others. The figure also indicates that the damage can be considered as an excitation source after direct subtraction and the scattered wave still complies with the energy decay model.

On the other hand, the side effect of the subtraction is that the measurement is more susceptible to noise. Since the damage is not a strictly a point damage, which is often the

case in real field applications, multiple reflections with different paths or dispersion may occur. Although the strength of such disturbance is not strong, it will induce low SNR if the original excitation has relatively low intensity. Moreover, instrumentational noise and electromagnetic interference become conspicuous since the gain of the amplifier for the signal conditioning of piezoelectric has to be increased. In addition, the imperfect installation of piezoelectric transducer may also result impaired sensitivity. In particular, since the damage is imitated by increased stiffness which is induced by applying magnetic force, the reflection factor of the damage is relatively small. Consequently, the signals collected at sensors that are far from the damage will have poor SNR. Figure 6.6 shows the normalized reflection waves under a similar setup except that the thickness of the plate is 1/8 inch. Although the noise characteristics, or more specifically the standard deviation of noise, are almost identical to that shown in Figure 6.5, the SNR for all signals are decreased dramatically and it is hard to distinguish the reflected wave packets from some of these signals. As environmental noises, such as the vibration generated by the fan inside the power amplifier in this setup, are substantive, the pre-damage signal and the post-damage signal may have different noise features, or standard deviation. This will generate in another source of error for the methods using the energy decay model.

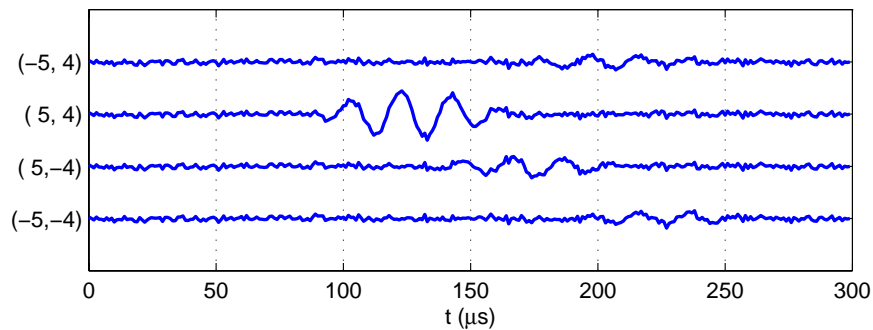


Figure 6.6 The reflection waves recovered in wireless sensors with a 1/8 inch plate

To obtain acceptable SNR and improve accuracy, sensor nodes from which data are used for damage localization must be pre-selected within the WSN. In the following experiments and results, the selection of sensor nodes in the WSN is determined by comparing the energy of reflection wave from different nodes. Four sensor nodes with maximum energy reading will be elected to participate in the damage localization.

6.3.1 Damage localization in base station with the Levenberg-Marquardt method

Firstly, the L-M method presented in Section 5.3 is verified using wireless sensors and the plate with 1/8 inch thickness. To give comparison and prove the potential gain of power efficiency through local processing in wireless sensors, first the collected data are directly transmitted to the base station, rather than being processed inside slave nodes. The computer will calculate the energy of signals from individual slave node, and employ L-M method to iteratively find out the damage location.

Table 6.1 Results of damage localization using the L-M method

#	Excitation		Damage Location (cm)	Sampling Freq. (MHz)	Data Points	Epoch	Result (cm)	Error (cm)	Error/Di*
	Voltage (V)	Central Freq. (kHz)							
1	±12	40	(3.81, -5.08)	10	3000	46	(2.40, -3.25)	2.31	7%
2	±12	40	(3.81, -5.08)	4	1200	46	(0.99, -7.89)	3.99	12%
3	±40	40	(3.81, -5.08)	10	3000	55	(4.09, -4.19)	0.93	3%
4	±40	40	(3.81, -5.08)	4	1200	38	(3.60, -4.39)	0.72	2%
5	±40	40	(7.62, 10.16)	10	3000	56	(7.01, 9.21)	1.12	3%
6	±40	40	(2.54, -2.54)	10	3000	57	(1.63, -3.21)	1.13	3%
7	±40	90	(7.62, -5.08)	10	2500	54	(7.94, -6.82)	1.76	5%
8	±40	90	(7.62, -5.08)	4	1000	45	(7.77, -6.74)	1.66	5%

* Di=32.5 cm is the diagonal of the sensor grid

Table 6.1 gives results from the experiments. The initial guesses for the L-M method in all cases are set to (7.62, 5.08) cm. The last column in the table gives the ratios of the offset between the result and the actual damage position and the diameter of the magnetic stone. It can be clearly seen that the energy decay model and the L-M optimization method

give robust performance on damage localization.

The importance of SNR is noticeably observed by comparing the 1st and 2nd cases with 3rd and 4th cases. With higher excitation voltages, the errors are significant less than that with low excitation voltages. However, since the energy decay model has included the influence of noise, the L-M method can still converge to an acceptable result as that the error is comparable with the diameter of the magnet stones.

With the excitation at peak voltages of ± 40 V, good convergences were made in all experiments. The central frequency of the excitation signal is increased to 90 kHz to compare with the results with those from 40 kHz. It can be seen that the localization errors increase when the central frequency increases. This may be attributed to two reasons: parasitic higher mode may exist since the central frequency is more close to the cutoff frequency (1MHz) of the A_1 mode; and strict requirement on synchronization as the group velocity increases proportional to the central frequency.

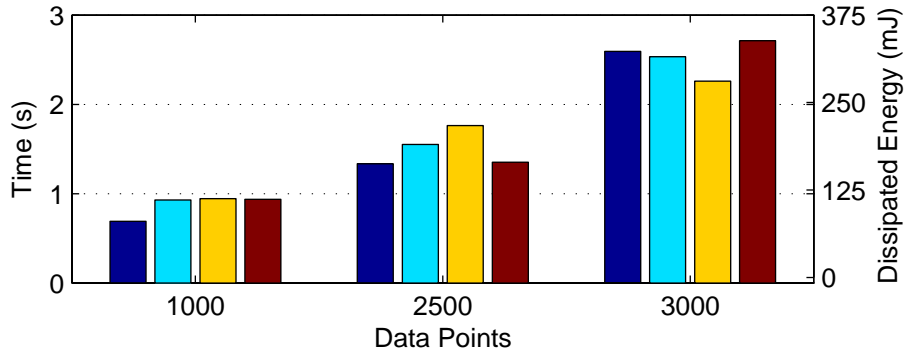


Figure 6.7 Time and energy consumption measured using the L-M method

Another aim of the experiments is to verify the high speed sensing capability of the wireless sensor, sampling rate of 10 Msps is primarily adopted. Nevertheless, excessive sampling rate results in large amount of data to be processed or transferred. As long as Shannon theorem can be satisfied to correctly recover waveforms, low sampling rate is

desired. 300 μs and 250 μs time windows are chosen for the 40 kHz and 90 kHz excitation, respectively, and the amount of data points collected in each experiment are also given in Table 6.1. The duration required to transmit the collected data are measured and plotted in Figure 6.7. Four measurements were made on each amount of data points. Since the actual communication speed depends on the wireless channel, the measurements show minor variances on same amount of data. As the average current consumption for the wireless sensor in transmission mode is 38 mA, the axis in the right hand side indicates the dissipated energy as the nominal voltage is 3.3V. The lessening on the sampling rate actually decreases the size of collected data, and resultantly the power consumption for communication and the computation can be reduced.

6.3.2 Embedded damage localization using cross-correlation and SVD

Secondly, experiments are conducted by embedding the cross-correlation method in wireless sensor. However, as discussed in Section 5.5, it is nearly impractical to directly implement cross-correlation method in the wireless sensor due to extremely long computation time required. Optimization and tradeoff must be applied to reduce the computation time and make the cross-correlation algorithm practical to be embedded in the wireless sensor.

Since the CCF represents the similarity of two data sets, the data of collected reflection wave can be cross-correlated with numerically modeled excitation. Noticing that the envelope of the five-peaked wave is modulated by a Hanning window, it can be found that the modeled excitation has non-zero values only within the first five periods of excitation. Accordingly, the computation for the rest part can be abrogated. The total number of multiplication and summation can be reduced to

$$N_{mul} = N_{sum} = M(N - M) + M(M - 1)/2 = M\left(N - \frac{M + 1}{2}\right) \quad (5.25)$$

where N is the number of collected data points, $M = 5 f_s / f_c$, f_s is the sampling frequency, and f_c is the central frequency of the excitation. For instance, for 1200 data points with 4 MHz sampling frequency and 100 kHz central frequency, the optimized procedure only requires 21990 cycles, which is three times less than that required originally.

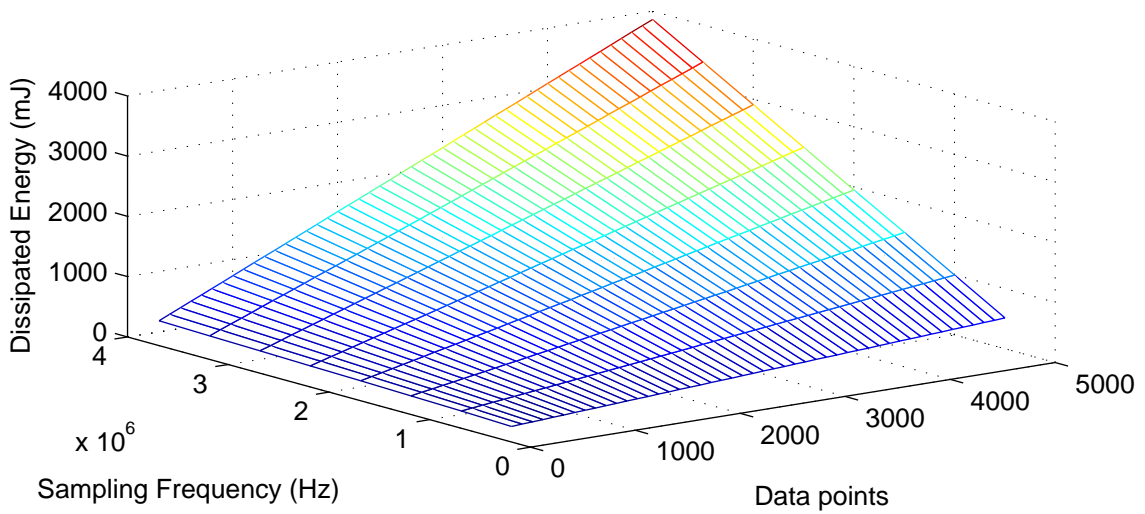


Figure 6.8 Energy consumption measured using the cross-correlation method in slave nodes

Figure 6.8 depicts the measured energy consumption of slave sensors with the cross-correlation method. The energy consumed per operation is plotted with respect to the amount of data points and the sampling frequency. As only a 16-bits integer, the calculated time lag, needs to be transmitted out, the communication consumption is ignored. With an average current consumption at 17 mA and nominal voltage at 3.3 V, the dissipated energy values are obtained by measuring the total time required for the slave nodes to complete the whole calculation. The central frequency is fixed to be 100 kHz, and discrete values are interpolated for graphical purpose. As expected, the dissipated energy is proportional to both factors. The

subservience of the optimization is evident, as the dissipated energy increases in a faster rate as the sampling frequency becomes higher. For the same instance described in the last paragraph, which implies that the sampling duration is 300 μ s, the energy consumption is 880 mJ. Comparing that with the results from the L-M method, the cross-correlation method does not outperform the L-M method with full transmission from viewpoint of energy conservation in the current setup. The only advantage is that damage localization can be made inside the sensor group. Nevertheless, it can not yield the conclusion that full transmission is better than local cross-correlation inside sensor nodes. When the WSN extends to a large scale and multi-hop communication has to be enforced, the energy consumption on full transmission may suffer drastically, which can not be reflected in the simple setup in this research. Since the energy consumption and processing time are independent with the scale of WSN, the cross-correlation method have steady performance practically and is still an acceptable embedded algorithm for wireless sensors.

Table 6.2 Results of damage localization using the cross-correlation method in slave nodes

#	Excitation		Damage (cm)	Sampling Freq. (MHz)	Data Points	Result (cm)	Error (cm)	Error/Di*
	Voltage (V)	Central Freq. (kHz)						
1	± 5	100	(5.08, 10.16)	4	1200	(5.68, 12.25)	2.18	10%
2	± 5		(5.08, 10.16)	2	600	(6.49, 8.61)	2.1	10%
3	± 12		(5.08, 10.16)	4	1200	(5.89, 9.76)	0.9	4%
4	± 12		(5.08, 10.16)	2	600	(5.97, 9.43)	1.15	5%
5	± 12		(5.08, 10.16)	1	300	(5.87, 9.13)	1.3	6%
6	± 12		(-12.70, 2.54)	2	600	(-11.79, 2.92)	0.98	5%
7	± 12		(-7.62, 7.62)	2	600	(-7.74, 8.38)	0.76	4%

* Di=21.55 cm is the diagonal of the sensor grid

Since the pseudo-inverse matrix can be pre-programmed into the master sensor node, the localization with time delays information is extremely simple and efficient. Thus, the energy consumption in the master node is trivial. Table 6.2 lists the parameters of several experiments conducted on the thinner plate with the calculated damage location and errors.

The central frequencies of the excitations are fixed to 100 kHz. Good agreements can be found between the actual damage positions and the calculated positions. The significant effect of SNR on accuracy can be seen as well from these results. Additionally, higher sampling frequency can yield slightly better results. To make tradeoff between the accuracy and the computation amount, it can be found that 2 MHz sampling frequency may be used in the experiment setup.

6.3.3 Embedded damage localization using the energy decay model and SVD

Finally, damage localization method based on the energy decay model is embedded in wireless sensors to compare its performance with that of previous two methods. As the evaluation of energy coefficients is pretty straightforward, a simple implementation of the algorithm is coded into slave sensors. In addition, SVD is embedded in the master nodes to perform calculation of the pseudo-inverse matrix required for damage localization.

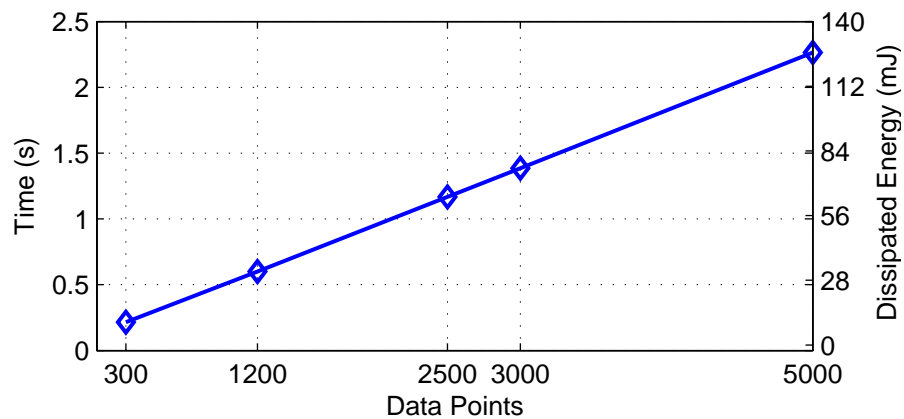


Figure 6.9 Energy consumption measured using the energy decay model in slave nodes

Figure 6.9 demonstrates the duration and energy consumption required to compute energy coefficients in slave nodes with respect to amounts of data points. The same method used to obtain energy values in Section 6.3.2 is adopted. It can be seen that the dissipated energy increases almost linearly with the number of data points. Compared with the values in

Figure 6.7 and Figure 6.8, the energy required to process the same amount of data points is much less than both previous cases. Since the communication consumption can be largely neglected, the figure actually reflects the energy consumption in slave nodes of a single diagnosis cycle. Also, measurements on master node are made to obtain energy consumption of performing SVD calculation. Since the number of sensors is fixed to four, the SVD calculations almost converge in the same amount of time, averaged at about 0.25 s or 14 mJ.

Table 6.3 Results of damage localization using the energy decay model in wireless sensors

#	Excitation		Damage (cm)	Sampling Freq. (MHz)	Data Points	Result (cm)	Error (cm)	Error/Di*
	Voltage (V)	Central Freq. (kHz)						
1	±12	100	(5.08, 10.16)	10	3000	(5.74, 9.33)	1.06	5%
2			(5.08, 10.16)	4	1200	(5.33, 9.47)	0.74	3%
3			(5.08, 10.16)	2	600	(5.61, 9.26)	1.05	5%
4			(5.08, 10.16)	1	300	(6.14, 9.29)	1.37	6%
5			(-12.70, 2.54)	2	600	(-11.33, 3.11)	1.49	7%
6			(-7.62, 7.62)	2	600	(-6.95, 8.44)	1.06	5%
7			(0.00, -3.82)	2	600	(-0.95, -4.23)	1.04	5%

* Di=21.55 cm is the diagonal of the sensor grid

Some of the results yielded from the energy decay model and SVD are given in Table 6.3. The excitation is fixed to have parameters of ±12V and 100 kHz. The imitated damage was varied at different locations to verify the performance the proposed algorithm. As expected, all detected damage locations are in good agreement with actual damage locations.

6.3.4 Comparison and summary

From the experiments, all the three methods of damage localization yield acceptable results of damage localization which have comparable accuracy. In this section, a brief review and comparison among them are given.

The first damage localization method was developed and verified mainly in the purpose of demonstrating traditional SHMS except the participation of wireless communication, in which all data are sent to a centralized base station for processing.

Although the L-M method does not offer significant benefits in terms of improving source localization accuracy with a large number of cost function evaluations, this method effectively gives a paradigm for wireless sensor SHMS that requires algorithms with computational complexity, i.e., migration [79].

The second method, which embedded cross-correlation algorithm into wireless sensors, gives examples that combine traditional TDOA based localization method and wireless sensor for active diagnosis. Although the potential damage location can be estimated within a wireless sensor group, it does not outperform the first scenario regarding to energy consumption, particularly in the setup in this research.

In the third method, a novel algorithm based on the energy model and SVD is implemented in wireless sensors. It addresses a strong prominence upon taking advantage of the sensor node’s “smart” core to detect potential damage and its location while keeps overall energy consumption low.

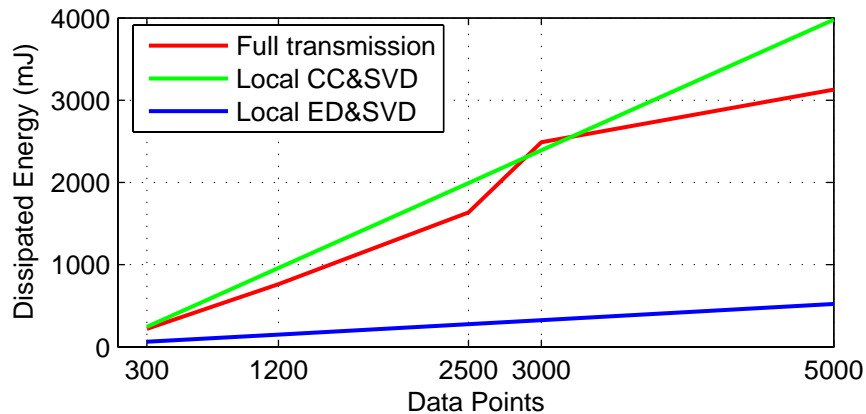


Figure 6.10 Comparison of total energy consumption for one diagnosis cycle in a group

To better explain the power efficiency gained by the proposed method, the energy consumption of one diagnosis cycle with the experiment setup and the described damage localization algorithms are plotted with respect to data points in Figure 6.10. The presented

data are the sum of the energy consumption of all four slave nodes and the master node, which are derived by the product of the average current consumption and the average time measured with different amount data points to be processed. For the first method, the energy consumption consists of communication consumption only; while for the other two methods, the computation consumption dominates, thus the communication consumption are quite small. It can be clearly seen that the last method is the best against the other two in energy consumption. Especially, the energy consumption for the last method increases much more slowly than those of the other two as the number of required data points gets larger and also is not coupled potential communication traffic.

A conclusion can be made herein that the proposed algorithm, energy decay model and its matrix solution, is a promising method for wireless sensors in active diagnosis. As the advantage and importance of local data processing for applying wireless sensor and active diagnosis in practical SHMS is shown, the proposed algorithm with the developed wireless sensor demonstrated the suitability for real-world WSN and SHM applications.

Finally, the factors that may affect the localization error with the proposed algorithm are listed and identified.

- a.) Standard deviation (STD) of noise: The standard deviations of noise are measured individually in all experiments. In practice, the pre-damage diagnosis and the post-damage diagnosis may be affected by noise with different STDs.
- b.) SNR: It has been extensively studied in both simulations and experiments.
- c.) Sensor gain and piezoelectric bonding: The transduction modules are pre-calibrated in all experiments as described at the beginning of this Chapter. However, perfect bonding of piezoelectric disc is implied and assumed. If the bonding is imperfect, the

piezoelectric discs may not pick up propagating waves with the same sensitivity equally in all directions. This will eventually generate error for the accuracy of energy coefficients.

- d.) Instrumentational error and quantitative error: Thermal noise existed in miscellaneous ICs also have impact on the accuracy, especially when SNR is low. Additionally, as the ADC has finite resolution, quantitative error may also be arisen for the evaluation of the energy coefficients.

7 Conclusions and Future Studies

7.1 Conclusions

In this dissertation, challenges of applying wireless sensors to active diagnosis for SHM have been addressed in detail. Focus has been placed on the development of active wireless sensor SHMS with power aware hardware, software and embedded algorithms.

After an extensive review of wireless sensors for SHM, the inadequacies of conventional designs for active diagnosis are described. Due to the centralized architecture and serial operation of ordinary MCU, traditional wireless sensor architecture not only suffers from limited data acquisition capability but also results in reduced power efficiency. Based on the preliminary researches, a novel dual processors based architecture is proposed and presented. By empowering wireless sensor capable of parallel controlling and processing, the optimized architecture can use dynamic frequency scaling to maximize power efficiency by eliminating unnecessary power consumption during data acquisition. Implementation of the architecture to build a comprehensive wireless sensor platform for SHM is also described in detail and verification of the acquisition accuracy is made.

The second part of this dissertation addresses the power awareness of damage localization algorithms which possess self-diagnosis capability and which must be embedded in the wireless sensor. With limited computation bandwidth and energy supply, efficient damage localization algorithms must be developed. TDOA based algorithms use cross-correlation technology to seek time differences to determine the propagating distance of diagnostic signals. However, in dispersive mediums, cross-correlation may fail to give correct results due to the inexactness in finding the similarity of the diagnosis signal and its dispersed version with distortion.

To employ diagnostic waves to detect damage, elastic wave propagation in plate-like structures is investigated. Higher-order theory is used to formulate the dispersion relation in isotropic plates. To correctly apply cross-correlation to dispersed waves after long-distance propagation, a linear mapping algorithm is developed to remove the dispersion and recompress dispersed waves. After dispersion removal, the spread of transient waves can be re-concentrated and the envelopes of propagating waves can be approximately recovered to the original form. Both simulations and experiments validate the effectiveness of the dispersion removal. Additionally, based on asymptotic expansion of the wave field, an energy decay model is derived and prepared for damage localization. With preclusion of the noise, the proposed model provides a simple, yet effective method to calculate propagation distance by measuring the intensity of the diagnosis signal.

As both methods have attractive potentials that enable dramatic reduction of the communication consumption and possibility of distributed computation, the two localization methods are further investigated to be embedded into resource-constrained wireless sensors and to reduce computational complexity. Matrix solutions to eliminate iterative search are established to expedite calculation and reduce computation consumption with known geometry information of sensors. Comparisons are made first in terms of accuracy and efficiency based on simulation.

By embedding the proposed damage localization algorithms into the developed wireless sensor, experiments are conducted to validate the power efficiency of the proposed hardware and software. With comparable accuracy, three damage localization scenarios, which are full transmission, embedded cross-correlation and embedded energy based method, are tested and compared. It has been found that the proposed method based on the energy

decay model requires significantly less power consumption to find potential damage locations within a local wireless sensor group.

The specific contributions made in this study are summarized below.

- a.) A novel architecture of wireless sensor, dual processor/controller architecture, is proposed and verified in this work. The architecture aims at providing a power aware platform for high speed acquisition applications, i.e., active diagnosis for SHM.
- b.) A compact wireless sensor with sizes of 30mm×30mm×35mm is developed to provide a hardware platform for wireless sensing and to facilitate future research in SHM. With modularized design, the sensor provides ultrasonic sensing capability, specifically 10 MHz sampling frequency, without losing efficiency for general purpose applications. Detailed design and development are given in this dissertation.
- c.) Higher-order theory is applied to obtain dispersion relations, phase and group velocities for elastic wave propagation in isotropic plates. In comparison with those using 3-D elastic theory, the dispersion relations have good accuracy with the first few modes and have a simpler polynomial form which may be beneficial to reduce computational complexity.
- d.) Dispersion removal for elastic wave propagation is derived. A linear mapping algorithm is developed to recompress dispersed waves in time domain and has been verified through experimental data. Using the dispersion removal, the constraint on the choice of frequency range, where the dispersion effects are small, are relaxed.
- e.) Essential nonlinear problems involved in damage localization by using TDOA or energy ratios are converted to linear problems. A matrix solution is presented by applying singular value decomposition and pseudo-inverse matrix. The resulting

- damage localization algorithm requires much less computational resource than before.
- f.) The energy decay model and the matrix solution are successfully embedded into the compact wireless sensor to present a first fully embedded wireless sensor SHMS for damage localization.
 - g.) The power efficiency of WSN for SHM is addressed by studying three damage localization scenarios: full transmission, embedded cross-correlation and embedded energy based method. Experimental results have shown that distributed computing with proper algorithms inside wireless sensors show the promise in power efficiency over the traditional centralized approach. Furthermore, it can be concluded that the proposed energy based method has acceptable accuracy and lower power consumption, and is a promising method to be used in WSN.
 - h.) In general, this work is the first ever attempt to make wireless sensor practical for active diagnosis SHMS. The developed wireless sensor and the proposed damage localization algorithms leverage the applications of WSN in SHM.

7.2 Future Studies

There are numerous opportunities for research on wireless sensor for SHM in addition to the investigations presented in this dissertation. This section touches briefly on a few of those that seem most promising.

The excitation from actuators is made through an external function generator and amplifier in the experiments. To realize a practical autonomous SHMS, excitation, i.e. piezoelectric driver, must be fully embedded into wireless sensors. Upon solving the theoretical part that energy consumption for pure excitation is within the power budget of wireless sensors, various technical issues remain to be solved. For instance, to improve SNR,

piezoelectric must be driven with sufficiently high voltage whereas only low voltage supplies are available in wireless sensors. Power amplifiers that can provide proper gain with moderate energy consumption must be addressed. This will extend research into seeking the optimum operating point of piezoelectric and circuits. A particular transduction module for piezoelectric driving, which can boost the driving voltage to 12V has been developed in this research. This dissertation does not include it since it has not been completely tested.

As mentioned in the dissertation, the lack of a floating point processor greatly impedes embedding complex damage localization algorithms into wireless sensors. The deficiency may be more pronounced when those algorithms become essential and critical. Other approaches, such as choosing digital signal processor (DSP) or a specific floating point unit, may be investigated upon the consideration of power consumption.

Although the volume of the wireless sensor is small, further shrinkage of the physical size of the wireless sensor and lowering down the cost are critical to make it feasible for field applications. Without full integration of all functional modules into a single silicon chip, wireless sensor may still remain as a concept. As the lack of the knowledge in IC design, the architecture presented in this work is only proposed for COTS discrete ICs. Further optimization may be sought as technical obstacles may exist.

As the scale of wireless sensor network increases, wireless communication will consume significant energy. Since the focus of this research is put on applying wireless sensor for SHM, networking are not deeply investigated, but treated as a transparent technology which may be directly substituted into the wireless sensor. However, concerns about power efficiency are not completely covered without involving the topic of power aware communication for wireless sensor. This remains a hot topic in electrical engineering

field and is being extensively investigated. Although the result and the conclusions from those researches can be directly applied, WSN for SHM has unique features that might be of interest to further improve power efficiency.

Also, the proposed energy based method may be invalidated when noise is significantly comparable with diagnostic signals or when noise figures do not keep constant. More advanced methods, which must be able to take advantage of distributed computation, may be examined and employed as long as the computational complexity and the power budget are satisfied.

8 References

1. Chang, F.K. *Structural Health Monitoring: Current Status and Perspectives*. in *International Workshop on Structural Health Monitoring*. Stanford, CA. 1997
2. Spencer, B.F., M.E. Ruiz-Sandoval, and N. Kurata, *Smart Sensing Technology: Opportunities and Challenges*. *Journal of Structural Control and Health Monitoring*, 2004. **11**(4): p. 349-368.
3. Shih, E., S. Cho, F.S. Lee, B.H. Calhoun, and A. Chandrakasan, *Design considerations for energy-efficient radios in wireless microsensor networks*. *Journal of VLSI Signal Processing Systems*, 2004: p. 77-94.
4. Straser, E.G. and A.S. Kiremidjian, *A modular wireless damage monitoring system for structures*, in *Technical Report 128*. 1998, John A. Blume Earthquake Engineering Center Stanford University.
5. Mitchell, K., S. Sana, V.S. Balakrishnan, V. Rao, and H.J. Pottinger. *Micro sensors for health monitoring of smart structures*. in *SPIE Conference on Smart Electronics and MEMS*. 1999.(**3673**): p. 351-358
6. Lynch, J.P., K.H. Law, A.S. Kiremidjian, T.W. Kenny, E. Carryer, et al. *The Design of a wireless Sensing Unit for Structural Health Monitoring*. in *The 3rd International Workshop on Structural Health Monitoring*. Stanford, CA. 2001
7. Lynch, J.P., A. Sundararajan, K.H. Law, A.S. Kiremidjian, and E. Carryer, *Embedding damage detection algorithms in a wireless sensing unit for operational power efficiency*. *Smart Materials and Structures*, 2004. **13**(4): p. 800.
8. Lynch, J.P., A. Sundararajan, K.H. Law, H. Sohn, and C.R. Farrar. *Design and Performance Validation of a Wireless Active Sensing Unit*. in *The International Workshop on Advanced Sensors, Structural Health Monitoring, and Smart Structures*. Tokyo, Japan. 2003
9. Lynch, J.P., *Design of a wireless active sensing unit for localized structural health monitoring*. *Structural control and health monitoring*, 2005. **12**: p. 405-423.
10. Lynch, J.P., A. Sundararajan, K.H. Law, E. Carryer, C.R. Farrar, et al., *Design and performance validation of a wireless sensing unit for structural health monitoring applications*. *Structural Engineering and Mechanics*, 2004. **17**(3): p. 394-408.
11. Hill, J.L. and D.E. Culler, *MICA: A Wireless Platform for Deeply Embedded Networks*. *IEEE Microelectric*, 2002. **22**(6): p. 12-24.
12. Kling, R., R. Adler, J. Huang, V. Hummel, and L. Nachman. *Intel Mote: using bluetooth in sensor networks*. in *Proceedings of the 2nd international conference on Embedded networked sensor systems* 2004: p. 318

13. IEEE, *Piezoelectricity IEEE Standard 1976*. 1976, IEEE.
14. Sazonov, E., K. Janoyan, and R. Jha. *Wireless Intelligent Sensor Network for Autonomous Structural Health Monitoring*. in *Proceedings of the SPIE, in Smart Structures and Materials: Smart Sensor Technology and Measurement Systems, San Diego, CA*. 2004.(**5384**): p. 305-314
15. Farrar, C.R., D.W. Allen, S. Ball, M.P. Masquelier, and G. Park. *Coupling Sensing Hardware with Data Interrogation Software for Structural Health Monitoring*. in *Proceedings of the 6th International Symposium on Dynamic Problems of Mechanics*. 2005
16. Xu, N., S. Rangwala, K.K. Chintalapudi, D. Ganesan, A. Broad , et al., *A wireless sensor network For structural monitoring*, in *Proceedings of the 2nd international conference on Embedded networked sensor systems*. 2004, ACM Press: Baltimore, MD, USA.
17. O'Flynn, B., S. Bellis, K. Mahmood, M. Morris, G. Duffy, et al., *A 3D miniaturized programmable transceiver*. *Microelectronics International*, 2005. **22**: p. 8-12.
18. Kiremidjian, A.S., T.W. Kenny, K.H. Law, and T. Lee, *A wireless modular health monitoring system for civil structures*. Proposal to the National Science Foundation,NSF 0121842, 2001.
19. Lamb, H., *On waves in an Elastic Plate*. *Proceedings Royal Society London*, 1917. **93(A)**: p. 114-128.
20. Lin, X. and F.G. Yuan, *Diagnostic Lamb waves in an integrated piezoelectric sensor/actuator plate: analytical and experimental studies*. *Smart Materials and Structures*, 2001. **10(5)**: p. 907-913.
21. Sohn, H., G. Park, J.R. Wait, N.P. Limback, and C.R. Farrar, *Wavelet-based active sensing for delamination detection in composite structures*. *Smart Materials and Structures*, 2004. **13(1)**: p. 153-160.
22. Lynch, J.P. and K.J. Loh, *A Summary Review of Wireless Sensors and Sensor Networks for Structural Health Monitoring*. *The Shock and Vibration Digest*, 2006. **38(2)**: p. 91-128.
23. Doebling, S.W., C.R. Farrar, and M.B. Prime, *A Summary Review of Vibration-based Damage Identification Methods*. *Shock and Vibration Digest*, 1998. **30(2)**: p. 91-105.
24. Callaway, E.H., *Wireless Sensor Networks: Architectures and Protocols*. 2003: CRC Press. 352.
25. Akyildiz, I.F., W. Su, Y. Sankarasubramaniam, and E. Cayirci, *Wireless sensor networks: a survey*. *The International Journal of Computer and Telecommunications Networking*, , 2002. **38**: p. 393-422.

26. Jiang, X.F., J. Polastre, and D.E. Culler. *Perpetual environmentally powered sensor networks*. in *The 4th international symposium on Information processing in sensor networks*. 2005: p. 463-468
27. Chandrakasan, A., R. Min, M. Bhardwaj, S. Cho, and A. Wang. *Power Aware Wireless Microsensor Systems*. in *The 32nd European State Device Research Conference*. 2002: p. 37-44
28. Sodano, H.A., D.J. Inman, and G. Park, *A Review of Power Harvesting from Vibration Using Piezoelectric Materials*. The Shock and Vibration Digest, 2004. **36**(3): p. 197-205.
29. Liu, L., F.G. Yuan, and F. Zhang, *Development of Wireless Smart Sensor for Structural Health Monitoring*. Proceedings of the SPIE Smart Structures and Materials conference, 2005. **5765**(1): p. 176-186.
30. Liu, L. and F.G. Yuan. *Development of Wireless Piezoelectrics Sensor on the MICA Platform*. in *The 1st International Workshop on Advanced Smart Materials and Smart Structures Technology*. 2004: p. 253-260
31. Hill, J.L., *System Architecture for Wireless Sensor Networks*. Ph.d Thesis, UC Berkeley, Berkeley, CA, 2003: p. 186.
32. Pop, P., P. Eles, and Z. Peng, *Analysis and Synthesis of Distributed Real-Time Embedded Systems*. 2004: Kluwer Academic Publishers. 326.
33. Brynjolfson, I. and Z. Zilic. *Dynamic clock management for low power applications in FPGAs*. in *The IEEE Custom Integrated Circuits Conference*. 2000: p. 139-142
34. Atmel, *AT94K05/10/40AL datasheet*. www.atmel.com, 2005.
35. *AD9200 datasheet*, in www.analog.com. 2005, Analog Device.
36. Erickson, R.W., *Fundamentals of Power Electronics*. 1997, Massachusetts: Kluwer Academic.
37. Liu, L. and F.G. Yuan. *Design of wireless sensor for high frequency applications*. in *The 5th international workshop on structural health monitoring*. Stanford, CA. 2005: p. 1602-1609
38. *CC2420 datasheet*, in www.chipcon.com. 2005, Chipcon.
39. Graff, K.F., *Wave Motion in Elastic Solids*. 1991.
40. Reissner, E., *On Bending of Elastic Plates*. Quarterly of Applied Mathematics, 1947. **5**(1): p. 55-68.

41. Mindlin, R.D., *Influence of Rotatory Inertia and Shear in Flexural Motions of Isotropic Elastic Plates*. Journal of Applied Mechanics, 1951. **ASME 18**: p. 31-38.
42. Reissner, E., *The Effect of Transverse Shear Deformation on the Bending of Elastic Plates*. Journal of Applied Mechanics, 1945. **ASME 12**: p. A69-A77.
43. Achenbach, J.D., *Wave Propagation in Elastic Solids*. 7th ed. 1999: Elsevier Science. 426.
44. Reddy, J.N., *Theory and analysis of elastic plates*. 1999, Philadelphia, Pa: CRC. 540.
45. Kane, T.R. and R.D. Mindlin, *High-Frequency Extensional Vibrations of Plates*. Journal of Applied Mechanics, 1956. **ASME 23**: p. 277-283.
46. Whitney, J.M. and C.T. Sun, *A Higher Order Theory for Extensional Motion of Laminated Composites*. Journal of Sound and Vibration, 1973. **30**(1): p. 85-97.
47. Mindlin, R.D. and M.A. Medick, *Extensional Vibrations of Elastic Plates*. Journal of Applied Mechanics, 1959. **26**: p. 561-569.
48. Breitzke, M., *Seismogram synthesis and recompression of dispersion in-seam seismic multimode data using a normal-mode superposition approach*. Geophysical Prospecting, 1992. **40**(1): p. 31-70.
49. Alleyne, D.N., T.P. Pialucha, and P. Cawley, *A signal regeneration technique for long-range propagation of dispersive Lamb waves*. Ultrasonics, 1993. **31**(3): p. 201-204.
50. Mason, I.M., D.J. Buchanan, and A.K. Booer, *Channel wave mapping of coal-seams in the United Kingdom*. Geophysics, 1980. **45**(6): p. 1131-1143.
51. Smith, G.B. and I.M. Mason, *A parametric approach to the compression of seismic by frequency transformation*. Geophysical Prospecting, 1980. **28**(4): p. 551-571.
52. Smith, G.B. and R.N. Rango, *Dispersive noise removal in t-x space: Application to Arctic data*. Geophysics, 1988. **53**(3): p. 346-358
53. Booer, A.K., J. Chambers, and I.M. Mason, *Fast numerical algorithm for the recompression of dispersed time signals*. Electronic Letters, 1980. **13**: p. 453-456.
54. Robinson, J.C., *A technique for the continuous representation of dispersion in seismic data*. Geophysics, 1979. **44**(8): p. 1345-1351.
55. Li, X.P. *Dispersion removal from seismic signals by frequency rescaling*. in *EG Technical Program Expanded Abstracts 16*. 1997.**(16)**: p. 1147-1150

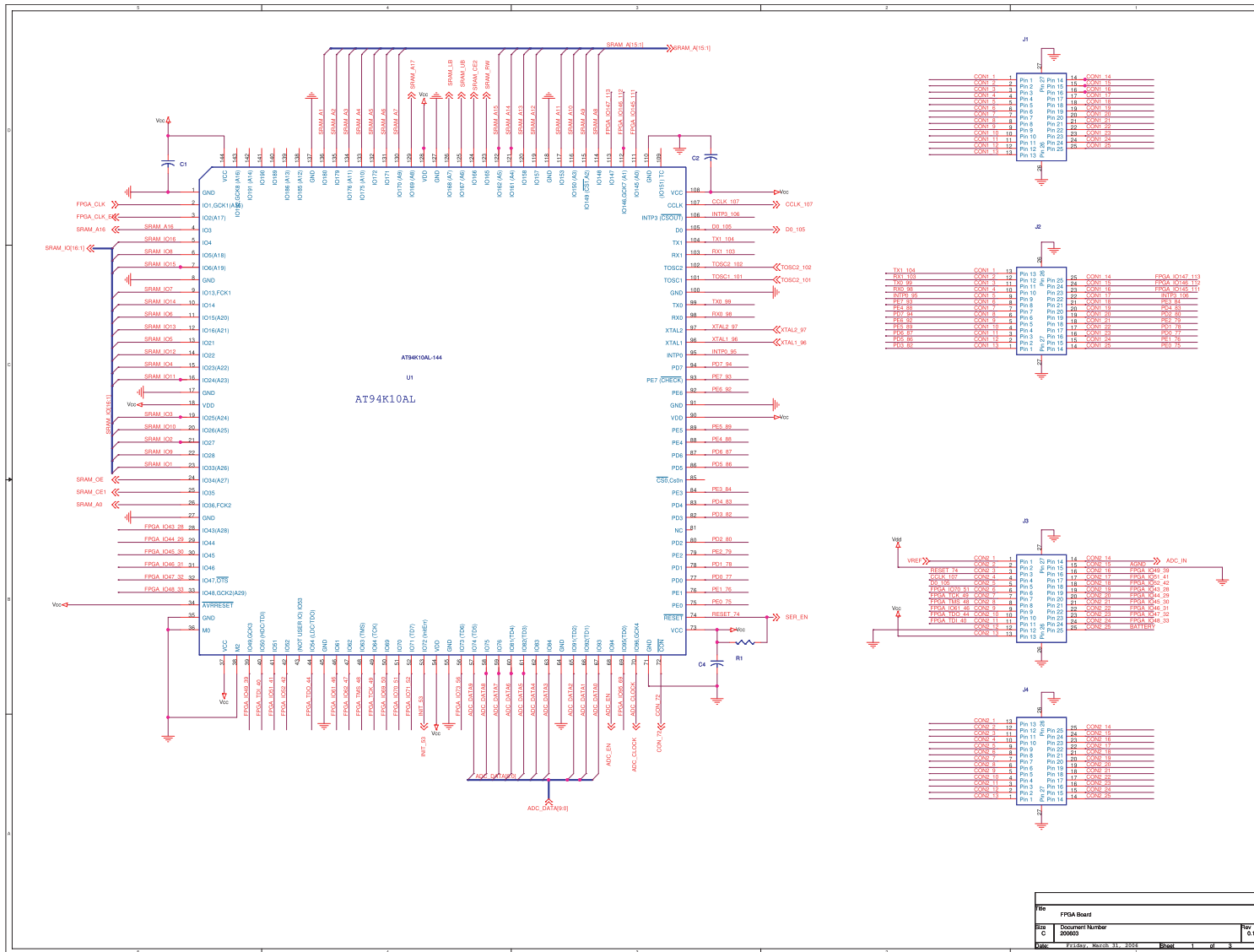
56. Wilcox, P.D., *A Rapid Signal Processing Technique to Remove the Effect of Dispersion from Guided Wave Signals*. IEEE transactions on ultrasonics, ferroelectrics, and frequency control, 2003. **50**(4): p. 419-427.
57. Santosa, F. and Y.H. Pao, *Transient Axially Asymptotic Response of an Elastic Plate*. Wave motion, 1989. **11**: p. 271-295.
58. Giurgiutiu, V., A.N. Zagari, and J. Bao, *Piezoelectric Wafer Embedded Active Sensors for Aging Aircraft Structural Health Monitoring*. Structural Health Monitoring, 2002. **1**(1): p. 41-61.
59. Crawley, E.F. and J. de Luis, *Use of Piezoelectric Actuators as Elements of Intelligent Structures*. AIAA journal, 1987. **25**: p. 1373–1385.
60. Keilers, C.H. and F.K. Chang, *Identifying delamination in composite beams using built-in piezoelectrics, I: experiments and analysis*. Journal of Intelligent Material Systems and Structures, 1995(6): p. 649-663.
61. Haykin, S., *Array Signal Processing*. 1985, Englewood-Cliffs, NJ: Prentice-Hall.
62. Taff, L.G., *Target Localization from Bearing-only Observations*. IEEE Transaction on Aerospace and Electronic Systems, 1997. **3**(1): p. 2-10.
63. Kaplan, L.M., Q. Le, and P. Molnár. *Maximum Likelihood Methods for Bearings-only Target Localization*. in *Proc. ICASSP*. Salt Lake City, UT. 2001: p. 554-557
64. Yao, K., R.E. Hudson, C.W. Reed, D. Chen, and F. Lorenzelli, *Blind Beam Forming on a Randomly Distributed Sensor Array System*. IEEE Journal Selected Areas in Communications, 1998. **16**: p. 1555-1567.
65. Reed, C.W., R.E. Hudson, and K. Yao. *Direct Joint Source Localization and Propagation Speed Estimation*. in *IEEE International Conference on Acoustics, Speech, and Signal Processing*. Phoenix, AZ. 1999: p. 1169-1172
66. Sheng, X.H. and Y.H. HU. *Energy Based Acoustic Source Localization*. in *The 2nd International Workshop on Information Processing in Sensor Networks*. Palo Alto, CA. 2003: p. 285-300
67. Sheng, X.H. and Y.H. Hu, *Maximum Likelihood Wireless Sensor Network Source Localization Using Acoustic Signal Energy Measurements*. IEEE Transaction on Signal Processing, 2003. **53**(1): p. 44-53.
68. Li, D. and Y.H. Hu, *Energy-Based Collaborative Source Localization Using Acoustic Microsensor Array*. Journal on Applied Signal Processing, 2003. **4**: p. 321-337.
69. Kehlenbach, M. and H. Hanselka. *Automated Structural Integrity Monitoring based on Broadband Lamb Wave Excitation and Matched Filtering*. in *The 44th*

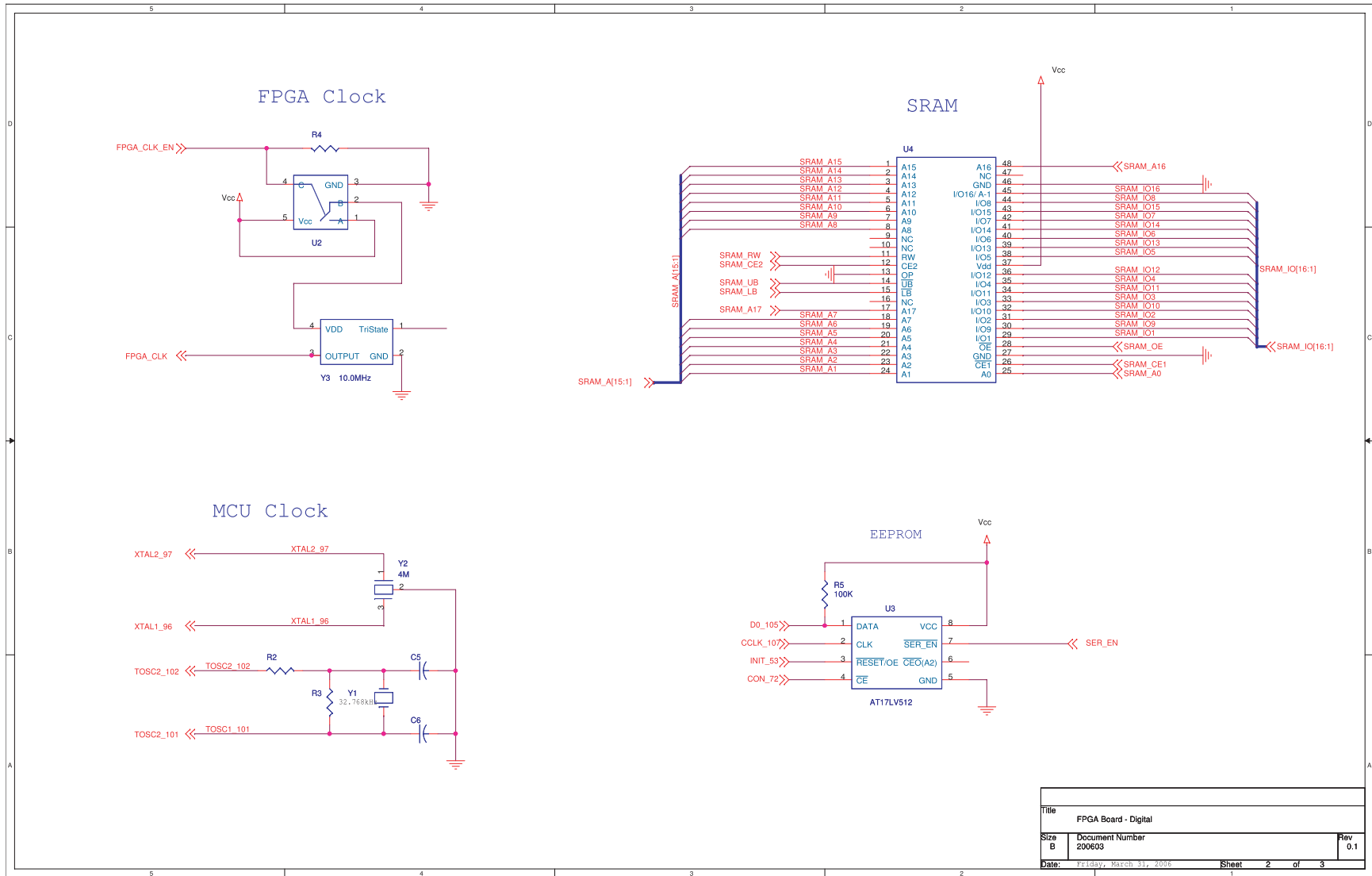
- AIAA/ASME/ASCE/AHS Structures, Structural Dynamics, and Materials Conference*. Norfolk, Virginia. 2003
70. Jeong, H., *Analysis of Plate Wave Propagation in Anisotropic Laminates Using a Wavelet Transform*. NDT&E International, 2001. **34**: p. 185-190.
 71. Winter, E.F. and D.A. Bies, *Correlation Properties Of Flexural Waves in Bars*. Journal of the Acoustical Society of America, 1962. **34**: p. 512-514.
 72. Ziola, S.M. and M.R. Gorman, *Source Location In Thin Plates Using Cross-correlation*. Journal of the Acoustical Society of America, 1991. **90**(5): p. 2551-2556.
 73. Lu, Y., Y. Lin, and Z.Q. Su, *Crack Identification in aluminum plates using Lamb wave signals of a PZT sensor network*. Smart Materials and Structures, 2006. **15**: p. 836-849.
 74. Ding, Y., R.L. Reuben, and J.A. Steel, *A New Method For Waveform Analysis For Estimating AE Wave Arrival Times Using Wavelet Decomposition*. NDT&E International, 2004. **37**: p. 279-290.
 75. Orfanidis, S.J., *Optimum Signal Processing. An Introduction*. 2nd ed. 1996, Englewood Cliffs, NJ: Prentice-Hall.
 76. Wang, L., *Elastic Wave Propagation in Composites and Least-Squares Damage Localization Technique*. Master's Thesis, North Carolina State University, Raleigh, North Carolina, 2004.
 77. Press, W.H., B.P. Flannery, S.A. Teukolsky, and W.T. Vetterling, *Numerical recipes in C: the art of scientific computing*. Cambridge University Press, 2nd edition, 1992.
 78. Björck, A.k., *Numerical methods for least squares problems* SIAM, Philadelphia, 1996.
 79. Klema, V.C. and A.J. Laub, *The Singular Value Decomposition: Its Computation and Some Applications*. IEEE Transactions on automatic control, 1980. **AC-25**(2): p. 164-176.
 80. Lin, X., *Structural Health Monitoring Using Geophysical Migration Technique with Built-in Piezoelectric Sensor/Actuator Arrays*. Ph.D's Thesis, North Carolina State University, Raleigh, North Carolina, 2000.
 81. Jetcheva, J.G. and D.B. Johnson. *Adaptive demand-driven multicast routing in multi-hop wireless ad hoc networks*. in *Proceedings of the ACM International Symposium on Mobile Ad Hoc Networking and Computing, MobiHoc*. Long Beach, CA. 2001. **(33-44)**

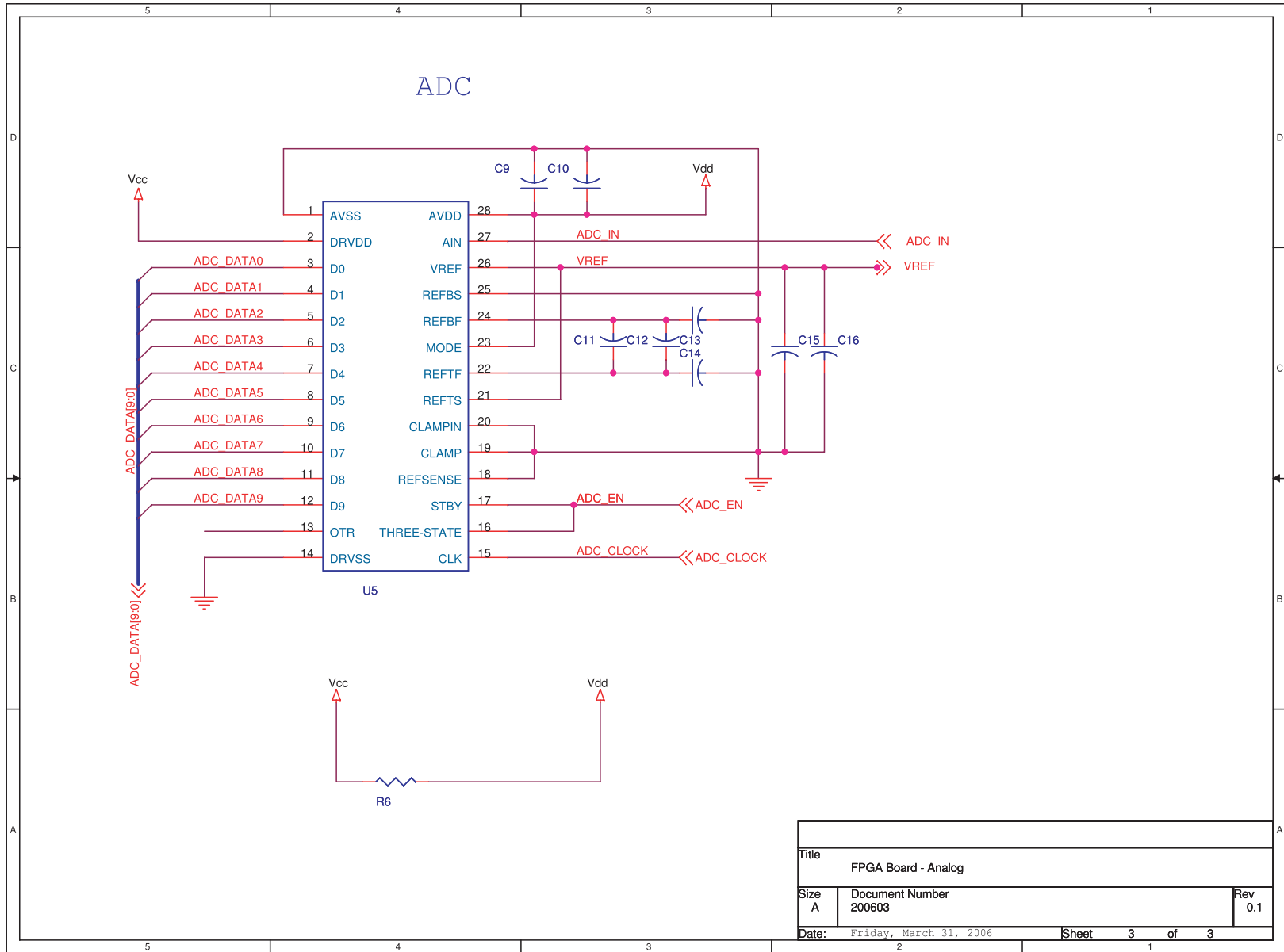
82. Choi, J.Y., H.S. Kim, I. Baek, and W.H. Kwon, *Cell based energy density aware routing: a new protocol for improving the lifetime of wireless sensor network*. Computer Communications, 2005. **28**(11): p. 1293-1302.
83. Muruganathan, S.D., D.C.F. Ma, R.I. Bhasin, and A.O. Fapojuwo, *A centralized energy-efficient routing protocol for wireless sensor networks*. IEEE Radio Communications, 2005. **43**(3): p. 8-13.
84. Zhao, J. and R. Govindan. *Understanding Packet Delivery Performance In Dense Wireless Sensor Networks*. in *The 1st International Conference on Embedded Networked Sensor Systems*. Los Angeles, CA. 2003: p. 1-13

APPENDIX

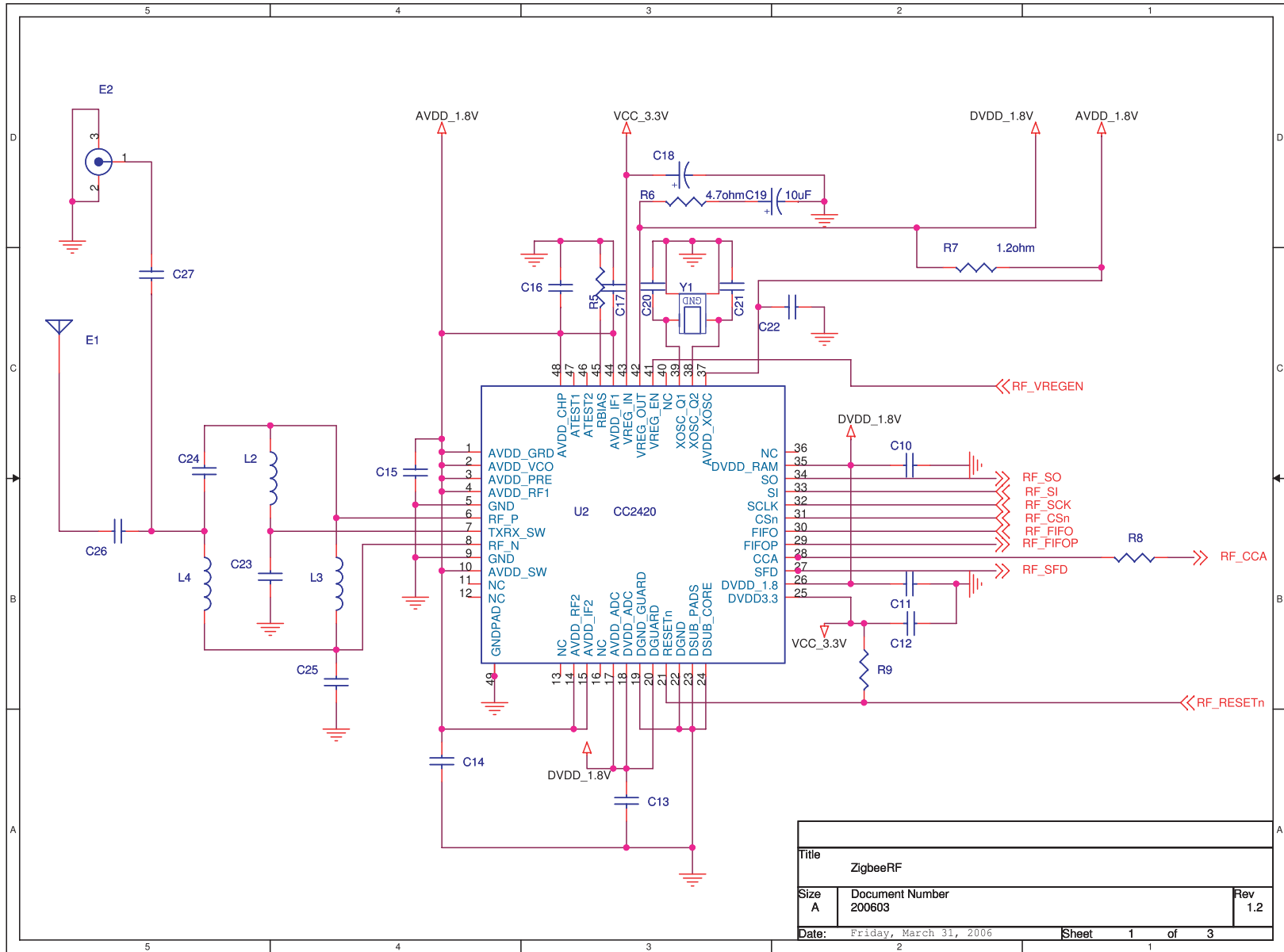
Appendix A: Schematics of the Wireless Sensor

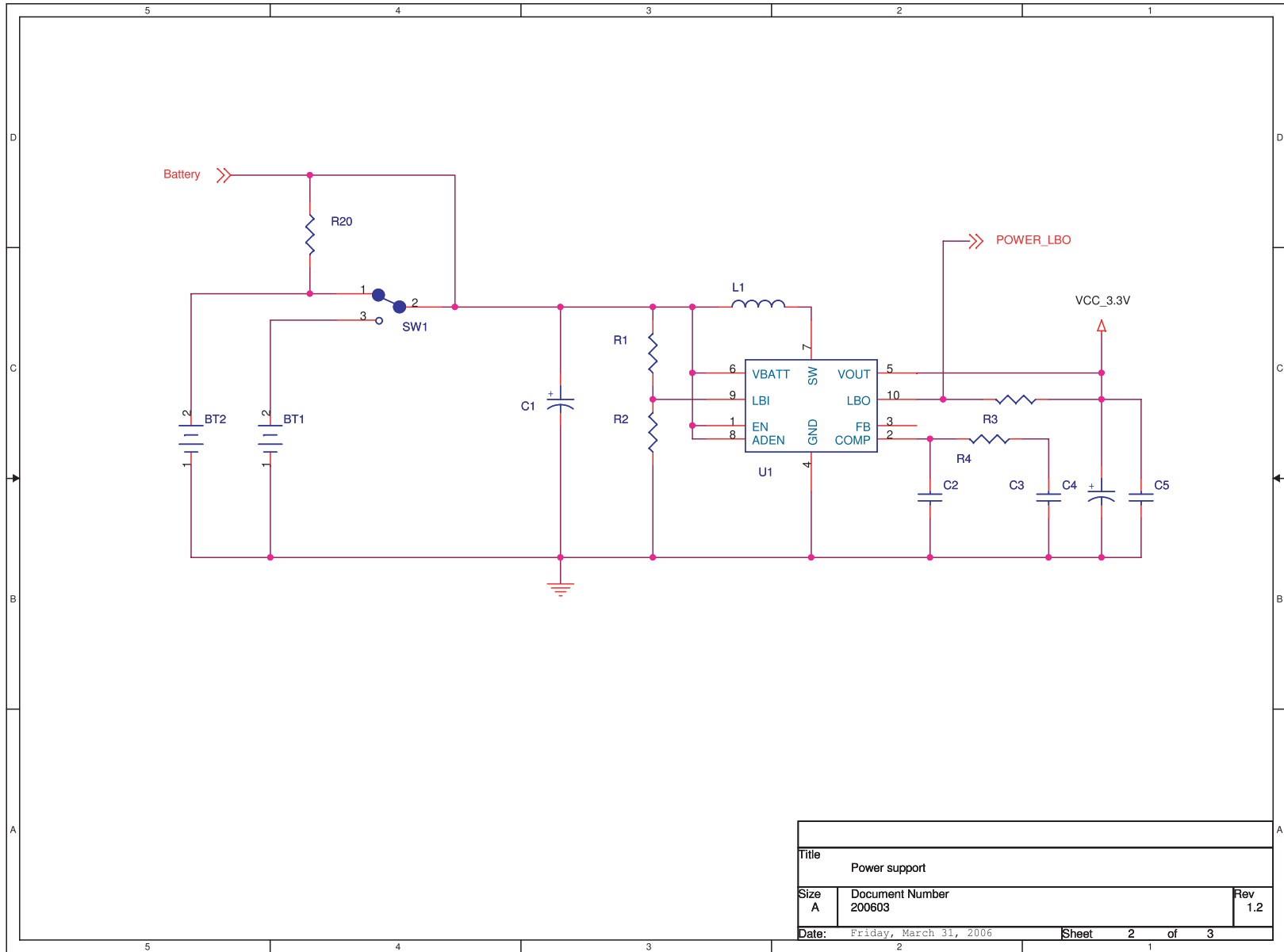






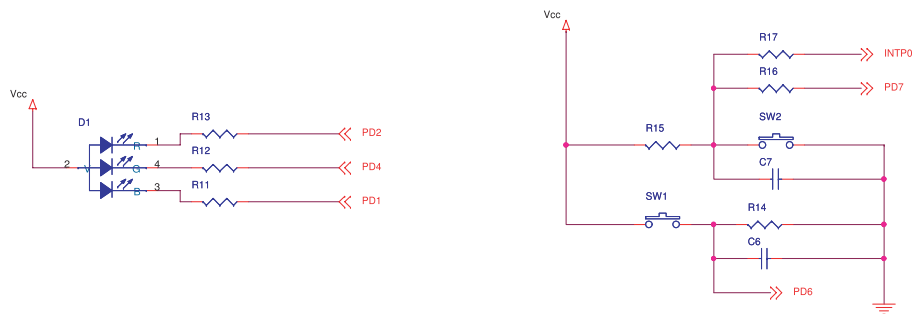
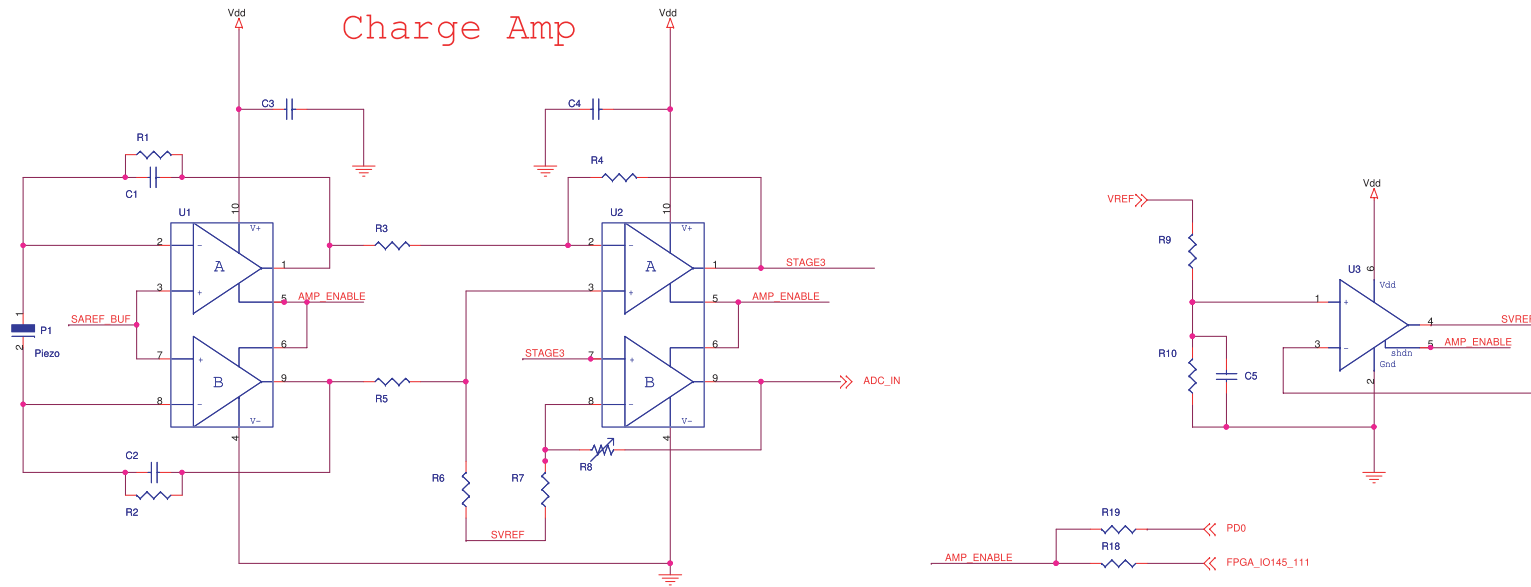
Title		
FPGA Board - Analog		
Size	Document Number	Rev
A	200603	0.1
Date:	Friday, March 31, 2006	Sheet 3 of 3



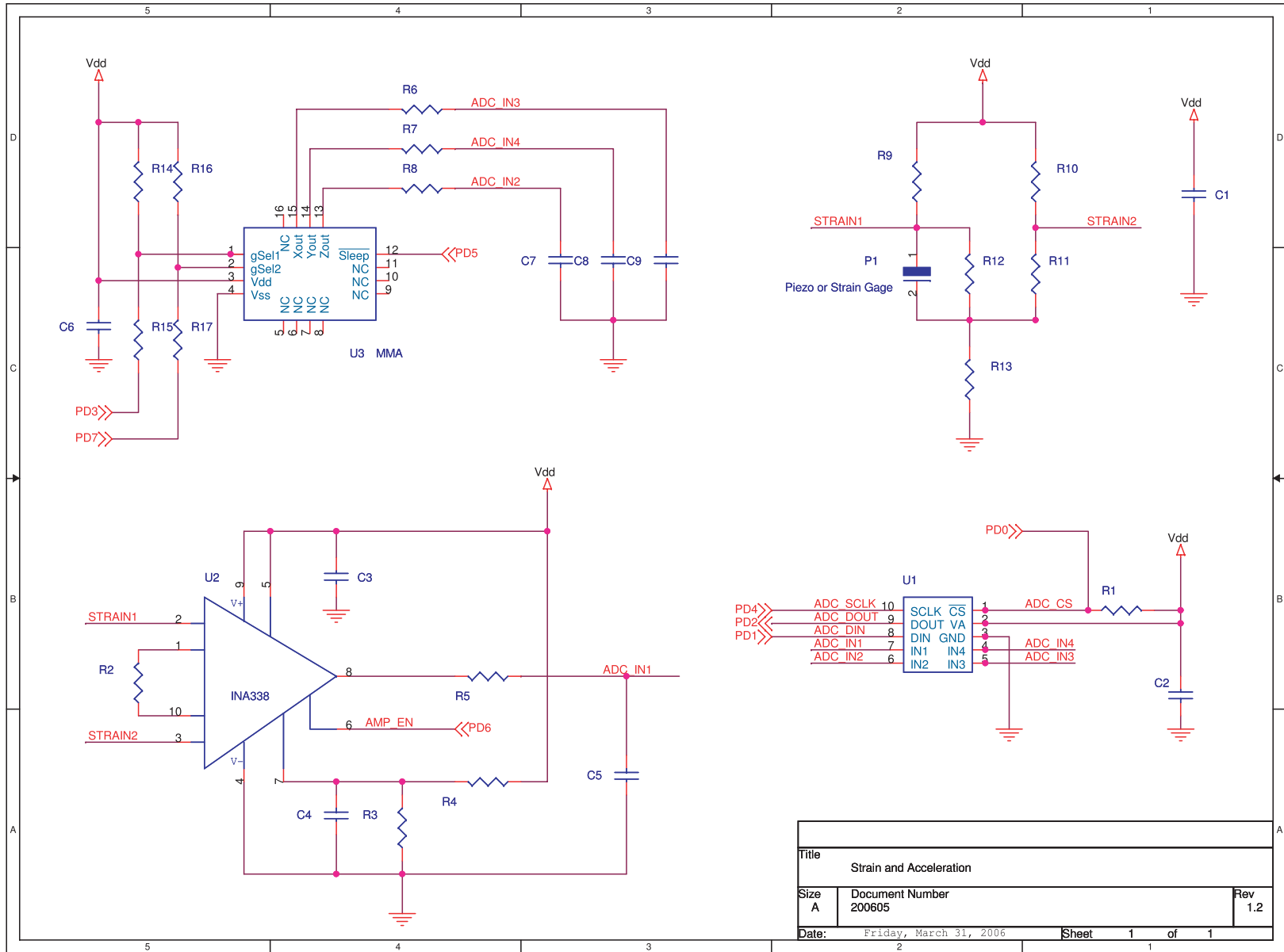


Title		
Power support		
Size	Document Number	Rev
A	200603	1.2
Date:	Friday, March 31, 2006	Sheet 2 of 3

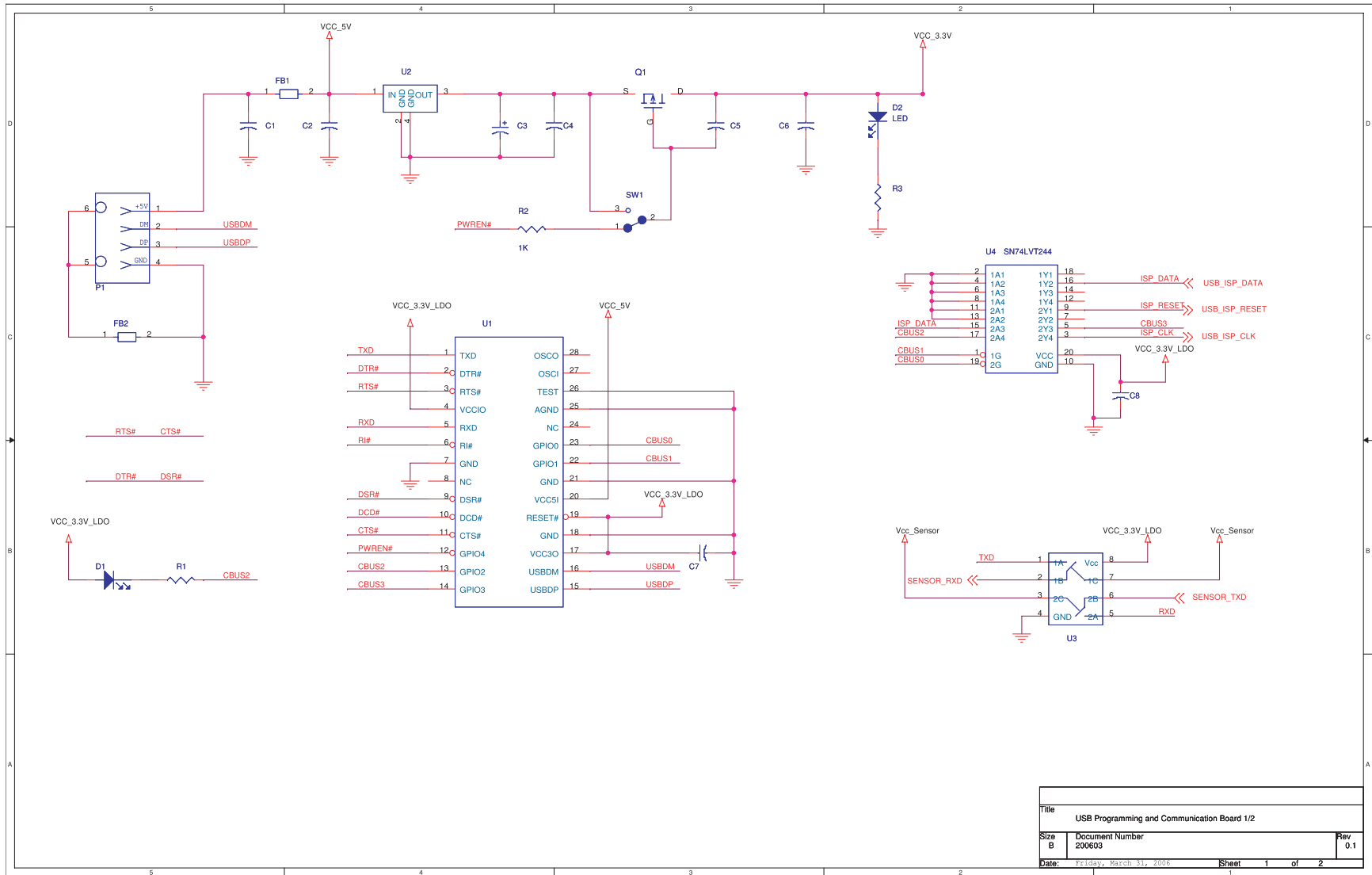
Charge Amp

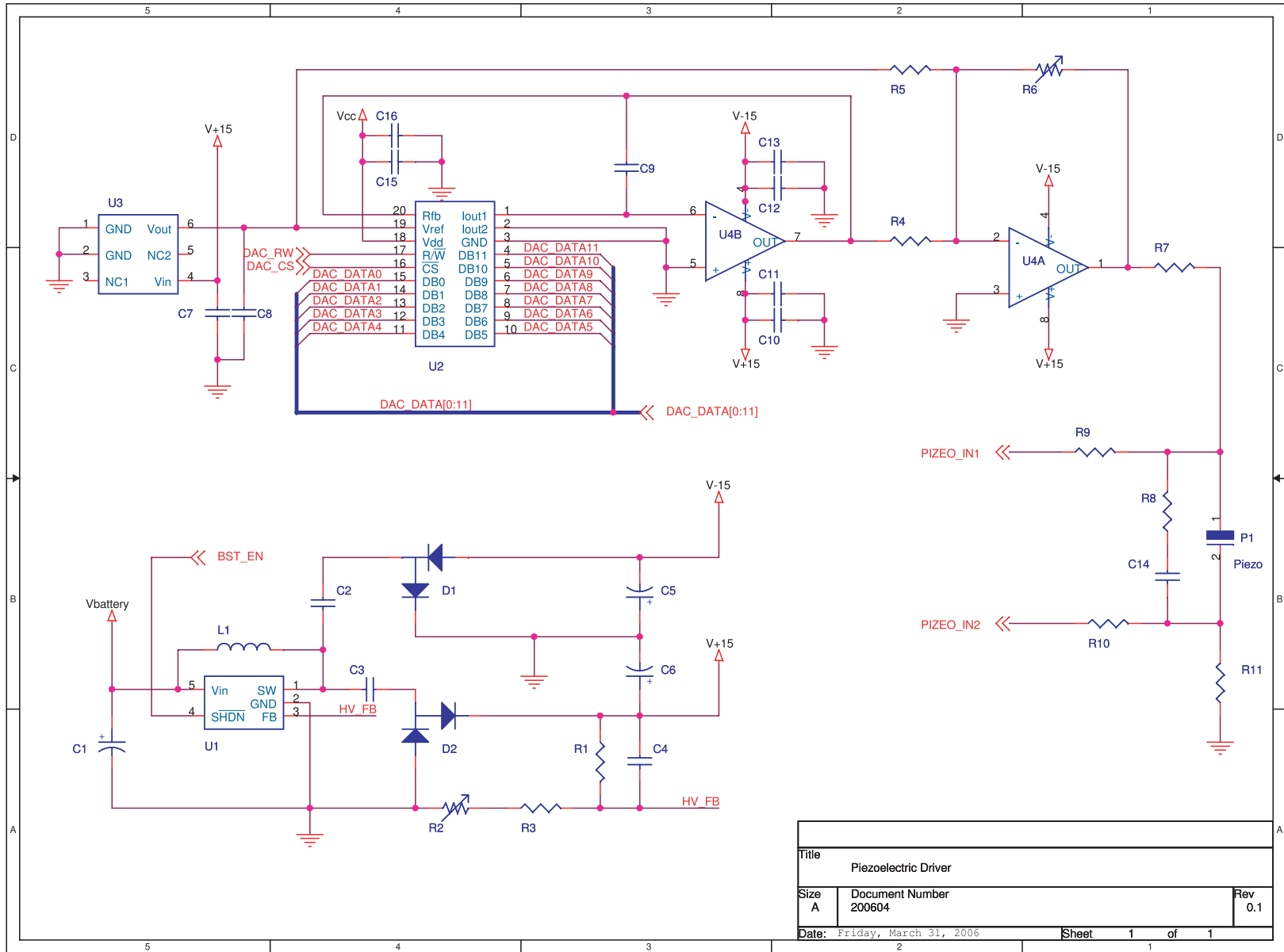


Title		
ChargeAmp and Switches		
Size	Document Number	Rev
B	200603	1.2
Date:	Friday, March 31, 2006	Sheet 1 of 2



Title		
Strain and Acceleration		
Size	Document Number	Rev
A	200605	1.2
Date:	Friday, March 31, 2006	Sheet 1 of 1





Title		
Piezoelectric Driver		
Size	Document Number	Rev
A	200604	0.1
Date:	Friday, March 31, 2006	Sheet 1 of 1

Appendix B: VHDL Code for the FPGA core

```

-----
-- File Name: Wisp.vhd
-----

LIBRARY IEEE;
USE IEEE.std_logic_1164.ALL;

library exemplar ;
use exemplar.exemplar.all ;

PACKAGE WISP IS
    CONSTANT CONSTANT_IDB_WIDTH: INTEGER:=8 ; -- Internal Data Bus Width
    CONSTANT CONSTANT_EDB_WIDTH: INTEGER:=16 ; -- External Data Bus Width
    CONSTANT CONSTANT_IAB_WIDTH: INTEGER:=16 ; -- External Address Bus Width
    CONSTANT CONSTANT_EAB_WIDTH: INTEGER:=18 ; -- External Address Bus Width

    TYPE TYPE_COMMAND IS (T_CMD_NONE,T_CMD_SAMPLE, T_CMD_READ,
    T_CMD_WRITE) ;
    -- ATTRIBUTE TYPE_ENCODING_STYLE OF TYPE_COMMAND: TYPE IS BINARY ;
    -- ATTRIBUTE TYPE_ENCODING OF TYPE_COMMAND :TYPE IS ("11","00","01","10");

    TYPE TYPE_CLOCK_SRC IS (T_CLK_NONE,T_CLK_EGCK,T_CLK_AVR,T_CLK_TOSC) ;
    -- ATTRIBUTE TYPE_ENCODING_STYLE OF TYPE_CLOCK_SRC: TYPE IS BINARY ;
    -- ATTRIBUTE TYPE_ENCODING OF TYPE_CLOCK_SRC :TYPE IS ("11","00","01","10");

    TYPE TYPE_STATE IS (T_STATE_IDLE,

T_STATE_GETTEXTADDRESS1,T_STATE_GETTEXTADDRESS2,T_STATE_GETTEXTADDRESS3,
T_STATE_GETTEXTADDRESS4,T_STATE_GETTEXTADDRESS5,T_STATE_GETTEXTADDRESS6,
    T_STATE_GETINTADDRESS1,T_STATE_GETINTADDRESS2,
    T_STATE_GETINTADDRESS3,T_STATE_GETINTADDRESS4,
    T_STATE_PRERW1,T_STATE_PRERW2,
    T_STATE_RW1,T_STATE_RW2,
    T_STATE_PRESAMPLE1,T_STATE_PRESAMPLE2,
    T_STATE_SAMPLE1,T_STATE_SAMPLE2,T_STATE_SAMPLE3,T_STATE_SAMPLE4,
    T_STATE_SAMPLES,T_STATE_SAMPLE6,T_STATE_SAMPLE7,T_STATE_SAMPLES,
    T_STATE_DONE);
    -- ATTRIBUTE TYPE_ENCODING_STYLE OF TYPE_STATE: TYPE IS GRAY ;
    -- ATTRIBUTE TYPE_ENCODING OF TYPE_STATE :TYPE IS (
    -- "00000",
    -- "00001","00011","00010","00110","00111","00101",
    -- "01101","01100",
    -- "01110","01111","01011","01001","01000","01010","11010","11110",
    -- "110101","10111","10110","10100","10101","10001","10011",
    -- "10000");
END PACKAGE WISP;

-----
-- File Name: MainController.vhd
-----

LIBRARY ieee ;
USE ieee.std_logic_1164.all;

LIBRARY work;
USE work.wisp.all ;

ENTITY MAIN_CONTROLLER IS
    PORT(
        CLOCK: IN std_logic ; -- Global clock
        RESET: IN std_logic; -- Global RESET signal
        IADDRC_RCO: IN std_logic; -- Internal address controller overflows
        EADDRC_RCO: IN std_logic; -- External address controller overflows
        COMMAND: IN TYPE_COMMAND ;-- Command from the microcontroller
        COMMANDDONE: OUT std_logic; -- Command done signal

        IADDRC_LOADB1: OUT std_logic ; -- Internal SRAM address controller begin register load
        IADDRC_LOADB2: OUT std_logic ; -- Internal SRAM address controller begin register load
        IADDRC_LOADE1: OUT std_logic ; -- Internal SRAM address controller end register load
        IADDRC_LOADE2: OUT std_logic ; -- Internal SRAM address controller end register load
        IADDRC_LOAD : OUT std_logic ; -- Internal SRAM address controller load whole
        IADDRC_OE : OUT std_logic ; -- Internal SRAM address controller output enable
        IADDRC_INCE : OUT std_logic ; -- Internal SRAM address controller increment enable

        EADDRC_LOADB1: OUT std_logic ; -- External SRAM address controller begin register load 1
        EADDRC_LOADB2: OUT std_logic ; -- External SRAM address controller begin register load 2
        EADDRC_LOADB3: OUT std_logic ; -- External SRAM address controller begin register load 3
        EADDRC_LOADE1: OUT std_logic ; -- External SRAM address controller end register load 1
        EADDRC_LOADE2: OUT std_logic ; -- External SRAM address controller end register load 2
        EADDRC_LOADE3: OUT std_logic ; -- External SRAM address controller end register load 3
        EADDRC_LOAD : OUT std_logic ; -- External SRAM address controller load whole
        EADDRC_OE : OUT std_logic ; -- External SRAM address controller output enable
        EADDRC_INCE : OUT std_logic ; -- External SRAM address controller increment enable

        ISRAM_WE: OUT std_logic; -- Internal SRAM Write Enable, (WEA)
        ISRAM_DATA_IN: IN std_logic_vector(7 DOWNTO 0); -- Internal SRAM data out,
        (MDINA7~MDINA0)
        ISRAM_DATA_OUT: OUT std_logic_vector(7 DOWNTO 0); -- Internal SRAM data in,
        (MDOUTA7~MDOUTA0)
        ISRAM_ADDR: OUT std_logic_vector(15 DOWNTO 0); -- Internal SRAM address,
        (MADDDRA15~MADDDRA0)

        ESRAM_DATA: INOUT std_logic_vector(15 DOWNTO 0); -- External SRAM data bus
        ESRAM_OE: OUT std_logic; -- External SRAM control OE
        ESRAM_CE1: OUT std_logic; -- External SRAM control CE1
        ESRAM_CE2: OUT std_logic; -- External SRAM control CE2
        ESRAM_RW: OUT std_logic; -- External SRAM control WE
        -- External ADC signal

        ADC_DATA: IN std_logic_vector(9 DOWNTO 0); -- External ADC data
        ADC_EN: OUT std_logic -- External ADC standby
    );
END MAIN_CONTROLLER ;

ARCHITECTURE behaviour OF MAIN_CONTROLLER IS
    SIGNAL current_state: TYPE_STATE ;
    SIGNAL next_state: TYPE_STATE ;
    SIGNAL shift_reg : std_logic_vector(23 DOWNTO 0) := "000000000000000000000000";
    SIGNAL adc_disable : std_logic ;
    SIGNAL esram_we_tmp : std_logic ;
    SIGNAL iaddr_oe_tmp : std_logic ;
    SIGNAL eaddr_oe_tmp : std_logic ;
    SIGNAL temp_buf : std_logic_vector(7 DOWNTO 0) ;
BEGIN
    MAIN_DAEMON: PROCESS(clock,reset)
    BEGIN
        IF (reset='1') THEN
            current_state <= T_STATE_IDLE;
        ELSIF (clock='1' AND clock'EVENT) THEN
            IF (command/=T_CMD_NONE AND current_state=T_STATE_IDLE) THEN
                current_state <= T_STATE_GETTEXTADDRESS1 ;
            ELSE
                current_state <= next_state AFTER 4 ns ;
            END IF ;
        END IF ;
    END PROCESS MAIN_DAEMON ;

    ADDRLOAD: PROCESS(clock)
    BEGIN
        -- Default value for the internal SRAM address control signal
        IADDRC_LOADB1 <= '0' ;
        IADDRC_LOADB2 <= '0' ;
        IADDRC_LOADE1 <= '0' ;
        IADDRC_LOADE2 <= '0' ;
        -- Default value for the external SRAM address control signal
        EADDRC_LOADB1 <= '0' ;
        EADDRC_LOADB2 <= '0' ;
        EADDRC_LOADB3 <= '0' ;
        EADDRC_LOADE1 <= '0' ;
        EADDRC_LOADE2 <= '0' ;
        EADDRC_LOADE3 <= '0' ;
        IF (clock='0' AND clock'EVENT) THEN
            CASE current_state IS
                WHEN T_STATE_GETTEXTADDRESS1 =>
                    EADDRC_LOADB1 <= '1' ;
                WHEN T_STATE_GETTEXTADDRESS2 =>
                    EADDRC_LOADB2 <= '1' ;
                WHEN T_STATE_GETTEXTADDRESS3 =>
                    EADDRC_LOADB3 <= '1' ;
                WHEN T_STATE_GETTEXTADDRESS4 =>
                    EADDRC_LOADE1 <= '1' ;
                WHEN T_STATE_GETTEXTADDRESS5 =>
                    EADDRC_LOADE2 <= '1' ;
                WHEN T_STATE_GETTEXTADDRESS6 =>
                    EADDRC_LOADE3 <= '1' ;
                WHEN T_STATE_GETINTADDRESS1 =>
                    IADDRC_LOADB1 <= '1' ;
                WHEN T_STATE_GETINTADDRESS2 =>
                    IADDRC_LOADB2 <= '1' ;
                WHEN T_STATE_GETINTADDRESS3 =>
                    IADDRC_LOADE1 <= '1' ;
                WHEN T_STATE_GETINTADDRESS4 =>
                    IADDRC_LOADE2 <= '1' ;
                WHEN OTHERS =>
                    END CASE ;
            END IF ;
        END PROCESS;

        STATEMAC: PROCESS(current_state,iaddr_rco,eaddr_rco)
        VARIABLE temp_reg : std_logic_vector(23 DOWNTO 0);
        BEGIN
            -- Default value for the internal SRAM address control signal
            IADDRC_LOAD <= '0' ;
            iaddr_oe_tmp <= '0' ;
            IADDRC_INCE <= '0' ;
            -- Default value for the external SRAM address control signal
            EADDRC_LOAD <= '0' ;
            eaddr_oe_tmp <= '0' ;
            EADDRC_INCE <= '0' ;
            COMMANDDONE <= '0' ;
            -- Default value for the internal SRAM control signal
            ISRAM_WE <= '0' ;
            ISRAM_ADDR <= "0011111111100010" ; -- SRAM address 0x3FE2
            ISRAM_DATA_OUT <= "XXXXXXXXX" ;
            -- Default value for the external SRAM control signal: activated but non-IO
            -- We have to enable CE while not in IDLE mode to let the combinational avoid glitch
            ESRAM_CE1 <= '0' ;
            ESRAM_CE2 <= '1' ;
            esram_we_tmp <= '1' ;
            -- Default in ESRAM write mode
            -- Please note the DATA is usually HighZ since CE and WE is enabled during initial status
            ESRAM_DATA <= "ZZZZZZZZZZZZZZ";
            -- Default value for the external ADC control signal: deactivated
            adc_disable <= '1' ;
        END STATEMAC;
    END ARCHITECTURE;

```

```

-----
-- File Name: Wisp.vhd
-----

LIBRARY IEEE;
USE IEEE.std_logic_1164.ALL;

library exemplar ;
use exemplar.exemplar.all ;

PACKAGE WISP IS
    CONSTANT CONSTANT_IDB_WIDTH: INTEGER:=8 ; -- Internal Data Bus Width
    CONSTANT CONSTANT_EDB_WIDTH: INTEGER:=16 ; -- External Data Bus Width
    CONSTANT CONSTANT_IAB_WIDTH: INTEGER:=16 ; -- External Address Bus Width
    CONSTANT CONSTANT_EAB_WIDTH: INTEGER:=18 ; -- External Address Bus Width

    TYPE TYPE_COMMAND IS (T_CMD_NONE,T_CMD_SAMPLE,T_CMD_READ,
T_CMD_WRITE) ;
-- ATTRIBUTE TYPE_ENCODING_STYLE OF TYPE_COMMAND: TYPE IS BINARY ;
-- ATTRIBUTE TYPE_ENCODING OF TYPE_COMMAND :TYPE IS ("11","00","01","10");

    TYPE TYPE_CLOCK_SRC IS (T_CLK_NONE,T_CLK_EGCK,T_CLK_AVR,T_CLK_TOSC) ;
-- ATTRIBUTE TYPE_ENCODING_STYLE OF TYPE_CLOCK_SRC: TYPE IS BINARY ;
-- ATTRIBUTE TYPE_ENCODING OF TYPE_CLOCK_SRC :TYPE IS ("11","00","01","10");

    TYPE TYPE_STATE IS (T_STATE_IDLE,

T_STATE_GETTEXTADDRESS1,T_STATE_GETTEXTADDRESS2,T_STATE_GETTEXTADDRESS3,
T_STATE_GETTEXTADDRESS4,T_STATE_GETTEXTADDRESS5,T_STATE_GETTEXTADDRESS6,
T_STATE_GETINTADDRESS1,T_STATE_GETINTADDRESS2,
T_STATE_GETINTADDRESS3,T_STATE_GETINTADDRESS4,
T_STATE_PRERW1,T_STATE_PRERW2,
T_STATE_RW1,T_STATE_RW2,
T_STATE_PRESAMPLE1,T_STATE_PRESAMPLE2,
T_STATE_SAMPLE1,T_STATE_SAMPLE2,T_STATE_SAMPLE3,T_STATE_SAMPLE4,
T_STATE_SAMPLES,T_STATE_SAMPLE6,T_STATE_SAMPLE7,T_STATE_SAMPLE8,
T_STATE_DONE);
-- ATTRIBUTE TYPE_ENCODING_STYLE OF TYPE_STATE: TYPE IS GRAY ;
-- ATTRIBUTE TYPE_ENCODING OF TYPE_STATE :TYPE IS (
-- "00000",
-- "00001","00011","0010","00110","00111","00101",
-- "01101","01100",
-- "01110","01111","01011","01001","01000","01010","11010","11110",
-- "10101","10111","10110","10100","10101","10001","10011",
-- "10000");
END PACKAGE WISP;

-----
-- File Name: MainController.vhd
-----

LIBRARY ieee ;
USE ieee.std_logic_1164.all;

LIBRARY work;
USE work.wisp.all ;

ENTITY MAIN_CONTROLLER IS
PORT(
    CLOCK: IN std_logic ; -- Global clock
    RESET: IN std_logic; -- Global RESET signal
    IADDRC_RCO: IN std_logic; -- Internal address controller overflows
    EADDRC_RCO: IN std_logic; -- External address controller overflows
    COMMAND: IN TYPE_COMMAND ;-- Command from the microcontroller
    COMMANDDONE: OUT std_logic; -- Command done signal

    IADDRC_LOADB1: OUT std_logic ; -- Internal SRAM address controller begin register load
    IADDRC_LOADB2: OUT std_logic ; -- Internal SRAM address controller begin register load
    IADDRC_LOADE1: OUT std_logic ; -- Internal SRAM address controller end register load
    IADDRC_LOADE2: OUT std_logic ; -- Internal SRAM address controller end register load
    IADDRC_LOAD : OUT std_logic ; -- Internal SRAM address controller load whole
    IADDRC_OE : OUT std_logic ; -- Internal SRAM address controller output enable
    IADDRC_INCE : OUT std_logic ; -- Internal SRAM address controller increment enable

    EADDRC_LOADB1: OUT std_logic ; -- External SRAM address controller begin register load 1
    EADDRC_LOADB2: OUT std_logic ; -- External SRAM address controller begin register load 2
    EADDRC_LOADB3: OUT std_logic ; -- External SRAM address controller begin register load 3
    EADDRC_LOADE1: OUT std_logic ; -- External SRAM address controller end register load 1
    EADDRC_LOADE2: OUT std_logic ; -- External SRAM address controller end register load 2
    EADDRC_LOADE3: OUT std_logic ; -- External SRAM address controller end register load 3
    EADDRC_LOAD : OUT std_logic ; -- External SRAM address controller load whole
    EADDRC_OE : OUT std_logic ; -- External SRAM address controller output enable
    EADDRC_INCE : OUT std_logic ; -- External SRAM address controller increment enable

    ISRAM_WE: OUT std_logic; -- Internal SRAM Write Enable, (WEA)
    ISRAM_DATA_IN: IN std_logic_vector(7 DOWNTO 0); -- Internal SRAM data out,
(MDINA7~MDINA0)
    ISRAM_DATA_OUT: OUT std_logic_vector(7 DOWNTO 0); -- Internal SRAM data in,
(MDOUTA7~MDOUTA0)
    ISRAM_ADDR: OUT std_logic_vector(15 DOWNTO 0); -- Internal SRAM address,
(MADDRA15~MADDRA0)

    ESRAM_DATA: INOUT std_logic_vector(15 DOWNTO 0); -- External SRAM data bus
    ESRAM_OE: OUT std_logic; -- External SRAM control OE
    ESRAM_CE1: OUT std_logic; -- External SRAM control CE1
    ESRAM_CE2: OUT std_logic; -- External SRAM control CE2
    ESRAM_RW: OUT std_logic; -- External SRAM control WE
-- External ADC signal

    ADC_DATA: IN std_logic_vector(9 DOWNTO 0); -- External ADC data
    ADC_EN: OUT std_logic -- External ADC standby
);

END MAIN_CONTROLLER ;

ARCHITECTURE behaviour OF MAIN_CONTROLLER IS
    SIGNAL current_state: TYPE_STATE ;
    SIGNAL next_state: TYPE_STATE ;
    SIGNAL shift_reg :std_logic_vector(23 DOWNTO 0) := "000000000000000000000000";
    SIGNAL adc_disable : std_logic ;
    SIGNAL esram_we_tmp : std_logic ;
    SIGNAL iaddrc_oe_tmp : std_logic ;
    SIGNAL eaddrc_oe_tmp : std_logic ;
    SIGNAL temp_buf : std_logic_vector(7 DOWNTO 0) ;
BEGIN

    MAIN_DAEMON: PROCESS(clock,reset)
    BEGIN
        IF (reset='1') THEN
            current_state <= T_STATE_IDLE;
        ELSIF (clock='1' AND clock'EVENT) THEN
            IF (command/=T_CMD_NONE AND current_state=T_STATE_IDLE) THEN
                current_state <= T_STATE_GETTEXTADDRESS1 ;
            ELSE
                current_state <= next_state AFTER 4 ns ;
            END IF ;
        END IF ;
    END PROCESS MAIN_DAEMON ;

    ADDRLOAD: PROCESS(clock)
    BEGIN
        -- Default value for the internal SRAM address control signal
        IADDRC_LOADB1 <= '0';
        IADDRC_LOADB2 <= '0';
        IADDRC_LOADB3 <= '0';
        IADDRC_LOADE1 <= '0';
        IADDRC_LOADE2 <= '0';
        -- Default value for the external SRAM address control signal
        EADDRC_LOADB1 <= '0';
        EADDRC_LOADB2 <= '0';
        EADDRC_LOADB3 <= '0';
        EADDRC_LOADE1 <= '0';
        EADDRC_LOADE2 <= '0';
        EADDRC_LOADE3 <= '0';
        IF (clock='0' AND clock'EVENT) THEN
            CASE current_state IS
                WHEN T_STATE_GETTEXTADDRESS1 =>
                    EADDRC_LOADB1 <= '1' ;
                WHEN T_STATE_GETTEXTADDRESS2 =>
                    EADDRC_LOADB2 <= '1' ;
                WHEN T_STATE_GETTEXTADDRESS3 =>
                    EADDRC_LOADB3 <= '1' ;
                WHEN T_STATE_GETTEXTADDRESS4 =>
                    EADDRC_LOADE1 <= '1' ;
                WHEN T_STATE_GETTEXTADDRESS5 =>
                    EADDRC_LOADE2 <= '1' ;
                WHEN T_STATE_GETTEXTADDRESS6 =>
                    EADDRC_LOADE3 <= '1' ;
                WHEN T_STATE_GETINTADDRESS1 =>
                    IADDRC_LOADB1 <= '1';
                WHEN T_STATE_GETINTADDRESS2 =>
                    IADDRC_LOADB2 <= '1';
                WHEN T_STATE_GETINTADDRESS3 =>
                    IADDRC_LOADE1 <= '1';
                WHEN T_STATE_GETINTADDRESS4 =>
                    IADDRC_LOADE2 <= '1';
                WHEN OTHERS =>
                    END CASE ;
            END IF ;
        END PROCESS;

    STATEMAC: PROCESS(current_state,iaddrc_rco,eaddrc_rco)
    VARIABLE temp_reg : std_logic_vector(23 DOWNTO 0);
    BEGIN
        -- Default value for the internal SRAM address control signal
        IADDRC_LOAD <= '0';
        iaddrc_oe_tmp <= '0';
        IADDRC_INCE <= '0';

        -- Default value for the external SRAM address control signal
        EADDRC_LOAD <= '0';
        eaddrc_oe_tmp <= '0';
        EADDRC_INCE <= '0';

        COMMANDDONE <= '0';

        -- Default value for the internal SRAM control signal
        ISRAM_WE <= '0';
        ISRAM_ADDR <= "001111111100010"; -- SRAM address 0x3FE2
        ISRAM_DATA_OUT <= "XXXXXXXX";

        -- Default value for the external SRAM control signal: activated but non-IO
        ESRAM_CE1 <= '0';
        ESRAM_CE2 <= '1';
        esram_we_tmp <= '1';

        -- Default in ESRAM write mode
        -- Please note the DATA is usually HighZ since CE and WE is enabled during initial status
        ESRAM_DATA <= "ZZZZZZZZ";
        -- Default value for the external ADC control signal: deactivated
        adc_disable <= '1';
    END PROCESS;

```

```

-- Shifter for the sampling
temp_reg(23 DOWNTO 10) := shift_reg(13 DOWNTO 0);
temp_reg(9 DOWNTO 0) := ADC_DATA;
shift_reg <= temp_reg;

CASE current_state IS
WHEN T_STATE_IDLE =>
-- Do nothing
ESRAM_CEI <= '1';
ESRAM_CE2 <= '0';
next_state <= T_STATE_IDLE;
-- Load Begin Address for the external SRAM from the internal SRAM
WHEN T_STATE_GETTEXTADDRESS1 =>
ISRAM_ADDR <= "001111111100011"; -- SRAM address 0x3FE3
next_state <= T_STATE_GETTEXTADDRESS2;
WHEN T_STATE_GETTEXTADDRESS2 =>
ISRAM_ADDR <= "001111111100100"; -- Read the internal SRAM address 0x3FE4
next_state <= T_STATE_GETTEXTADDRESS3;
WHEN T_STATE_GETTEXTADDRESS3 =>
ISRAM_ADDR <= "001111111100110"; -- SRAM address 0x3FE6
next_state <= T_STATE_GETTEXTADDRESS4;
-- Load End Address for the external SRAM from the internal SRAM
WHEN T_STATE_GETTEXTADDRESS4 =>
ISRAM_ADDR <= "001111111100111"; -- SRAM address 0x3FE7
next_state <= T_STATE_GETTEXTADDRESS5;
WHEN T_STATE_GETTEXTADDRESS5 =>
ISRAM_ADDR <= "001111111101000"; -- SRAM address 0x3FE8
next_state <= T_STATE_GETTEXTADDRESS6;
WHEN T_STATE_GETTEXTADDRESS6 =>
ISRAM_ADDR <= "001111111101010"; -- Prefetch SRAM address 0x3FEA : begin address
of the internal SRAM address.
-- Proceed to next status: Load internal SRAM address or start command
CASE command IS
WHEN T_CMD_SAMPLE =>
next_state <= T_STATE_PRESAMPLE1;
WHEN T_CMD_READ | T_CMD_WRITE =>
next_state <= T_STATE_GETINTADDRESS1;
WHEN T_CMD_NONE =>
next_state <= T_STATE_DONE;
END CASE;
WHEN T_STATE_GETINTADDRESS1 =>
ISRAM_ADDR <= "001111111101011"; -- SRAM address 0x3FEB
next_state <= T_STATE_GETINTADDRESS2;
WHEN T_STATE_GETINTADDRESS2 =>
ISRAM_ADDR <= "001111111101100"; -- SRAM address 0x3FEC
next_state <= T_STATE_GETINTADDRESS3;
-- Load End Address for the internal SRAM from the internal SRAM
WHEN T_STATE_GETINTADDRESS3 =>
ISRAM_ADDR <= "001111111101101"; -- SRAM address 0x3FED
next_state <= T_STATE_GETINTADDRESS4;
WHEN T_STATE_GETINTADDRESS4 =>
next_state <= T_STATE_PRERW1;
WHEN T_STATE_PRERW1 =>
-- load address counters
EADDR_LOAD <= '1';
IADDR_LOAD <= '1';
next_state <= T_STATE_PRERW2;
WHEN T_STATE_PRERW2 =>
-- Enable outputs of the address controllers
iaddr_oe_tmp <= '1';
eaddr_oe_tmp <= '1';
next_state <= T_STATE_RW1;
WHEN T_STATE_RW1 =>
-- Enable outputs of the address controllers
iaddr_oe_tmp <= '1';
eaddr_oe_tmp <= '1';
CASE command IS
WHEN T_CMD_READ =>
-- Set the external SRAM in read mode
ISRAM_WE <= '1';
ISRAM_DATA_OUT <= ESRAM_DATA(7 DOWNTO 0);
WHEN T_CMD_WRITE =>
esram_we_tmp <= '0';
ESRAM_DATA(7 DOWNTO 0) <= ISRAM_DATA_IN;
temp_buf <= ISRAM_DATA_IN;
WHEN OTHERS =>
END CASE;
-- Increase the internal SRAM address only
IADDR_INCE <= '1';
next_state <= T_STATE_RW2;
WHEN T_STATE_RW2 =>
-- Enable outputs of the address controllers
iaddr_oe_tmp <= '1';
eaddr_oe_tmp <= '1';
CASE command IS
WHEN T_CMD_READ =>
-- Set the external SRAM in read mode
ISRAM_WE <= '1';
ISRAM_DATA_OUT <= ESRAM_DATA(15 DOWNTO 8);
WHEN T_CMD_WRITE =>
esram_we_tmp <= '0';
ESRAM_DATA(15 DOWNTO 8) <= ISRAM_DATA_IN;
ESRAM_DATA(7 DOWNTO 0) <= temp_buf;
WHEN OTHERS =>
END CASE;
-- Increase both addresses
IADDR_INCE <= '1';
EADDR_INCE <= '1';
next_state <= T_STATE_RW1;
WHEN T_STATE_PRESAMPLE1 =>
-- Activate the external ADC
adc_disable <= '0';
-- Load the external address counter
EADDR_LOAD <= '1';
next_state <= T_STATE_SAMPLE1;
WHEN T_STATE_PRESAMPLE2 =>
-- Wait for ADC stable
-- Activate the external ADC
adc_disable <= '0';
esram_we_tmp <= '0';
eaddr_oe_tmp <= '1';
next_state <= T_STATE_SAMPLE1;
WHEN T_STATE_SAMPLE1 =>
-- Activate the external ADC
adc_disable <= '0';
esram_we_tmp <= '0';
-- Enable the output of the external SRAM address controller
eaddr_oe_tmp <= '1';
next_state <= T_STATE_SAMPLE2;
WHEN T_STATE_SAMPLE2 =>
-- Activate the external ADC
adc_disable <= '0';
esram_we_tmp <= '0';
-- Write the external SRAM
ESRAM_DATA <= temp_reg(19 DOWNTO 4);
-- Increase the address of the external SRAM
EADDR_INCE <= '1';
-- Enable the output of the external SRAM address controller
eaddr_oe_tmp <= '1';
next_state <= T_STATE_SAMPLE3;
WHEN T_STATE_SAMPLE3 =>
-- Activate the external ADC
adc_disable <= '0';
esram_we_tmp <= '0';
-- Enable the output of the external SRAM address controller
eaddr_oe_tmp <= '1';
next_state <= T_STATE_SAMPLE4;
WHEN T_STATE_SAMPLE4 =>
-- Activate the external ADC
adc_disable <= '0';
esram_we_tmp <= '0';
-- Write the external SRAM
ESRAM_DATA <= temp_reg(23 DOWNTO 8);
-- Increase the address of the external SRAM
EADDR_INCE <= '1';
-- Enable the output of the external SRAM address controller
eaddr_oe_tmp <= '1';
next_state <= T_STATE_SAMPLE5;
WHEN T_STATE_SAMPLE5 =>
-- Activate the external ADC
adc_disable <= '0';
esram_we_tmp <= '0';
-- Write the external SRAM
ESRAM_DATA <= temp_reg(17 DOWNTO 2);
-- Increase the address of the external SRAM
EADDR_INCE <= '1';
-- Enable the output of the external SRAM address controller
eaddr_oe_tmp <= '1';
next_state <= T_STATE_SAMPLE6;
WHEN T_STATE_SAMPLE6 =>
-- Activate the external ADC
adc_disable <= '0';
esram_we_tmp <= '0';
-- Enable the output of the external SRAM address controller
eaddr_oe_tmp <= '1';
next_state <= T_STATE_SAMPLE7;
WHEN T_STATE_SAMPLE7 =>
-- Activate the external ADC
adc_disable <= '0';
esram_we_tmp <= '0';
-- Write the external SRAM
ESRAM_DATA <= temp_reg(21 DOWNTO 6);
-- Increase the address of the external SRAM
EADDR_INCE <= '1';
-- Enable the output of the external SRAM address controller
eaddr_oe_tmp <= '1';
next_state <= T_STATE_SAMPLE8;
WHEN T_STATE_SAMPLE8 =>
-- Activate the external ADC
adc_disable <= '0';
esram_we_tmp <= '0';
-- Write the external SRAM
ESRAM_DATA <= temp_reg(15 DOWNTO 0);
-- Increase the address of the external SRAM
EADDR_INCE <= '1';
-- Enable the output of the external SRAM address controller
eaddr_oe_tmp <= '1';
next_state <= T_STATE_SAMPLE1;
-- Load Begin Address for the internal SRAM from the internal SRAM
WHEN T_STATE_DONE =>
-- Write result to the internal SRAM
COMMANDDONE <= '1';
-- No status transition here
next_state <= T_STATE_DONE;
END CASE;
IF (iaddr_rco='1' OR eaddr_rco='1') AND current_state/=T_STATE_DONE THEN
COMMANDDONE <= '1';
next_state <= T_STATE_DONE;
ASSERT (current_state/=T_STATE_IDLE)
REPORT "Address counter overflows while no operation."
SEVERITY ERROR;
END IF;
END PROCESS STATEMAC;

```

```

-- Shifter for the sampling
temp_reg(23 DOWNTO 10) := shift_reg(13 DOWNTO 0);
temp_reg(9 DOWNTO 0) := ADC_DATA;
shift_reg <= temp_reg;

CASE current_state IS
WHEN T_STATE_IDLE =>
-- Do nothing
ESRAM_CEI <= '1';
ESRAM_CE2 <= '0';
next_state <= T_STATE_IDLE;
-- Load Begin Address for the external SRAM from the internal SRAM
WHEN T_STATE_GETTEXTADDRESS1 =>
ISRAM_ADDR <= "001111111100011"; -- SRAM address 0x3FE3
next_state <= T_STATE_GETTEXTADDRESS2;
WHEN T_STATE_GETTEXTADDRESS2 =>
ISRAM_ADDR <= "001111111100100"; -- Read the internal SRAM address 0x3FE4
next_state <= T_STATE_GETTEXTADDRESS3;
WHEN T_STATE_GETTEXTADDRESS3 =>
ISRAM_ADDR <= "001111111100110"; -- SRAM address 0x3FE6
next_state <= T_STATE_GETTEXTADDRESS4;
-- Load End Address for the external SRAM from the internal SRAM
WHEN T_STATE_GETTEXTADDRESS4 =>
ISRAM_ADDR <= "001111111100111"; -- SRAM address 0x3FE7
next_state <= T_STATE_GETTEXTADDRESS5;
WHEN T_STATE_GETTEXTADDRESS5 =>
ISRAM_ADDR <= "001111111101000"; -- SRAM address 0x3FE8
next_state <= T_STATE_GETTEXTADDRESS6;
WHEN T_STATE_GETTEXTADDRESS6 =>
ISRAM_ADDR <= "001111111101010"; -- Prefetch SRAM address 0x3FEA : begin address
of the internal SRAM address.
-- Proceed to next status: Load internal SRAM address or start command
CASE command IS
WHEN T_CMD_SAMPLE =>
next_state <= T_STATE_PRESAMPLE1;
WHEN T_CMD_READ | T_CMD_WRITE =>
next_state <= T_STATE_GETINTADDRESS1;
WHEN T_CMD_NONE =>
next_state <= T_STATE_DONE;
END CASE;
WHEN T_STATE_GETINTADDRESS1 =>
ISRAM_ADDR <= "001111111101011"; -- SRAM address 0x3FEB
next_state <= T_STATE_GETINTADDRESS2;
WHEN T_STATE_GETINTADDRESS2 =>
ISRAM_ADDR <= "001111111101100"; -- SRAM address 0x3FEC
next_state <= T_STATE_GETINTADDRESS3;
-- Load End Address for the internal SRAM from the internal SRAM
WHEN T_STATE_GETINTADDRESS3 =>
ISRAM_ADDR <= "001111111101101"; -- SRAM address 0x3FED
next_state <= T_STATE_GETINTADDRESS4;
WHEN T_STATE_GETINTADDRESS4 =>
next_state <= T_STATE_PRERW1;
WHEN T_STATE_PRERW1 =>
-- load address counters
EADDR_LOAD <= '1';
IADDR_LOAD <= '1';
next_state <= T_STATE_PRERW2;
WHEN T_STATE_PRERW2 =>
-- Enable outputs of the address controllers
iaddr_oe_tmp <= '1';
eaddr_oe_tmp <= '1';
next_state <= T_STATE_RW1;
WHEN T_STATE_RW1 =>
-- Enable outputs of the address controllers
iaddr_oe_tmp <= '1';
eaddr_oe_tmp <= '1';
CASE command IS
WHEN T_CMD_READ =>
-- Set the external SRAM in read mode
ISRAM_WE <= '1';
ISRAM_DATA_OUT <= ESRAM_DATA(7 DOWNTO 0);
WHEN T_CMD_WRITE =>
esram_we_tmp <= '0';
ESRAM_DATA(7 DOWNTO 0) <= ISRAM_DATA_IN;
temp_buf <= ISRAM_DATA_IN;
WHEN OTHERS =>
END CASE;
-- Increase the internal SRAM address only
IADDR_INCE <= '1';
next_state <= T_STATE_RW2;
WHEN T_STATE_RW2 =>
-- Enable outputs of the address controllers
iaddr_oe_tmp <= '1';
eaddr_oe_tmp <= '1';
CASE command IS
WHEN T_CMD_READ =>
-- Set the external SRAM in read mode
ISRAM_WE <= '1';
ISRAM_DATA_OUT <= ESRAM_DATA(15 DOWNTO 8);
WHEN T_CMD_WRITE =>
esram_we_tmp <= '0';
ESRAM_DATA(15 DOWNTO 8) <= ISRAM_DATA_IN;
ESRAM_DATA(7 DOWNTO 0) <= temp_buf;
WHEN OTHERS =>
END CASE;
-- Increase both addresses
IADDR_INCE <= '1';
EADDR_INCE <= '1';
next_state <= T_STATE_RW1;
WHEN T_STATE_PRESAMPLE1 =>
-- Activate the external ADC
adc_disable <= '0';
-- Load the external address counter
EADDR_LOAD <= '1';
next_state <= T_STATE_SAMPLE1;
WHEN T_STATE_PRESAMPLE2 =>
-- Wait for ADC stable
-- Activate the external ADC
adc_disable <= '0';
esram_we_tmp <= '0';
eaddr_oe_tmp <= '1';
next_state <= T_STATE_SAMPLE1;
WHEN T_STATE_SAMPLE1 =>
-- Activate the external ADC
adc_disable <= '0';
esram_we_tmp <= '0';
-- Enable the output of the external SRAM address controller
eaddr_oe_tmp <= '1';
next_state <= T_STATE_SAMPLE2;
WHEN T_STATE_SAMPLE2 =>
-- Activate the external ADC
adc_disable <= '0';
esram_we_tmp <= '0';
-- Write the external SRAM
ESRAM_DATA <= temp_reg(19 DOWNTO 4);
-- Increase the address of the external SRAM
EADDR_INCE <= '1';
-- Enable the output of the external SRAM address controller
eaddr_oe_tmp <= '1';
next_state <= T_STATE_SAMPLE3;
WHEN T_STATE_SAMPLE3 =>
-- Activate the external ADC
adc_disable <= '0';
esram_we_tmp <= '0';
-- Enable the output of the external SRAM address controller
eaddr_oe_tmp <= '1';
next_state <= T_STATE_SAMPLE4;
WHEN T_STATE_SAMPLE4 =>
-- Activate the external ADC
adc_disable <= '0';
esram_we_tmp <= '0';
-- Write the external SRAM
ESRAM_DATA <= temp_reg(23 DOWNTO 8);
-- Increase the address of the external SRAM
EADDR_INCE <= '1';
-- Enable the output of the external SRAM address controller
eaddr_oe_tmp <= '1';
next_state <= T_STATE_SAMPLE5;
WHEN T_STATE_SAMPLE5 =>
-- Activate the external ADC
adc_disable <= '0';
esram_we_tmp <= '0';
-- Write the external SRAM
ESRAM_DATA <= temp_reg(17 DOWNTO 2);
-- Increase the address of the external SRAM
EADDR_INCE <= '1';
-- Enable the output of the external SRAM address controller
eaddr_oe_tmp <= '1';
next_state <= T_STATE_SAMPLE6;
WHEN T_STATE_SAMPLE6 =>
-- Activate the external ADC
adc_disable <= '0';
esram_we_tmp <= '0';
-- Enable the output of the external SRAM address controller
eaddr_oe_tmp <= '1';
next_state <= T_STATE_SAMPLE7;
WHEN T_STATE_SAMPLE7 =>
-- Activate the external ADC
adc_disable <= '0';
esram_we_tmp <= '0';
-- Write the external SRAM
ESRAM_DATA <= temp_reg(21 DOWNTO 6);
-- Increase the address of the external SRAM
EADDR_INCE <= '1';
-- Enable the output of the external SRAM address controller
eaddr_oe_tmp <= '1';
next_state <= T_STATE_SAMPLE8;
WHEN T_STATE_SAMPLE8 =>
-- Activate the external ADC
adc_disable <= '0';
esram_we_tmp <= '0';
-- Write the external SRAM
ESRAM_DATA <= temp_reg(15 DOWNTO 0);
-- Increase the address of the external SRAM
EADDR_INCE <= '1';
-- Enable the output of the external SRAM address controller
eaddr_oe_tmp <= '1';
next_state <= T_STATE_SAMPLE1;
-- Load Begin Address for the internal SRAM from the internal SRAM
WHEN T_STATE_DONE =>
-- Write result to the internal SRAM
COMMANDDONE <= '1';
-- No status transition here
next_state <= T_STATE_DONE;
END CASE;
IF (iaddr_rco='1' OR eaddr_rco='1') AND current_state/=T_STATE_DONE THEN
COMMANDDONE <= '1';
next_state <= T_STATE_DONE;
ASSERT (current_state/=T_STATE_IDLE)
REPORT "Address counter overflows while no operation."
SEVERITY ERROR;
END IF;
END PROCESS STATEMAC;

```

Appendix C: Analytical Expressions of The Five-peaked Waves

The five-peaked wave is one type of the narrowband waves popularly used in active damage diagnosis. It can be expressed as

$$f(t) = A[H(t) - H(t - \frac{2\pi N_p}{\omega_c})] \left[1 - \cos\left(\frac{\omega_c}{N_p} t\right) \right] e^{i\omega_c t} \quad (C.1)$$

where A is the initial amplitude, $N_p = 5$ is the number of peaks, ω_c is the central frequency and $H(t)$ is the Heaviside step function. From its expression, it can be seen that the five-peaked wave is a synthesized 5-cycle tone-burst signal with its amplitude modulated a cosine function. The waveform and amplitude spectrum in the frequency domain of the five-peaked wave are shown in Figure C.1.

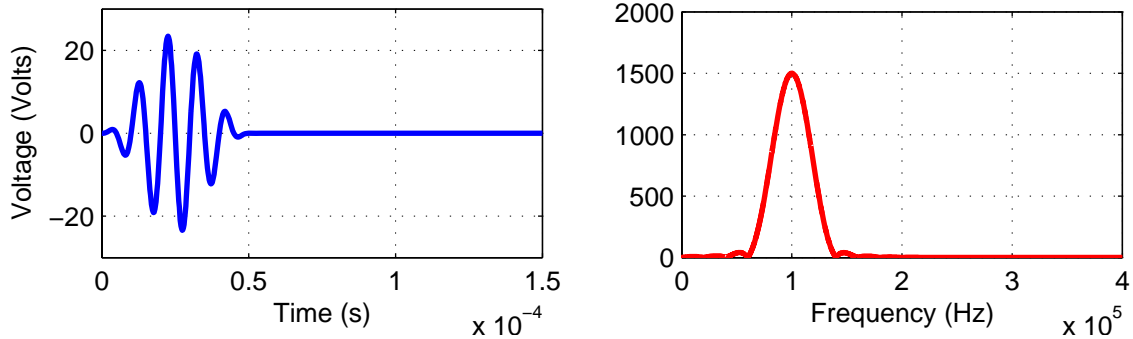


Figure C.1 Waveform and amplitude spectrum of the five-peaked wave

The Fourier transform of $f(t)$ is given by

$$\begin{aligned} F(\omega) &= \int_{-\infty}^{\infty} A[H(t) - H(t - \frac{2\pi N_p}{\omega_c})] \left[1 - \cos\left(\frac{\omega_c}{N_p} t\right) \right] e^{i\omega_c t} e^{-i\omega t} dt \\ &= \int_0^{\frac{2\pi N_p}{\omega_c}} \left[1 - \cos\left(\frac{\omega_c t}{N_p}\right) \right] e^{i(\omega_c - \omega)t} dt \\ &= \frac{e^{at}}{a} \Big|_0^{\frac{2\pi N_p}{\omega_c}} - \int_0^{\frac{2\pi N_p}{\omega_c}} \cos bt e^{at} dt \end{aligned} \quad (C.2)$$

where $a = i(\omega_c - \omega)$ and $b = \omega_c/N_p$. The Eq. (C.2) can be further simplified to

$$F(\omega) = \frac{i\omega_c^2}{N_p^2(\omega_c - \omega)^3 - \omega_c^2(\omega_c - \omega)} \left(e^{i(\omega_c - \omega)2\pi N_p/\omega_c} - 1 \right) \quad (C.3)$$

Thus, the amplitude spectrum is

$$|F(\omega)| = \frac{2\omega_c^2}{\left| N_p^2(\omega_c - \omega)^3 - \omega_c^2(\omega_c - \omega) \right|} \left| \sin \frac{(\omega_c - \omega)\pi N_p}{\omega_c} \right| \quad (C.4)$$

The mean-square angular frequency bandwidth of the five-peaked wave can be obtained by

$$(\Delta\omega)^2 = \frac{1}{2\pi} \int_0^\infty (\omega - \omega_c)^2 \frac{|F(\omega)|^2}{E} d\omega \quad (C.5)$$

where $\Delta\omega$ is the mean-square angular frequency bandwidth, E is the energy contained in the signal $f(t)$, which can be given as

$$E = \frac{1}{2\pi} \int_{-\infty}^\infty |f(t)|^2 dt = \frac{3\pi N_p}{\omega_c} \quad (C.6)$$

It must be noted that the integral limitation of Eq. (C.5) is set from zero to positive infinite since the practical frequency is positive real. Substituting Eq. (C.4) and Eq. (C.6) into Eq. (C.5), the mean-square bandwidth is finally obtained

$$\Delta\omega = \frac{1}{\sqrt{3}} \frac{\omega_c}{N_p} \quad (C.7)$$

From this result, it can be known that the frequency bandwidth of a five-peaked wave is proportional to its central frequency.